Fabrication and Characterization of GaInAs-InP Nanostructures

thesis by

Roderick William MacLeod

Submitted for the degree of Doctor of Philosophy to the Electrical and Electronics Engineering Department of Glasgow University

March 1994

© Roderick William MacLeod, 1994

ProQuest Number: 13818513

All rights reserved

INFORMATION TO ALL USERS
The quality of this reproduction is dependent upon the quality of the copy submitted.

In the unlikely event that the author did not send a complete manuscript
and there are missing pages, these will be noted. Also, if material had to be removed,
a note will indicate the deletion.

ProQuest 13818513

Published by ProQuest LLC (2018). Copyright of the Dissertation is held by the Author.

All rights reserved.
This work is protected against unauthorized copying under Title 17, United States Code
Microform Edition © ProQuest LLC.

ProQuest LLC.
789 East Eisenhower Parkway
P.O. Box 1346
Ann Arbor, MI 48106 – 1346

Thesis
9789
Copy 1

GLASGOW
UNIVERSITY
LIBRARY

Abstract

This thesis is concerned with the fabrication and characterization of semiconductor nanostructures. In particular, the semiconductor material used in this research consisted of InGaAs, as a quantum well layer, sandwiched between layers of InP, which acts as a barrier layer.

The driving force behind this research was twofold. Firstly, it included a desire to understand the physics governing the behaviour of these devices. As the lateral sizes of these devices decrease, theories predict that the structures will give strong atom-like resonances, so a study of these structures is similar to studying large quasi-atoms. Secondly, besides the fundamental physics involved, there was also a practical application stimulating this research. Already, quantum well lasers are used in the consumer electronics market, and it was speculated that by using quantum wire or dot systems the laser threshold currents would be reduced still further, yielding improved laser efficiency.

The fabrication process involved electron beam lithography to pattern structures as small as 10nm in diameter, reactive ion etching (RIE) to transfer these patterns to the semiconductor, and various other post-RIE fabrication steps including wet chemical etching and annealing, as required. No evidence of an optically inactive "dead layer" was found because luminescence was observed from even the smallest structures. If an optically inactive region did exist its thickness could only be of the order of a few nanometres. The characterization of the nanostructures included techniques such as photoluminescence spectroscopy and absorption measurements.

The photoluminescence measurements revealed the participation of a number of different energy levels in the emission spectra when the lateral dimensions of the nanostructures were reduced to 100nm or less. This high energy level participation became more pronounced when the lateral dimensions were reduced below 50nm.

Quantum confinement was clearly observed in the low temperature emission spectra of 10nm and 20nm diameter dots. This quantum confinement was manifested by an energy upshift of the PL peak energy.

It was found that exciton transport plays a crucial role in the emission strength of wires. This was attributed to localization effects resulting from variations in the layer thickness at the InGaAs/InP interface, as well as alloy potential fluctuations.

Annealing of a sample after RIE and wet chemical etching reduced the absolute PL intensity of the quantum structures and also caused narrowing of the PL emission.

Wet chemical etching of a sample after RIE narrowed the PL spectrum of quantum structures compared with structures of similar lateral dimensions which were only subjected to RIE. In particular, the samples which were wet etched did not exhibit the broadening to high energies characteristic of the RIE only samples.

to my Mother and Father

The storm is chang'd into a calm
at his command and will;
So that the waves, which rag'd before,
now quiet are and still.

Then are they glad, because at rest
and quiet now they be:
So to the haven he them brings,
which they desired to see.

(Scottish Metrical Psalms, Psalm number 107 verses 29 & 30)

Acknowledgements

I would like to take this opportunity to thank the many people who helped me during the course of this work.

I am grateful to Clivia Sotomayor Torres, my academic supervisor, for her guidance, enthusiasm and help throughout this work. I would also like to thank Malcolm Saker, my industrial supervisor, for his help and advice; and the DRA for the additional funding.

The technical assistance in the department is excellent. Douglas Irons, initially, and Alex Ross, latterly, were responsible for the care of the nanostructure lab. in which I worked. Their ability and readiness to assist was of great help. I would also like to thank Joe Smith and Robert Kirk for their help. Douglas MacIntyre, Dave Gourley, Helen McLelland and Susan Ferguson were very helpful in teaching me how to use all manner of microscopes and evaporators with numerous bells and whistles. Ray Darkin, Dave Clifton, Dave Lawson and Gillian Hopkins helped me with any RIE problems I encountered and made Friday afternoons, when I did most of my etching, pass quicker.

There were other technicians who helped me during my research but to list their names would take to long. To ensure that I don't omit anyone I will use this opportunity to thank them en masse.

I would like to thank Stephen Thoms (who knows more about electron beam lithography than anyone has a right to know) for helping me with the Jeol - that most esoteric of machines - and the other electron beam machines in the department. John Weaver and I shared many a failed "lift-off" fabrication step and I would like to thank him for his "Jeol and general fabrication" hints and for starting the Jeol self-help group.

Hazel Arnot, Morag Watt, Yinsheng Tang and Peidong Wang taught me some of the secrets of optical spectroscopy and helped with some of the experiments I did. I would like to thank Andy Smart and William Rodden for all of the interesting discussions we had, few of which had anything to do with work.

There is a host of postgraduate students and research assistants I should thank but time and space do not permit. I would, however, like to thank those I shared an office with, particularly Andy Jennings and Ken Thomas, and those I played five-a-side football with (John Bebbington, Jim Bonar, Calum Cossar etc.).

I owe a great debt to the minister and congregation of Partick Highland Free Church, who did so much to welcome me and encourage me during my years in Glasgow. More than anything or anyone else they made my time in Glasgow bearable when times were bad and enjoyable when times were good.

Last of all I would like to thank my parents and brothers, who helped me to keep this work in perspective and to distinguish between the important things and those things which were just academic.

Table of Contents

Chapter 1	Introduction and basic theory	1
1.1	Progress in microelectronics	1
1.2	Excitons	2
1.3	Low dimensional effects	3
1.4	Heterojunctions	4
1.4.1	The quantum well	6
1.5	Exciton confinement effects in quantum structures	6
1.5.1	Exciton confinement effects in quantum wells	6
1.5.2	Exciton confinement in quantum wires and dots	7
1.6	The InGaAs/InP quantum well system	8
1.6.1	Advantages of the InGaAs/InP quantum well system	9
1.7	Growth of InGaAs/InP	9
1.7.1	Elemental source MBE	10
1.7.2	MOVPE	10
1.7.3	Gas-Source, metal-organic and chemical beam epitaxy	10
1.7.4	Heterojunction interface quality	12
1.8	Surface recombination	13
Chapter 2	Literature study and review	17
2.1	Fabrication of quantum structures - background information	17
2.2	Fabrication of quantum wires	18
2.2.1	Direct growth of wires	18
2.2.2	Ion implantation to obtain quantum wires	19
2.2.3	Strain confinement of carriers to quantum wires	19
2.2.4	Selective barrier removal to obtain quantum wires	20
2.2.5	Holographic photolithography	21
2.2.6	Lithography and wet etching to produce quantum wires	22
2.2.7	Lithography and ion beam milling to fabricate wires	23
2.2.8	Lithography and reactive etching to fabricate wires	25
2.3	Fabrication of dots	26
2.3.1	Direct growth of quantum dots	27
2.3.2	Strain confinement of carriers to quantum dots	27
2.3.3	Lithography and ion beam milling to produce dots	27
2.3.4	Lithography and reactive ion etching	28
2.4	Summary of literature published on quantum wires and dots	28
Chapter 3	Pattern delineation and lithography	32
3.1	Lithography - General principles	32
3.2	Resist	33
3.2.1	Negative resist	34
3.2.2	Positive resist	34
3.2.3	Resist exposure	35
3.2.4	Electron scattering - the proximity effect	35
3.3	PSEM500 electron beam machine	36
3.3.1	Fabrication process for PSEM500	37
3.3.2	Sample layout and design	41
3.3.3	Disadvantages of the PSEM500	41
3.4	JEOL 100CXII electron beam machine	43
3.4.1	Fabrication process for JEOL 100CXII	45
3.4.2	Sample layout and design	46
3.4.3	High resolution lithography using the JEOL	48
3.5	The Electron Beam Pattern Generator	50
3.5.1	Fabrication process for the Beamwriter	52
3.5.2	Sample layout and design	52
3.5.3	High resolution lithography using the Jeol	53

Chapter 4	Pattern transfer and reactive ion etching	56
4.1	The need for dry etching	56
4.2	Reactive ion etching - general introduction	56
4.3	Basic theory of rf discharges	57
4.3.1	Generation of active species	57
4.3.2	Anisotropic etching	58
4.4	Etching with a methane/hydrogen gas mixture	59
4.5	Surface damage due to RIE	61
4.6	The ET340 reactive ion etch machine	61
4.6.1	Optimising the ET340 CH_4/H_2 process	62
4.6.2	Damage inflicted by ET340 during CH_4/H_2 etching	69
4.7	The µP80 reactive ion etch machine	70
4.7.1	Advantages of the µP80 RIE machine	70
4.7.2	Optimising the µP80 CH_4/H_2 process	71
4.7.3	The multi-step etch process	74
4.7.4	Damage inflicted by µP80 during CH_4/H_2 etching	76
4.8	Comparisons between CH_4/H_2 etching in ET340 and µP80	76
Chapter 5	Experimental techniques and apparatus	88
5.1	Introduction to luminescence spectroscopy	88
5.1.1	Photoluminescence spectroscopy (PL)	88
5.1.2	Photoluminescence Excitation (PLE)	89
5.2	Absorption experiments	91
5.3	Photoluminescence apparatus	92
5.3.1	PL apparatus - experimental method	98
5.4	The Fast Fourier Transform (FFT) spectrometer	99
5.5	Summary of nanostructure characterization techniques	105
Chapter 6	Luminesence spectroscopy of wires and dots	108
6.1	Sample fabrication considerations	108
6.1.1	Samples referenced in this thesis	109
6.1.2	Guide to nomenclature of wires and dots	111
6.2	Dots from 600 to 60nm fabricated using the PSEM500 AND ET340	111
6.2.1	PL spectra from 600 to 60nm sized dots	112
6.2.2	Integrated PL intensities of 600 to 60nm sized dots	118
6.2.3	discussion of data from 600 to 60nm dots	119
6.3	Wires down to 30nm fabricated using the JEOL and µP80 system	120
6.3.1	170 and 100nm wires - sample nos.2 & 3	120
6.3.1.1	Determination of PL intensity variation with wire length	120
6.3.1.2	Discussion of PL intensity variation with wire length	122
6.3.2	50 to 30nm wires - sample no.4	123
6.3.3	Discussion of PL data obtained from sample no.4	129
6.3.4	Very small wires - sample no.5	133
6.3.5	Discussion of PL data obtained from sample no.5	137
6.4	Wire and dot samples fabricated down to 20nm using the Beamwriter and µP80 system - sample nos.6 to 10	139
6.4.1	Wires and dots down to 20nm - sample no.6	142
6.4.2	Discussion of PL data obtained from sample no.6	144
6.4.3	Annealing of wires and dots - sample no.7	146
6.4.3.1	PL spectra obtained from sample no.7	147
6.4.3.2	Effects of annealing on quantum dots	148
6.4.4	Wet etching of dry etched structures	149
6.4.4.1	PL of annealed and wet etched structures - sample no.8	150
6.4.4.2	Wires and dots - sample no.9	151
6.4.4.3	The effect of wet etching on quantum structures	155
6.4.5	Summary of PL experiments on samples fabricated with the Beamwriter	156

6.5	Experiments performed with an FFT spectrometer	157
6.5.1	FFT PL and absorption measurements on sample no.4	158
6.5.2	Spatially resolved PL experiments	159
Chapter 7	Conclusions and further work	163
7.1	Conclusions	163

Table of Figures

Figure 1.1	Variation of the density of states with increasing confinement	4
Figure 1.2	Band diagram of two different semiconductors when separated (a) and when forming a heterojunction (b)	5
Figure 1.3	Diagram of a quantum well system	6
Figure 1.4	Typical differences between wire and dot widths and lateral dimensions	7
Figure 1.5	Epitaxial layer growth technologies	11
Figure 1.6	Linewidths for various growth processes	13
Figure 2.1	Wire emission intensity as a function of geometrical wire width	24
Figure 2.2	Graph of PL peak energy shift versus wire width	29
Figure 3.1	Positive and negative resist operation	35
Figure 3.2	Diagram of forward scattering and backscattering of electrons	36
Figure 3.3	Modified PSEM500 lithography system	37
Figure 3.4	The "lift-off" process	38
Figure 3.5	Wet etched alignment marks	39
Figure 3.6	Wet etched rectangular alignment marks	39
Figure 3.7	Fabrication of dots using positive and negative resists	40
Figure 3.8	Sample layout for use with PSEM500	41
Figure 3.9	Micrograph of sample layout	42
Figure 3.10	Modified Jeol 100CXII	44
Figure 3.11	Lift-off with bi-layer resist	45
Figure 3.12	Sample layout for use with the Jeol	46
Figure 3.13	Micrograph of sample layout	47
Figure 3.14	20nm wide wire array	49
Figure 3.15	10nm wide wire array	49
Figure 3.16	30nm dot array	50
Figure 3.17	Diagram of Beamwriter (EBPG HR5) column	51
Figure 3.18	Sample layout for use with the Beamwriter	52
Figure 3.19	30nm wide wire array	53
Figure 3.20	Array of 25nm diameter dots	54
Figure 3.21	Array of 10nm diameter dots	54
Figure 4.1	Sputtering of substrate with ions, and chemical etching with gas molecules	57
Figure 4.2	Effect of rf signal on substrate	59
Figure 4.3	Diagram of the ET340 etch chamber	61
Figure 4.4	Changes in etch profile with time, showing origin of overcut profile	64
Figure 4.5	Etch depth versus time for optimum CH_4/H_2 conditions	64
Figure 4.6	Two micrographs showing 100nm (upper micrograph) and 60nm (lower micrograph) wide pillars of InP, etched under optimum conditions	66
Figure 4.7	Micrographs of dots etched in various etch conditions, as shown in table 4.1	67
Figure 4.8	Micrographs of dots etched in various etch conditions, as shown in table 4.1	68
Figure 4.9	Diagram of the μP80 etch chamber	70
Figure 4.10	Micrographs of dots etched in various CH_4/H_2 ratios	72
Figure 4.11	Etch rate versus pressure for etching InP in the μP80	73
Figure 4.12	A 50nm wide wire after a multi-step etch consisting of three 5 minute etches	75
Figure 4.13	50nm wide wire after a multi-step etch consisting of five 3 minute etches	75

Figure 4.14 Structure of the samples which were used for etch tests, and some examples of the different depths to which these samples were etched 78
Figure 4.15 PL spectrum of an unetched sample (B308) excited with 100μW of laser power 79
Figure 4.16 PL spectrum of sample B308 after having 95nm removed from its surface by etching in the ET340 79
Figure 4.17 PL spectrum of an unetched sample (B308) excited with 100μW of laser power 80
Figure 4.18 PL spectrum of sample B308 after having 100nm removed from its surface by etching in the μP80 80
Figure 4.19 PL spectrum of an unetched sample (B308) excited with 100μW of laser power 83
Figure 4.20 PL spectrum of sample B308 after having 180nm removed from its surface by etching in the ET340 83
Figure 4.21 PL spectrum of an unetched sample (B308) excited with 100μW of laser power 84
Figure 4.22 PL spectrum of sample B308 after having 185nm removed from its surface by etching in the μP80 84

Figure 5.1 Excitation processes in quantum wells 89
Figure 5.2 Schematic diagram of observable PLE transitions 90
Figure 5.3 Typical apparatus for absorption experiments 92
Figure 5.4 Plan diagram of the PL experimental apparatus 93
Figure 5.5 Diagram of helium cooling system 94
Figure 5.6 CF1024 cryostat and insert rod 95
Figure 5.7 Grating efficiency curves for 600 grooves per mm gratings 97
Figure 5.8 Experimental (lower) and theoretical (upper) spectra of a blackbody source 98
Figure 5.9 Diagram of BIO-RAD FT60A FFT spectrometer 100
Figure 5.10 Diagram of the Michelson interferometer used in the BIO-RAD FT60A FFT spectrometer 101
Figure 5.11 FFT spectrometer configuration for absorption experiments 102
Figure 5.12 PL configuration of FFT spectrometer 103
Figure 5.13 Plan view of sample holder for PLE experiments 103
Figure 5.14 Spatially resolved PL experimental apparatus 105

Figure 6.1 B556 sample structure 111
Figure 6.2 PL spectrum obtained from the mesa on sample no.1 112
Figure 6.3 PL spectrum obtained from a 300nm wide dot array on sample no.1 113
Figure 6.4 PL spectrum obtained from both the mesa and 100nm wide dot array on sample no.1 113
Figure 6.5 Laser power versus integrated emission intensity for sample no.1 115
Figure 6.6 PL spectra of B556 material recorded at three different sample temperatures 116
Figure 6.7 Structure of sample no.3 120
Figure 6.8 PL integrated intensity versus wire length for the 100nm wide wire arrays on sample no.3 121
Figure 6.9 PL integrated intensity versus wire length for the 170nmm wide wire arrays on sample no.2 122
Figure 6.10 Micrograph of 30nm (possibly 15nm) wires 124
Figure 6.11 PL spectra of a 50nm wide wire array and a mesa array on sample no.4 125
Figure 6.12 PL spectra of the same 50nm wide wire array on sample no.4 126
Figure 6.13 PL spectra of a 30nm wide wire array on sample no.4 127
Figure 6.14 PL spectra from the second 50nm wide wire array and a mesa array on sample no.4 128

Figure 6.15	PL spectra of the second 50nm wide wire array and a mesa array on sample no.4	129
Figure 6.16	Structure of sample no.5, PMB297	133
Figure 6.17	Micrograph of the 20nm wide wire array on sample no.5	134
Figure 6.18	PL spectra of a 20nm wide wire array and a mesa array on sample no.5	135
Figure 6.19	PL spectra of an array of 20nm wide wires on sample no.5	136
Figure 6.20	PL spectra obtained from the 20nm wide wires on sample no.5	137
Figure 6.21	Structure of sample 2311, sample no.6	140
Figure 6.22	Laser power versus integrated emission intensity for material type 2311	140
Figure 6.23	Temperature dependence of the PL peak position of material type 2311	141
Figure 6.24	Relationship between measured PL peak width and temperature for material type 2311	142
Figure 6.25	PL spectra of a 20nm wide dot array under two different excitation intensities	143
Figure 6.26	PL spectra of a 30nm wide wire array under two different excitation intensities	144
Figure 6.27	PL spectra of a 20nm wide dot array on sample no.7 before and after annealing	147
Figure 6.28	PL spectra of a 50nm wide dot array on sample no.7 before and after annealing	148
Figure 6.29	PL spectra of an annealed and wet etched 30nm wide dot array and a mesa array	151
Figure 6.30	PL spectra of a 330nm wide dot array and a mesa area on sample no.9	152
Figure 6.31	PL spectra of a 20nm wide dot array and a mesa area on sample no.9	153
Figure 6.32	PL spectra of a 10nm dot array and a mesa array on sample no.9	154
Figure 6.33	PL spectra of a 25nm wide array and a mesa area on sample no.9	154
Figure 6.34	Graph of energy up-shift versus diameter for reactive ion then wet etched quantum dots fabricated on material type 2311	157
Figure 6.35	FFT absorption and PL spectrum obtained from a 30nm wide wire array and mesa area on sample no.4	159
Figure 6.36	SRPL spectra of different sites of a mesa area on sample no.4	160
Figure 6.37	SRPL spectra of three different sites on a mesa area on sample no.10	160

Table of Tables

Table 2.1	Summary of published wire widths and corresponding energy shifts	28
Table 3.1	Wavelengths and masses of moving electrons	33
Table 3.2	Frame and pixel sizes and corresponding magnifications for PSEM500	37
Table 3.3	Details of exposure values for dot files using PSEM500	40
Table 3.4	Frame and pixel sizes and corresponding magnifications for the Jeol 100CXII	44
Table 3.5	Details of Jeol parameters for fine line lithography	48
Table 3.6	details of the parameters used for Beamwriter lithography	53
Table 4.1	Summary of important etch results	63
Table 4.2	µP80 etch results for constant rate of CH_4 flow	72
Table 4.3	Etch results for µP80 with constant CH_4 to H_2 ratio	73
Table 4.4	Positions, FWHM, and integrated intensities of PL peaks on figures 4.15 to 4.18	81
Table 6.1	Samples used in this research work	110
Table 6.2	Two-Gaussian approximation parameters for figures 6.2 to 6.4 with possible interpretation of emission origin	114
Table 6.3	Integrated PL intensity for sample no.1	119
Table 6.4	Theoretical energy level emission for a 10nm thick well	130
Table 6.5	PL peak intensities of spectra from figures 6.11 and 6.12 and tentative assignments of emission origin	131
Table 6.6	PL peak intensities of spectra from figure 6.13	131
Table 6.7	Deconvolution of spectrum (a) on figure 6.13 using a 3 gaussian approximation	132
Table 6.8	Theoretical energy levels for a 9nm thick quantum well	138
Table 6.9	Deconvolution of spectrum (d) on figure 6.20 using a 3-Gaussian approximation	138
Table 6.10	Deconvolution of mesa spectrum of figure 6.25 using 2-Gaussian approximation	144
Table 6.11	Deconvolution of spectrum (c) on figure 6.25 using a 3-Gaussian approximation	145
Table 6.12	Results of 3-Gaussian deconvolution of spectrum (c) on figure 6.26	146
Table 6.13	Deconvolution of figures 6.27 and 6.28	149
Table 6.14	PL peak positions for different structure types after various fabrication processes	156
Table 6.15	PL peak positions for different arrays after wet and dry etching	156

Chapter 1
Introduction and basic theory

1.1 Progress in microelectronics

Since the beginning of the microelectronics era, which was ushered in with the discovery of the transistor in the late 1940's, there has been a continuous trend towards smaller device dimensions to provide, amongst other things, faster devices and greater device density on integrated circuits.

This philosophy that smaller devices are inherently better than larger ones led to the harnessing of optical lithography to reduce integrated circuit linewidths to approximately 0.3μm, and now utilises electron beam lithography to enable linewidths of the order of tens of nanometres to be produced.

However, in pursuit of miniaturisation the linewidths have become so small that they are comparable with the de Broglie wavelength of the carriers in the substrate material. The de Broglie wavelength, λ_B, is given by equation 1.1:

$$\lambda_B = h / p \qquad 1.1$$

where p is the carrier momentum, which is related to the effective mass of the carriers (m^*) by equation 1.2:

$$p^2 = 2m^* k T \qquad 1.2$$

The laws of 'classical mechanics' no longer account for the behaviour of these small structures because they are in the regime where quantum size effects become increasingly important and can even dominate the behaviour of the devices.

Quantum size effects are manifested by the occurrence of new physical phenomena which accompany the reduction of device dimensions. This research work is concerned with the study of these new phenomena in structures fabricated to sizes within the quantum size regime. Examples of these phenomena will be introduced and considered throughout this chapter.

1.2 Excitons

Perhaps the single most important concept which must be grasped in order to understand this area of research is that of the exciton. An exciton, in general, is the name given to an excited electronic energy state of a semiconducting or insulating crystal (Elliot, 1957).

When a semiconductor is irradiated with light of energy approximately equal to or greater than its energy band gap then it begins to absorb the incident energy. In this absorption process an electron from the valence band is excited into the conduction band leaving behind a positively charged hole in the valence band. This electron-hole pair can, under certain circumstances, form an exciton. An exciton is an electron-hole pair which is bound together by the mutual interaction arising from the coulombic attraction between the negatively charged electron and the positively charged hole (Dexter and Knox, 1965).

The energy required to form an exciton is less than the energy of the band gap. This energy difference corresponds to the binding energy of the exciton. Since excitons in GaAs and InGaAs are only weakly bound they are analogous to the hydrogen atom, and the allowed energy states of the exciton can be approximated by a hydrogenic model (i.e. the effective mass approximation) such as equation 1.3. (Bube, 1981):

$$E_{ex,n} = \frac{\mu_r}{m_o} \cdot \frac{1}{\varepsilon_r^2} \cdot \frac{1}{n^2} \cdot E_H \qquad 1.3$$

where E_H is the ground state energy of an isolated hydrogen atom, m_o is rest mass of an electron, ε_r is the dielectric constant of the material, n is the principal quantum number, and μ_r is the reduced mass of the exciton, which is given by equation 1.4:

$$\frac{1}{\mu_r} = \frac{1}{m_e^*} + \frac{1}{m_h^*} \qquad 1.4$$

For InGaAs, using the values given in Appendix A, the light-hole exciton ground state binding energy is 1.6meV, and the heavy-hole exciton ground state binding energy is 2.7meV.

An exciton can diffuse through the semiconductor and transport energy (represented by the binding energy of the electron and hole), however, because the exciton is electrically

neutral no net charge is transported (Kittel, 1986). The approximate total energy of an exciton is given by equation 1.5:

$$E_{ex} = \frac{\hbar^2 K_{ex}^2}{2(m_e^* + m_h^*)} + E_{ex,n} \qquad 1.5$$

where the first term on the right hand side of the equation represents the kinetic energy of the exciton, K_{ex} is a wave-vector which represents the motion of an exciton's centre of mass, and $E_{ex,n}$ is the binding energy of the exciton in its nth state (N.B. the binding energy is negative).

The effective "size" of an exciton is given by the Bohr radius (a_B) which, in 3 dimensions, is given by equation 1.6.

$$a_B = \frac{\varepsilon_r a_o m_o}{\mu_r} \qquad 1.6$$

where a_o is the Bohr radius for a hydrogen atom.

For InGaAs, this equation yields a light-hole exciton Bohr radius of 32nm and a heavy-hole exciton radius of 19nm. These values of Bohr radius for InGaAs are approximately double those of GaAs, the implications of which will become clear when quantum wire and dot fabrication problems are considered in the fabrication chapter of this thesis (chapter 3).

1.3 Low dimensional effects

Foremost amongst the new phenomena which occur with a diminishing of the structure size is the radically altered density of allowed energy states.

In a bulk semiconductor - i.e. a semiconductor whose lateral dimensions are very much greater than the de Broglie wavelength of the carriers - the density of allowed energy states takes the form of a continuum beginning at the band gap energy and with an $E^{1/2}$ shape. If one of these lateral dimensions is reduced sufficiently (the so-called quantum slab) then the DOS (density of states) becomes step-like. When two dimensions are reduced (the so-called quantum wire) the DOS assumes the form of a single step followed by a tail with an approximately $E^{-1/2}$ dependence; and finally, when all these dimensions are small (the so-called quantum box or dot) then the DOS becomes a series of delta functions which resemble the energy level scheme of atoms.

These conditions are termed 3D, 2D, 1D and 0D quantum confinement respectively, and are illustrated schematically in figure 1.1.

Thus, it is clear that the term 'low dimensional' has a twofold meaning: used in one sense it can refer to reduced dimensionality, i.e. a regime where carriers are confined in one or more direction - as shown in figure 1.1; but in another sense the term can be applied where low is used to mean small, i.e. where sizes are small compared with the de Broglie wavelength of the carriers (Razeghi, 1989).

The radical change in the DOS produces major changes in the optical properties of semiconductors of reduced dimensionality. As can be seen from figure 1.1 the band-broadened optical properties of bulk solids are transformed to sharp, atom-like resonances with the move to lower dimensional structures. With these sharp, atom-like resonances comes a concentrated oscillator strength. Confinement of the carriers does not actually change the oscillator strength per electron-hole pair, but the strict requirement of momentum conservation is relaxed with reduced dimensionality. This has the effect of concentrating the oscillator strength compared with the bulk system, the 3D case (Weisbuch, 1991).

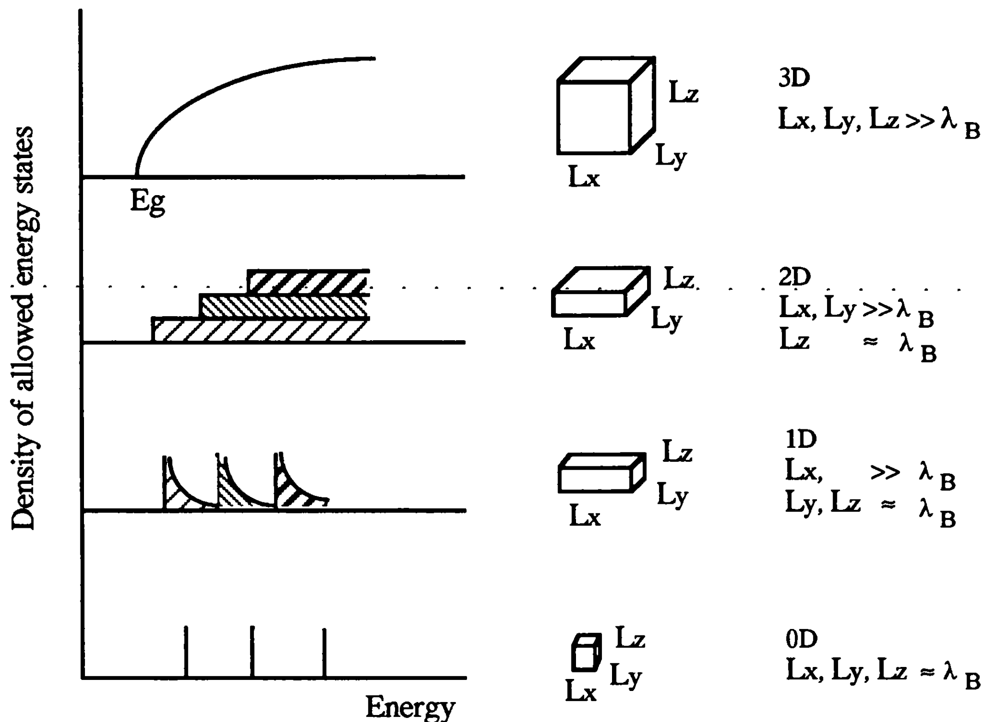

Figure 1.1 Variation of the density of states with increasing confinement

1.4 Heterojunctions

Figure 1.1 shows the effects of reduced dimensionality which arise as a result of the small lateral dimensions of a semiconductor. It is now necessary to consider how these small sizes are achieved in practice. This inevitably introduces the concept of the heterojunction.

A heterojunction results when two different semiconductors are brought together to form an abrupt junction. In a perfect heterojunction the bulk properties of each semiconductor remain unchanged right up to the interface, and then they abruptly change into the bulk properties of the other semiconductor. To satisfy these conditions the semiconductors which constitute the heterojunction must have similar lattice structure and lattice constants (Jaros, 1989).

The next problem concerns the electronic structure of the heterojunction system, and particularly the alignment of the band structures, i.e. the alignment of the two periodic potentials relative to each other. Since the band structures (the dispersion energy E_k versus wave vector k) are different for each semiconductor then there will be a discontinuity (a potential step) in both the conduction and valence bands at the semiconductor interface: these discontinuities are called the conduction band and valence band offsets, respectively.

The mean electron charge density must be the same on each side of the interface, and so the Fermi energies of the two semiconductors (which have similar lattice constants) must align. Figure 1.2 shows two semiconductors which are separated initially, and the bandstructure which results when the two are brought together to form a heterojunction .

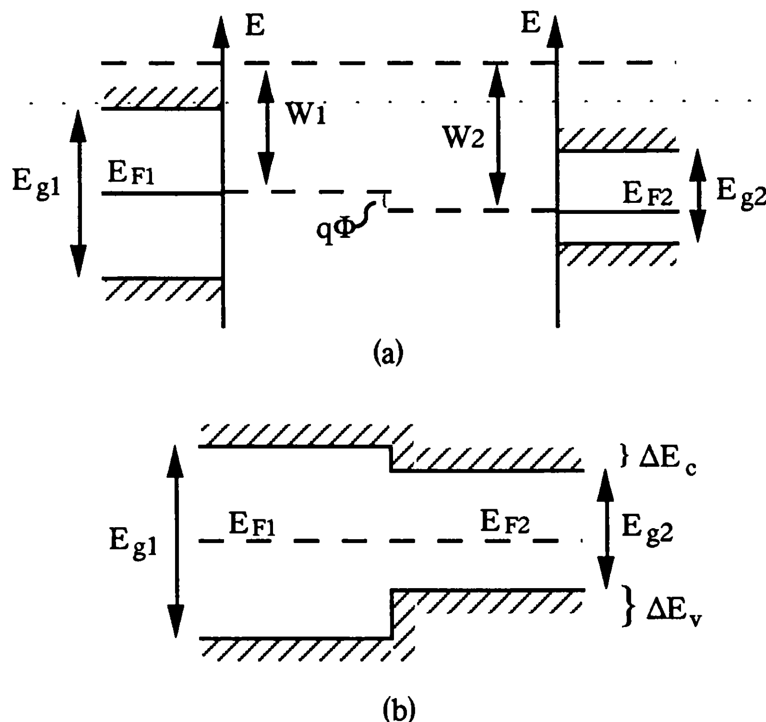

Figure 1.2 Band diagram of two different semiconductors when separated (a) and when forming a heterojunction (b). After Jaros, 1989

1.4.1 The quantum well

The logical extension of the concept of the heterojunction is the double heterojunction system, one example of which is the quantum well. A quantum well consists of a thin layer of material with energy gap E_{g2} (the quantum well layer) sandwiched between two layers of material with a larger energy gap E_{g1} (the barrier layers), as shown in figure 1.3. This figure shows the so-called type I quantum well, which means that the electrons and holes are both confined in the layer with energy gap E_{g2}.

The effect of this structure is to confine both of the carriers (electrons and holes) within the conduction and valence bands (respectively) of the lower band gap material. This is the method commonly used to obtain 2D confinement - the quantum well slab of figure 1.1.

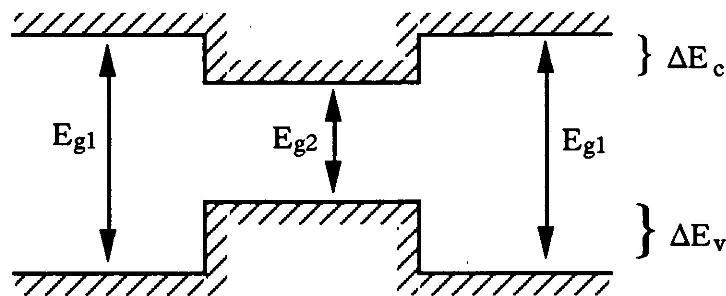

Figure 1.3. Diagram of a quantum well system.

1.5 Exciton confinement effects in quantum structures

1.5.1 Exciton confinement effects in quantum wells

Thus far, it has been assumed that confinement effects - such as those exhibited by the quantum wells - are complete, i.e. that the electron and hole wavefunctions are perfectly confined to the quantum well layer with no leakage of the wavefunction into the barrier.

However, this is not the case for real quantum wells because the confining potential in the well is finite. As the well width is reduced the confinement of the wavefunction becomes stronger until a certain critical size of well width is reached; below this critical size confinement effects weaken because the bound state is pushed up near to the top of the well, which lowers its binding energy and allows the wavefunction to leak into the barrier (Davies, 1992).

A simple approximation of the well width which yields maximum electron confinement is given by equation 1.7:

$$d = \sqrt{\frac{\hbar^2 \pi^2}{2m_e^* V_o}} \qquad 1.7$$

where d is the well width and V_o is the conduction band offset. For InGaAs this yields a value of 6nm for optimum confinement of the electron wavefunction.

To differentiate between perfect 2 dimensional confinement and confinement where the wavefunction leaks into the barrier the pre-fix "quasi" is usually added to the 2D in the latter case to signify that the system is not perfectly 2 dimensional.

The Bohr radius and binding energy calculations in section 1.2 referred to an exciton in a 3 dimensional system. In a 2 dimensional system these values require modification because confinement enhances the exciton kinetic energy and reduces the electron-hole separation, thus increasing the confined-exciton binding energy. In a perfectly 2D system the exciton binding energy increases four-fold and the Bohr radius is halved. An estimation of the 2D Bohr radius is given by equation 1.8 (Bryant, 1988).

$$a^{2D} = \sqrt{\frac{3}{8}}\,\frac{\varepsilon_r a_o}{\mu} \qquad 1.8$$

For InGaAs equation 1.8 yields a light-hole value, a_{lh}^{2D}, of 20nm; and a heavy-hole value, a_{hh}^{2D}, of 12nm.

1.5.2 Exciton confinement in quantum wires and dots

A common method of preparing wire and dot samples relies on patterning a quantum well sample in the plane of the quantum well. Most fabrication processes produce wire and dot structures with lateral dimensions (L) considerably larger than the well width, as shown in figure 1.4. This raises the question of how small L has to be for confinement effects to become important. The answer to this question is of great importance as it is fundamental in interpreting the photoluminescence spectra recorded in chapter 6.

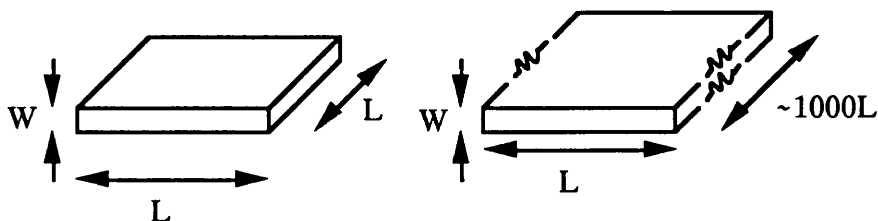

Figure 1.4 Typical differences between wire and dot widths and lateral dimensions

It is thought that there are three distinct regimes of confinement (D'Andrea et al, 1990). The first of these is where the lateral dimensions (L) are very small (comparable with the 2D Bohr radius) and the electron and hole wavefunctions are quantised independently, this is the regime of strong confinement, or separate electron and hole confinement.

The second regime is for samples with L » a_B but still less than some critical value (approximately 200nm for InGaAs), in this regime there are electron-hole pairs rather than excitons. Although in this regime the electronic wavefunctions are not quantised independently the exciton is still not completely free to move in the plane of the well because of "reflections" from the wire or dot boundaries. This gives rise to a standing wave pattern with quantised energy levels (Heitmann et al, 1991). The kinetic energy for centre of mass motion is given by equation 1.9.

$$E_{CM}^{kin} = \frac{\hbar^2 K_{ex}^2}{2(m_e^* + m_h^*)} \qquad 1.9$$

In the direction perpendicular to the wires, K_{ex}^n can only have quantised values

$$K_{ex}^n = \frac{\pi}{L_x} n \qquad n = 1,2,3,... \qquad 1.10$$

The third regime includes the size range between strong confinement (20nm) and centre of mass confinement (200nm). In this regime there is a gradual increase in the exciton ground state energy with decreasing lateral dimensions (L). It is expected that in this regime there is a transition from centre of mass confinement to strong confinement. As the lateral dimensions decrease the confinement energy increases but so does the binding energy (it becomes more negative) which tends to mask the increase in confinement energy and offset any small blue-shift in, for example, the photoluminescence (PL) spectra.

As a result of these competing processes and the different regimes of confinement, careful interpretation of the PL spectra of quantum wires and quantum dots is required.

1.6 The $In_{0.53}Ga_{0.47}As$/InP quantum well system

A number of possible material systems can be used to produce quantum well structures, the most common being the GaAs/AlGaAs system. In this system the GaAs acts as the confined layer and the AlGaAs as the barrier layer; these layers are grown successively onto a GaAs substrate. The InGaAs system is different because the ternary (InGaAs) acts as the confined layer and the binary (InP) as the barrier layer.

1.6.1 Advantages of the $In_{0.53}Ga_{0.47}As/InP$ system

There are several reasons why the InGaAs/InP material system was used and studied in preference to the GaAs/AlGaAs system.

A major advantage of this system is that the electron and light hole effective masses in InGaAs are lower than in GaAs. One of the fundamental length scales which affects carrier behaviour in quantum wells is the Bohr radius - the distance between the electron and hole in an exciton. The low electron effective mass in InGaAs ensures that the exciton Bohr radius is much larger in InGaAs (~20nm) than in GaAs (10nm), and so confinement effects should become apparent for larger wire and dot dimensions in this sytem. This eases the fabrication problems slightly because it is possible to fabricate structures with lateral dimensions as small as 20nm, which is the regime for strong confinement for this system.

Another advantage of this system is the lower surface recombination velocity in InP than in GaAs - up to 100 times lower according to some sources (Casey et al, 1977) - which implies that there will be greater luminescence efficiency for the InGaAs system than for the GaAs system. Patterning dots and wires greatly enhances the surface to volume ratio of the active material and so any surface defects become very important, and could even dominate the device behaviour by quenching the luminescence via non-radiative recombination centres. In light of this the prospect of a material system with a low surface recombination velocity is very appealing.

Finally, the InGaAs/InP system is very attractive for optoelectronics device applications, particularly for optical communication systems, because the system covers the region from 1.3 to 1.6μm. It is in precisely this region that the spectral range of low dispersion and minimum attenuation for silica fibres occurs. No elemental or binary semiconductor has an energy band gap within this range, so a ternary or quaternary material (such as InGaAsP) is needed.

1.7 Growth of InGaAs/InP

Producing heterostructures which are abrupt on an atomic scale requires the use of advanced epitaxial growth techniques. Numerous methods have been used to grow InGaAs epitaxial layers onto an InP substrate, examples include: low-pressure metal-organic vapour phase epitaxy (LP-MOVPE) (Razeghi et al, 1983), atmospheric pressure MOVPE (Skolnick et al, 1986 and Seifert et al, 1990), chloride VPE (Kodama et al, 1983), hydride VPE (DiGiusseppe et al, 1983), solid source molecular beam epitaxy (MBE) (Marsh et al, 1985), gas source MBE (Temkin et al, 1985) and chemical beam epitaxy (CBE) (Tsang and Schubert, 1986). Figure 1.5 shows some of the most common epitaxial growth technologies, with typical values of operating pressures.

1.7.1 Elemental source MBE

MBE employs atomic beams obtained from elemental sources which are evaporated at high temperatures onto a heated crystalline substrate where they react chemically under ultra high vacuum conditions . Although MBE is a very popular and good (in terms of interface and well quality) technique for growing GaAs/AlGaAs quantum wells, it is not so well suited to growing InGaAs/InP quantum wells due to the difficulty in handling phosphorous in a MBE system.

1.7.2 MOVPE

MOVPE growth proceeds with the introduction of metered amounts of group III alkyls and group V hydrides into a quartz tube containing a substrate on a heated carbon susceptor. This hot susceptor has a catalytic effect on the decomposition of the gaseous products and so the growth takes place primarily at this hot surface. The chemicals reach the substrate surface by diffusing through a stagnant gas boundary layer above the substrate.

There are three other growth techniques which bridge the gap between MBE and MOVPE, and offer some of the advantages which are associated with each process.

1.7.3 Gas source, metal-organic and chemical beam epitaxy

The term gas source MBE is used when elemental group III and vapour group V sources are used. The conventional group V elements are replaced by the gases AsH_3 and PH_3 which are decomposed to yield molecular beams containing As_2, P_2 and H_2.

In metal-organic MBE the group III metal evaporation sources are replaced by metal-organic compounds but the group V source is still elemental.

Chemical beam epitaxy is the name given to the process which uses both vapour group III and group V starting sources. The Ga and In are derived from the pyrolysis of triethylgallium and trimethylindium at the heated substrate surface, and the arsenic and phosphorous are obtained by thermal decomposition of their hydrides. These chemicals are then admitted into the high vacuum chamber in the form of a beam.

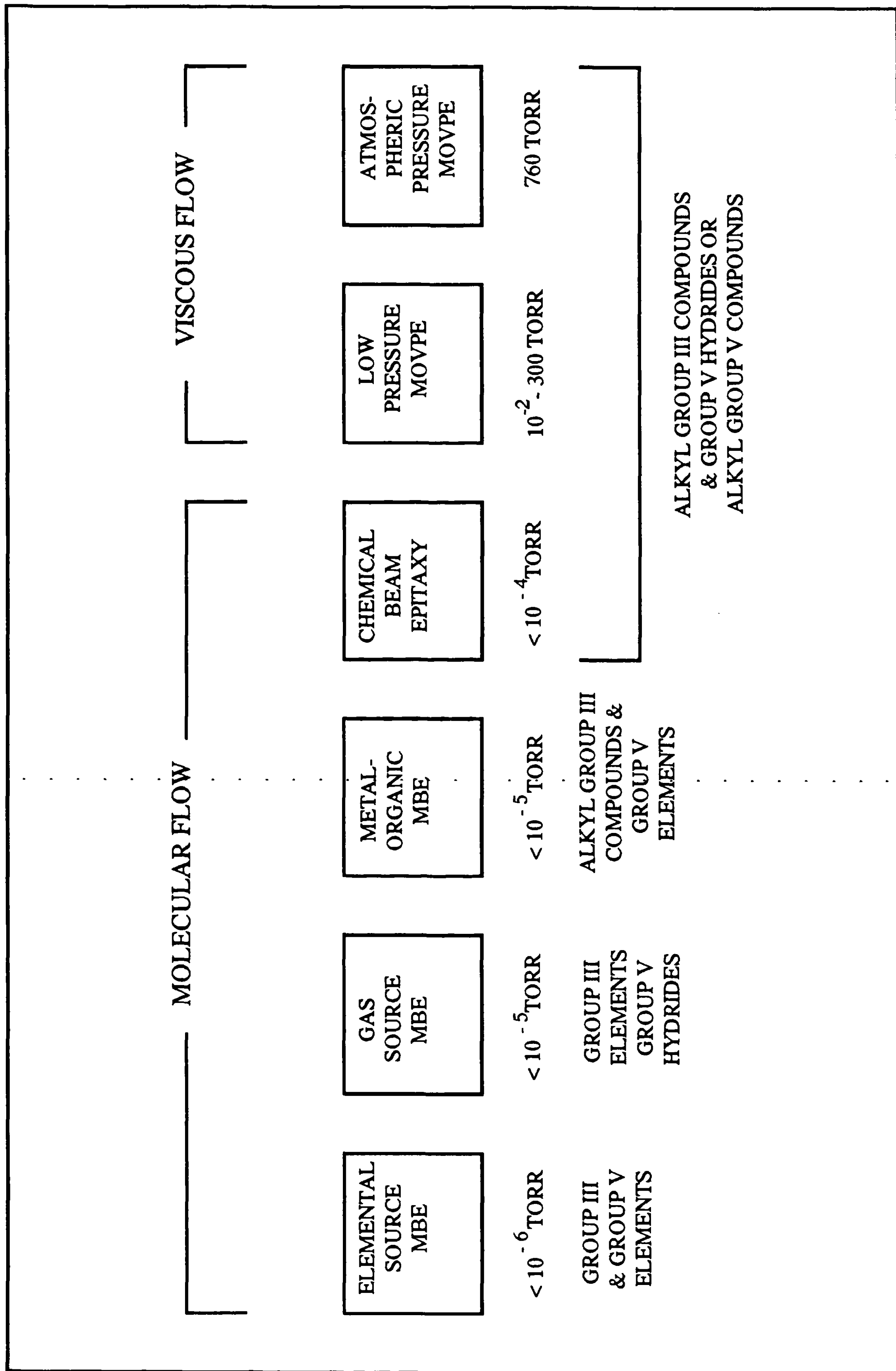

Figure 1.5 Epitaxial layer growth technologies (from Ploog, 1991)

1.7.4 Heterojunction interface quality

Regardless of which method is used to grow the quantum well the most important factor from a spectroscopist's point of view is the quality of the interfaces produced, with a high premium set on abrupt interfaces.

Assessing the quantum well interface quality is usually done by photoluminescence measurements. Although this technique may, on occasion, yield slightly misleading results, the advantages associated with it account for its widespread use. These advantages include the following: at low temperatures the principle linewidth broadening mechanism is the interface roughness (Singh et al, 1984); the technique is non-destructive; the experiment can be performed reasonably quickly; the quantum well signals are intense with strong resonances appearing which correspond to recombination in the well; impurities and native defects can be detected, even when they are in concentrations as low as 10^{15} cm^{-3} (Razeghi, 1989); and the type of emission - free exciton, bound exciton, donor-acceptor pairs, etc. can often be determined.

Figure 1.6 shows a graph of PL linewidth versus InGaAs quantum well width for various growth techniques. A striking feature of this graph is the dominance of the CBE technique: it produces InGaAs quantum wells with considerably lower values of full width at half maximum (FWHM) than any other technique. The material used throughout this research came from four different sources. AP-MOVPE grown quantum well material was supplied by RSRE, Sheffield University provided solid source MBE grown samples, RWTH in Aachen supplied MOVPE material which was specifically designed for this research work, and Thomson-CSF supplied some LP-MOVPE material. Comments on the quality of the material used will be given in chapter 6 of this thesis. In all cases, the FWHM values measured at 5K were larger than those obtained from samples grown by the CBE technique.

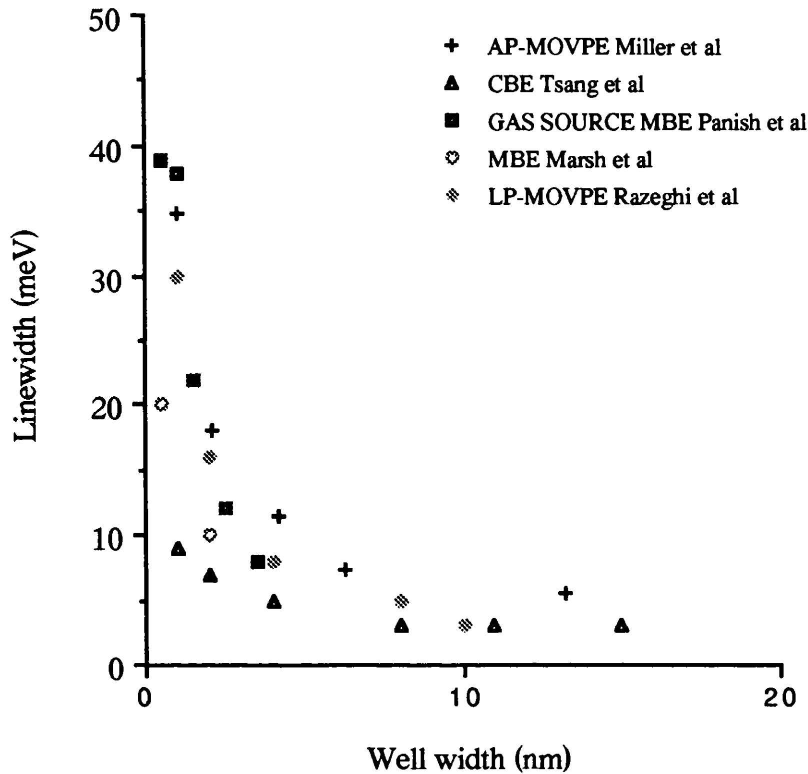

Figure 1.6 Linewidths for various growth processes

1.8 Surface recombination

Patterning wires or dots onto a sample surface inevitably increases the proportion of the quantum well material which is exposed to air. Any surface related effects will be exacerbated because of this increase in surface area which accompanies the patterning of wires and dots. For this reason it is necessary to study the role of surface effects.

The surface of any semiconductor represents the loss of periodicity of that semiconductor in one dimension, and hence there will be a change in the electronic states at that surface (Lassatère, 1987). The crystal surface gives rise to additional electron states whose wavefunctions extend over the entire crystal surface but which are sharply attenuated with distance into the sample (Christman, 1988). Surface states can be associated with dangling bonds, structural imperfections, modifications to the surface stoichiometry and adsorbed impurities. These electronic surface states (states with wavefunctions restricted to the surface) behave as trapping or non-radiative recombining centres and so introduce allowed energy levels into the band gap. There are also surface states which are introduced by defects and these states are localised at a certain point on the sample surface. These new energy levels increase the probability of non-radiative carrier recombination and hence reduce the luminescence signal.

This increase in non-radiative recombination suggests that there will be a lateral size for wires and dots below which radiative recombination will not be observable. If this lateral size is greater than the size where confinement effects become significant then the result is catastrophic because it will inhibit observation of quantisation effects. In the light of the above both the native surface properties and the effects of further processing on these properties become crucial.

Unlike GaAs, where the Fermi level is pinned approximately midway inside the bandgap, InP and both n- and p- type GaInAs have a Fermi level pinning position within 0.2eV of the conduction band minimum. The density of the surface states of InP is also more than an order of magnitude lower than that of GaAs (Wieder, 1985).

The position of the Fermi level pinning is an important parameter because it affects the size of the space-charge layer (also known as the "dead layer"). Pinning of the Fermi level (which can occur when there is a surface defect concentration as low as 0.1%) together with the presence of surface states gives large recombination velocities at the surfaces. The surface space-charge layer is related to the position of the Fermi level at the surface as measured from the conduction band and is called the barrier height: the smaller the barrier height the smaller the "dead layer" (Casey et al, 1977).

References

Blakemore J S, 1969 Solid State Physics (W B Saunders Company)

Bryant G W, 1988 Phys Rev B 37 (15) p8763-8772

Bube R H, 1981 "Electrons in Solids: An Introductory Survey" Academic Press, New York

Casey H C and Buehler E, 1977 Appl Phys Lett 30 (5) p247-249

Christman J R, 1988 "Fundamentals of Solid State Physics" (Wiley), New York

D'Andrea A and Del Sole R, 1990 Solid State Communications 74 (10) p1121-1124

Davies J H, 1992 Nanoelectronics Course, University of Glasgow, unpublished

Dexter D L and Knox R S, 1965 "Excitons" (Interscience Publishers), New York

DiGiuseppe M A, Temkin H, Peticolas L and Bonner W A, 1983 Appl Phys Lett 43 (10) p906-908

Elliot R J, 1957 Phys Rev 108 p1384-1389

Heitmann D, Lage H, Kohl M, Cingolani R, Grambow P and Ploog K, 1991 International meeting on Optics of Excitons in Confined Systems, Giardini Naxos, Italy, Inst Phys Conf Ser No 123, p109-117

Jaros M, 1989 Physics and Applications of Semiconductor Microstructures (Oxford University Press), Oxford

Kittel C, 1986 "Introduction to Solid State Physics" 6th Ed (Wiley), New York

Kodama K, Ozeki M and Komeno J, 1983 J Vac Sci Technol B1 (3) p696-699

Lassabatère L, 1987 in: Semiconductor Interfaces: formation and properties, Eds G Lelay, J Derrien and N Boccara, Springer proc in Physics Vol 22, Springer, Berlin, p239-272

Marsh J H, Roberts J S and Claxton P A, 1985 Appl Phys Lett 46 (12) p1161-1163

Ploog K, 1991 in "Low dimensional structures in semiconductors" Eds Peaker and Grimeiss. NATO ASI series B Physics Vol 281,Plenum press, New York, p47 - 67

Razeghi M, Hirtz J P, Ziemelis U O, Delalande C, Etienne B and Voos M, 1983 Appl Phys Lett 43 (6) p585-587

Razeghi M, 1989 The MOCVD Challenge (Adam Hilger)

Seifert W, Fornell J O, Ledebo L, Pistol M E and Samuelson L, 1990 Appl Phys Lett 56 (12) p1128-1130

Skolnick M S, Tapster P R, Bass S J, Apsley N, Pitt A D, Chew N G, Cullis A G, Aldred S P and Warwick C A, 1986 Appl Phys Lett 48 (21) p1455-1457

Singh J, Bajaj K K and Choudhuri S, 1984 Appl Phys Lett 44 (8) p805-807

Temkin H, Panish M B, Petroff P M, Hamm R A, Vandenberg J M and Sumski S, 1985 Appl Phys Lett 47 (4) p394-396

Tsang W T and Schubert E F, 1986 Appl Phys Lett 49 (4) p220-222

Wieder H H, 1985 VLSI Electronics: Microstructure Science Vol 10 p168-219 (Academic Press)

Weisbuch C, 1991 in: "Low dimensional structures in semiconductors" Eds Peaker and Grimeiss. NATO ASI series B Physics Vol 281, Plenum press, New York, p165 - 200

Chapter 2 Literature survey and review

2.1 Fabrication of quantum structures - background information

The general aim of this research is to produce samples which are patterned in such a way as to exhibit the effects of quantum confinement. More particularly, this research focuses on the use of the $In_{0.57}Ga_{0.47}As/InP$ material system.

The Nanoelectronics Research Centre at Glasgow University is not alone in pursuing the goal of achieving quantum confinement in heterostructures. Many other research establishments throughout the world have turned their attention to this problem. As a result, diverse methods to achieve this goal have come to light, each of these methods having its own peculiar advantages and disadvantages. This chapter deals with the work published by other groups in this burgeoning field, and seeks to elucidate some of the features of the more promising techniques for obtaining quantum confinement.

If quantum dot or wire technology is to be used for commercial applications, for example as the active layer in laser devices, then the technique used to create such structures needs to have certain features in order to lend itself to industrial applications. These features include the need for a reliable and reproducible fabrication process and preferably one that is amenable to high sample throughput. These industrial considerations have affected certain research groups who look towards industrial integration, as far as possible, for all their processes. However, since the subject is comparatively new and there remains much that is not fully understood, the suitability of the fabrication process to industrial use is not the primary concern of this work. The primary concern of this work is to fabricate these structures and understand the physics involved in their response to optical excitation.

The study of quantum confinement in heterostructures began in earnest when Dingle et al (1974) observed the quantisation of energy levels in quantum wells of GaAs surrounded by AlGaAs barriers. Since then, with the availability of highly controllable growth techniques, this field of study has received much attention world-wide, and work done on quantum well structures has proliferated.

2.2 Fabrication of quantum wires

In some ways the fabrication of wires is more appealing than the fabrication of dots. One of the main problems associated with quantum structures is the low signal strength of luminescence from these structures, making luminescence studies very difficult. In addition to other physical considerations, this problem arises from the low percentage of material left to luminesce after structures have been patterned to such small sizes (a few tens on nanometres). The percentage of quantum well material remaining after patterning tends to be greater in quantum wires (approximately 10 to 20%) than in quantum dots (approximately 4 to 10%), thus - in general - it is easier to obtain photoluminescence (PL) spectra from quantum wires than from quantum dots. The following sections deal with different methods used to pattern wires and so attain quasi-one dimensional confinement.

2.2.1 Direct growth of quantum wires

A method of growing quantum wires directly onto an epitaxial layer is a very attractive concept because it has the advantage of not introducing any damage to the wires, which inevitably occurs with processes which use dry etching or ion implantation to pattern wires. This method of direct growth also obviates the problems associated with nanometre scale lithography. A further advantage of a direct growth process is that buried wires can be fabricated in one process stage, and so the resulting wires are free from interface contamination or any other surface defects which are associated with etching (wet or dry), air exposure or subsequent regrowth steps.

Galeuchet et al (1990) fabricated wires using a *one-step MOVPE growth process*. This technique relies on differences in the growth behaviour of the ternary (GaInAs) for different crystal planes, and results in the reduction during growth of large dimensions on the substrate to the very much smaller dimensions of the wires grown.

They started with an InP substrate which was either patterned (for growth in a channel or on a mesa) or masked with silicon dioxide (for growth in a window in this mask). A plane selective growth technique was then used to obtain GaInAs layers which had both lateral and vertical dimensions in the quantum size regime. Cathodoluminescence (CL) experiments on these wires revealed a strong luminescence signal and a FWHM of 8meV indicating that the

wires were of high quality (see section 1.7.4 for typical values of FWHM for various growth techniques).

Cox et al (1989) proposed a direct growth technique which used a different method to that of Galeuchet et al (1989), their method utilised *vicinal substrates*. A vicinal substrate is a substrate which has a surface slightly misoriented from a low-index plane - for example, from the (001) direction. The process requires a grating of parallel grooves to be etched on the surface of a vicinal substrate, followed by an epitaxial growth stage which fills in the grooves. They demonstrated the principles of this process by fabricating very large GaInAs wires on an InP substrate, but no data is available for wires with dimensions in the quantum size regime.

2.2.2 Ion implantation to obtain quantum wires

Weiner et al (1990) employed an in situ *focused gallium ion beam* writing technique together with dry etching and gas source MBE to fabricate quantum wires. The process begins with the growth of a 3nm oxide layer on the top of an InP substrate. Squares are then patterned in the substrate using a gallium ion beam and the sample is etched by approximately 300nm using argon ion beam assisted chlorine etching. The last stage of the process is to regrow layers of InP and InGaAs within these etched squares using MBE.

The resolution limit of this process is determined by the spot size of the focused gallium ion beam, which for their particular experimental apparatus was approximately 200nm. The smallest wires they fabricated had a width of 200nm and a period of 2μm. These wires were assessed using CL. The lateral variation in CL intensity for these wires was small, which led them to conclude that recombination at the wire interfaces does not substantially degrade the quantum efficiency of the wires.

If the fabrication resolution of this technique could be lowered from the present value of 200nm then perhaps it would be a useful means of obtaining quantum confinement, however, the attainable size of 200nm is far too large to observe the quantum confinement effects associated with separate electron and hole confinement.

2.2.3 Strain confinement of carriers to quantum wires

Kash et al (1989) described a novel method of confining carriers by deliberately creating *strain patterns* in a quantum well. A uniform strained layer of GaInAsP was separated from the GaInAs quantum well by a thin barrier layer of InP. The strained overlayer was patterned with wires and etched away. The strained overlayer relaxes partially, producing an inhomogeneous strain pattern in the underlying material, creating a potential well for excitons under the strained layer by confining primarily the electrons.

They performed PL measurements on 400nm wide wires fabricated using this technique and found that the quantum well emission was red shifted. They cited the high luminescence efficiency of the GaInAs quantum well as evidence of the lateral confinement of carriers to the regions beneath the wells.

The smallest width of wires which they produced using this technique was 200nm. They did not state the resolution limits of this process, so whether it will be of use in obtaining clear evidence of quantum confinement remains an open question.

One obvious advantage of this process is that there is no need for any physical patterning, and therefore degrading, of the quantum well layer, only the layer above the quantum well. One disadvantage of this technique is that it is not integratable in this form. However, the use of strain within a structure combined with etching comparatively far away from the quantum well area is a promising route to achieving quantum confinement.

2.2.4 Selective barrier removal to obtain quantum wires

Gréus et al (1991) published work done using the InGaAs system ($In_{0.18}Ga_{0.82}As$) but they used GaAs as the barrier layer rather than the more commonly used InP. The technique they used relies on the patterning and removal by wet etching of the barrier layer (GaAs). They call this process *selective barrier removal* because the barrier - and not the quantum well - is removed by etching, although a small amount of the quantum well surface (~2nm) is inevitably removed because of the non-zero etch rate of InGaAs in the wet etch.

Confinement of the carriers to the quantum well layer is obtained by virtue of the high energy barrier of the uncovered quantum well compared with the masked quantum well region. These GaAs covered quantum well regions represent structures which are effectively buried, and so do not require subsequent overgrowth steps to improve the quantum efficiency. The active regions of these wires are also defect free because they are not subjected to etching or any other patterning technique.

They presented data which compares three different methods of producing quantum confinement: their own selective etch technique, deep wet etching (etching through the quantum wells), and deep dry etching. Their PL intensity results showed that the luminescence intensity of the wires fabricated by selective barrier removal remains comparable with that of the control sample down to smaller lateral sizes (100nm) than deep wet etched wires (approximately 500nm) or deep dry etched wires (1000nm).

PL spectra of 70nm and 35nm wires revealed blue shifts (shifts to higher energies) of approximately 7meV and 15meV respectively. These results are somewhat surprising because the blue shifts obtained are greater than expected. Indeed, for the 70nm wide wires no blue shift at all is expected (assuming a square confining potential). They attribute these stronger than expected blue shifts to uncertainties in determining the actual wire width, as compared

with the geometrical wire width (the confining potential is not necessarily square). A broadening of the emission spectra of narrow wires was reported and accounted for by variations in the widths of the wires over the array excited by the laser light.

2.2.5 Holographic photolithography to produce quantum wires

Miller et al (1989) used *holographic photolithography* to create arrays of quantum wires. This method involves a departure from the ubiquitous electron beam lithography technique which is commonly used to pattern wires. As the name suggests, holographic photolithography utilises photo-resist and an holography technique to pattern gratings. Holography is the term used when an interference pattern is produced by the crossing of two laser beams, producing small period gratings (typically 100nm) over comparatively large areas (for example, $5mm^2$). This process offers the advantage of producing large arrays of wires much quicker than conventional electron beam lithography is able to. After they patterned and developed an array of wires in the resist they used wet chemical etching to transfer the pattern to the single InGaAs quantum well layer. Afterwards, the wires were overgrown using atmospheric pressure MOVPE.

The data they presented relates to wires with lateral widths between 30 and 40nm. Characterisation of the wires was done by PL spectroscopy. An interesting aspect of their PL experiments was the fact that they only focused the laser beam spot to a size of 500μm, which is comparatively large. The reason for doing this was that it ensured that a large number of wires were sampled, and so large PL intensities and good signal to noise ratios were obtained, enabling them to vary the laser pump power over an incredible seven orders of magnitude.

They found that after regrowth the normalised PL intensity of the wires (taking the fill-factor into account) was 1.95 compared with a value of 1 for the control area. Although this might seem to indicate an increased luminescence efficiency this is not necessarily the case. They state that it is likely that electron-hole pairs will be captured from the InP areas between the wires, which would cast doubt on the validity of normalising the PL intensity by the fill-factor of the wires. Perhaps the best way of presenting the data is to say that the wire arrays emit with an integrated PL intensity approximately one third of that of the control area (without any correction or normalisation). They reported a 6meV shift to higher energies for these quantum wires which they ascribe to quantum confinement; although they did not discount the possibility that strain induced by the etching and/or regrowth stages may contribute to this energy shift.

This method of fabricating quantum wires appears to be quite attractive because of its ability to pattern large arrays very quickly and because of the low damage nature of wet etching. However, Miller et al (1989) did not state the resolution limits of this technique.

2.2.6 Lithography and wet etching to produce quantum wires

Naganuma et al (1990) and then Notomi et al (1991) published results based on electron beam lithography followed by *selective wet chemical etching*. An array of wires with a period of 150nm was written along a certain crystallographic axis, the <011> direction, of the InP using electron beam lithography. A selective, anisotropic etch was then used, which utilises the natural phenomenon of preferential etching of InP in one plane, to produce wires in the InP which have a reverse mesa shape, i.e. they are wide at the top and much narrower at the bottom. This technique permits the fabrication of wires whose lateral dimensions are much smaller than the original width defined by electron beam lithography.

Thus, this technique enables wires to be fabricated in a reproducible manner with minimal and uniform lateral dimensions (10nm); in addition, because a wet etch is used the surface damage should be low.

Naganuma et al (1991) reported CL experiments performed on wires fabricated using this technique and subsequently overgrown with InP. The smallest wires which they probed were 30nm wide. The CL spectrum of these wires showed a blue shift of approximately 9meV. The normalised integrated PL intensity of the wires (i.e. taking the fill-factor into account) was 0.25 compared with a value of 1 for the control area. They stated that this was indicative of a good quality wire with good interfaces between the wire and the overgrown InP.

Notomi et al (1991) reported a systematic study of arrays of wires whose widths varied from 10 to 80nm. They performed PL measurements of the wire arrays, which were overgrown with InP. This investigation is undoubtedly the most comprehensive study of wire widths as they vary from sizes below to sizes above the Bohr radius of the InGaAs heavy-hole exciton (approximately 30nm).

They obtained a PL signal from even the smallest wires (the smallest being a mere 10nm) and cited this as strong evidence that the fabrication process - in particular the wet etching stage - inflicts little damage on the quantum well layer. They omitted to give information on how the luminescence intensity changes with decreasing wire width, or whether the signal scales with fill-factor.

They observed a definite high energy shift with decreasing wire width, up to a maximum value of 50meV for the 10nm wide wires. They plotted the wire width versus energy shift for 25 different wire widths and found that the experimentally determined energy shift (from the PL spectra) was in good agreement with the calculated shift. This calculation assumed that the lateral confining potenetial was rectangular and finite. An extra shoulder feature which appeared at higher energies was observed on all spectra (except for the smallest wires) which they attributed to the second quantised level of the lowest (n=1) electron-heavy hole transition,

due to lateral quantization. However, there was a larger discrepancy between the experimental and theoretical energy shifts for this transition than for the main transition. They attributed this larger discrepancy to the higher level being complicated by band mixing or confinement effects.

Perhaps it is worth noticing that the spectra they published relating to the 10 and 20nm wide overgrown wires showed considerable broadening.

2.2.7 Lithography and ion beam milling to fabricate wires

Fabricating wires using electron beam lithography followed by argon ion milling or Ar/O_2 reactive ion beam etching has proved to be a popular method in the pursuit of quantum confinement.

Temkin et al (1987) used *electron beam lithography and argon ion milling* to fabricate wires down to 30nm wide. The PL spectrum showed a blue shift of 14meV although this shift changed with incident laser power, which lead them to conclude that perhaps only 6meV of the shift was caused by confinement, the rest by band-filling effects. The normalised, integrated (i.e. taking the fill-factor into account) PL intensity was approximately 0.02 compared with a value of 1 for the control area. This represents a reduction in PL intensity of almost 2 orders of magnitude. When the integrated PL intensity of the wires was plotted against the incident laser power (using logarithmic scales on both axes) the slope was linear, with a gradient of approximately 1. This smooth decrease in PL intensity with decreasing incident laser power implies that there is no significant non-radiative surface or defect recombination. They attributed the lower intensity to remnants of the etch mask screening the laser light.

Gershoni et al (1988) used the same technique to fabricate 35nm wide wires, which they probed using both PL and PLE. The PL spectrum exhibited a blue shift of 11meV which did not change with laser power. The PLE spectrum showed two additional peaks which they assigned to the excitonic transitions associated with lateral confinement in the x direction. They found that the PL intensity scales with fill-factor and cited this as confirmation of their previous statements that there is a negligibly low density of non-radiative recombination centres in argon ion milled wires of InGaAs.

Maile et al (1989) carried out temperature dependent luminescence studies of wires fabricated by *Ar/O_2 reactive ion beam etching RIBE* with widths between 5µm and 40nm. They stated that the quantum efficiency at high temperatures (room temperature) was predominantly affected by surface recombination and they invoke a "dead layer" (an optically inactive layer) concept to account for the quenching of luminescence from wires narrower than

40nm. The "dead layer" width was quoted as being approximately 19nm. This figure was obtained by fitting their luminescence intensity model to the experimental data, which indicated that the luminescence quenched when structures less than 40nm wide were fabricated. The defects which give rise to this "dead layer" are non radiative recombination centres which do not introduce a lateral barrier. Thus the PL spectrum of 40nm dots is not significantly different to that of 5000nm dots because the excitons are not confined by the "dead layer". Figure 2.1 shows how the luminescence intensity of their wires changes with geometrical wire width.

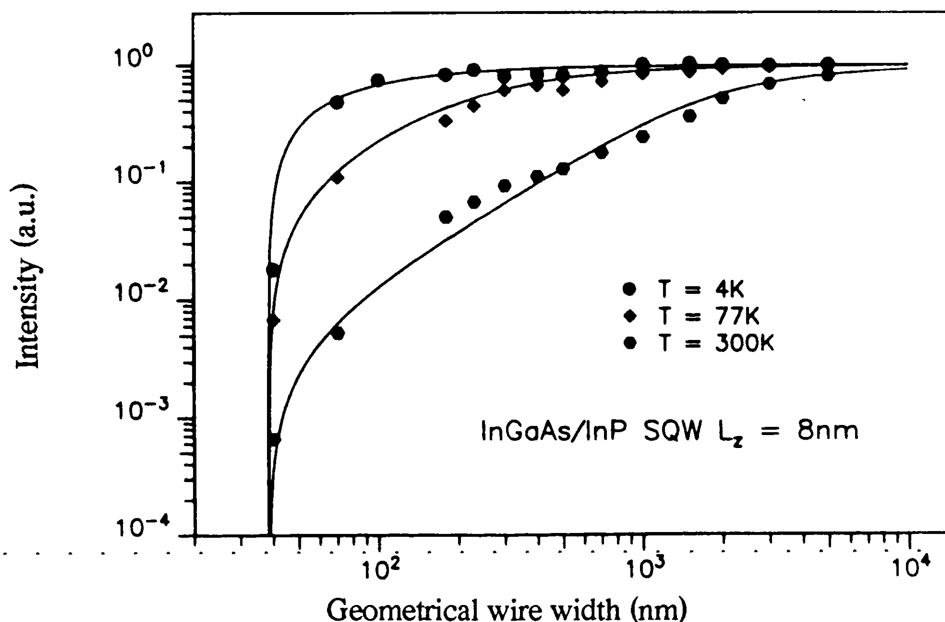

Figure 2.1 Wire emission intensity as a function of geometrical wire width. The points refer to experimental data and the lines refer to the calculated dependence (Maile et al, 1989)

A more recent study of the quantum efficiency of wires etched by *Ar/0₂ RIBE* was published by Lehr et al (1992). They compared the luminescence of a number of arrays of as-etched and overgrown quantum wires the widths of which varied from 800nm down to 65nm. The luminescence was obtained under both resonant and non-resonant excitation. In this case resonant refers to the selective excitation of the quantum well layer (InGaAs) and non-resonant refers to the excitation of both the quantum well and barrier layers (InGaAs and InP respectively).

After overgrowth the quantum efficiency was at least an order of magnitude higher than it was prior to overgrowth, which they attributed to suppression of the surface recombination at the active wire region boundaries and a reduction in the optically inactive layer thickness.

The use of resonant and non-resonant excitation enabled them to distinguish between carrier loss mechanisms in the barrier and in the active wire region. The quantum efficiency is

defined as the ratio of the emission intensities (under identical conditions) of the wire or dot structures to the control (mesa) area. An ideal quantum efficiency has a value of

$$\frac{I_{wire}}{I_{mesa}} = 1 \qquad 2.1$$

They find that resonant excitation yields greater values of quantum efficiency than non-resonant excitation, which suggests that non-radiative processes in the barrier strongly influence the quantum efficiency of the wire. Even the smallest overgrown wires (65nm) have a high quantum efficiency (0.84) when excited resonantly.

The difference in quantum efficiency for resonant and non-resonant excitation increases with diminishing wire width, which implies that the capture of carriers from the barrier also decreases with wire width. This difference in quantum efficiency for the excitation energies is always greater in the as-etched than in the overgrown wires, which suggests that overgrowth enhances carrier capture from the barrier.

Finally, they warned that models which are based on surface recombination at active wire boundaries are only valid when the quantum well material alone is excited, and not the well and barrier layers together. This could prove important because most of the PL measurements published have used non-resonant excitation conditions, which excite both the well and barrier layers.

2.2.8 Lithography and reactive ion etching to fabricate wires

Patillon et al (1990) used *electron beam lithography followed by CH_4/H_2 RIE* to fabricate wires with lateral dimensions down to 80nm. They performed both PL and PLE measurements on the samples, some of which were as-grown structures and others were overgrown with InP. The as-etched wires showed considerable broadening of the PL spectrum, with the presence of a high energy hump which they attributed to modifications of the relaxation mechanisms. After overgrowth, however, the PL spectrum displayed a FWHM comparable with that of the reference part of the sample. The PL spectrum showed a small (2meV) blue shift of the wires which they tentatively attributed to quantum confinement. These results highlight the difficulty in interpreting bumps and peaks in PL and PLE spectra. It would be useful if it could be ascertained why there is a shift in the peak position after overgrowth.

Izrael et al (1991) used *electron beam lithography followed by $CH_4/H_2/Ar$ RIE* to fabricate wires. They presented PL measurements on a single quantum well sample patterned with wires of 15nm lateral width. The PL spectrum revealed a 30meV high energy shift for these wires which is indicative of quantum confinement. They state that PL measurements on wires

between 60 and 100nm wide showed no shift in energy. The normalised PL intensity of the wires (i.e. taking the fill-factor into account) was approximately 0.13 compared with a value of 1 for the control piece of the sample.

Adesida et al (1992) fabricated wires 40nm wide using *electron beam lithography and CH_4/H_2 RIE*. They performed PL experiments and noted a high luminescence efficiency from the quantum wires down to 60nm (the signal was 70% of that of the control sample or a quantum efficiency of 0.7) and good emission from the 40nm wires (10% of that of the control sample) which suggests that their RIE process induces low damage in the etched wires. The PL spectrum of the 40nm wires showed no blue shift but it did have a broadened hump at higher energies which they could not account for.

Samuelson et al 1992 used *electron beam lithography, electron cyclotron resonance metal-organic reactive ion etching and wet chemical etching* to produce quantum wires down to 80nm wide. They presented 25K CL spectra of an unetched area and an area patterned with 80nm wide quantum wires. The CL spectrum of the wires was shifted to higher energies (blue shift) by approximately 10meV compared with the spectrum obtained from the unpatterned area. It is interesting to note that prior to the wet etch the CL spectra obtained exhibited a blue shift which varied across the sample. They attributed this variation in shift to strain induced by the residue which was left on top of the wires after etching. They stated that the brief wet etch removed this residue along with approximately 10nm of the wire surface, which removed the layer of material which was damaged during etching and also straightened the wire sidewalls. They reported that there was no loss of luminescence intensity after fabrication of the wires.

2.3 Fabrication of quantum dots

Compared with the abundance of literature on quantum wires the volume of literature published on fabricating quantum dots in InGaAs/InP material has been meagre. Perhaps the reason for this is related to the lower fill-factors associated with dots, and hence the signal intensities obtained are lower and more difficult to detect. Many of those techniques described above which are used to fabricate quantum wires are unsuitable for fabricating dots, but - in general- any method which can be used for dots can also be used for wires. The four methods for fabricating dots detailed below were also used by the authors for fabricating wires and these results have already been given under the quantum wire section above.

2.3.1 Direct growth of quantum dots

Galeuchet et al (1991) fabricated buried quantum dot arrays using *selective area MOVPE growth.* The smallest dots fabricated had a lateral width of approximately 150nm. The CL spectra obtained from the dots was shifted to lower energies, which they attribute to an increase in the indium content and an enhancement of the quantum well thickness in the buried InGaAs dots. The normalised integrated PL intensities of the dots (i.e. taking the fill-factor into account) are very large. For example, they quote a value of 4 for 280nm wide dots compared with a value of 1 for the control area. They claim that their quantum efficiency figures compare very favourably with those published by Maile et al (1989). They state that their normalised integrated PL intensity figures are between 3 and 6 times larger than those obtained by Maile et al (1989) for comparable dot sizes. However, it is possible that these dots capture electron-hole pairs generated in the InP under the original SiO_2 mask, thus artificially boosting the luminescence efficiency values. The size of dots grown (150nm) is too large to observe quantum confinement effects. Whether smaller dots can be grown by this method or not is unclear because the authors do not state if there are any fundamental limits to the minimum size of dot which can be grown by this technique.

2.3.2 Strain confinement of carriers to quantum dots

Kash et al (1989) applied their *strain technique* (see section 2.2.3 for details) to the creation of quantum dots. The 5K PL spectrum of an array of dots, each 400nm in diameter, showed a large (~10meV) shift to lower energies and exhibited a luminescence intensity which (after taking the fill-factor into account) has a value of 2 or 3 compared with a value of 1 for the control region. They attributed the shift to lower energies (red-shift) to the creation of larger potential wells for excitons.

However, dots which are 400nm in diameter are at least an order of magnitude larger than the 3D Bohr radius and so quantum size effects should not be dominant.

2.3.3 Lithography and ion beam milling to produce dots

Temkin et al (1987) fabricated wires (see section 2.2.7) and dots using *electron beam lithography and argon ion milling*. The 6K PL spectrum of the dot array showed an energy upshift of approximately 6meV. The spectrum displayed considerable broadening, which they attributed primarily to variations in the dot size over the array but they did not exclude other possible explanations.

2.3.4 Lithography and reactive ion etching

Patillon et al (1990) used *electron beam lithography and CH_4/H_2 etching* to fabricate quantum dots of 80nm width. They performed both PL and PLE experiments on the dot arrays and found a small (5meV) energy upshift on the PLE spectrum and a high energy hump on the PL spectrum. This high energy hump occurred at a higher energy than the lowest electron-heavy hole transition and was attributed to modifications of the high energy levels and perhaps even luminescence associated with an electron-light hole transition.

2.4 Summary of literature published on quantum wires and dots

The above summary of the work done on quantum wires and dots plainly reveals the inconsistency of the results obtained. In order to show this more clearly, table 2.1 summarises the wire widths and the energy shifts (to higher energies) obtained from these wires. The dash (-) indicates that the information required was not given in the reference.

Geometrical wire width (nm)	Reference (first author and year)	Fabrication method	Energy shift (meV)	Intensity compared with mesa	Overgrowth
35	Miller '92	Wet etching	6	1.95	√
30	Naganuma '90	Wet etching	9	0.25	√
10	Notomi '91	Wet etching	50	-	√
20	Notomi '91	Wet etching	10	-	√
40	Notomi '91	Wet etching	5	-	√
30	Temkin '87	Ar milling	6	0.02	X
35	Gershoni '88	Ar milling	11	1	X
80	Patillon '90	RIE	2	0.4	√
15	Izrael '91	RIE	30	0.13	X
40	Adesida '92	RIE	0	0.1	X
80	Samuelson '92	ECR RIE	10	1.4	√

Table 2.1 Summary of published wire widths and corresponding energy shifts

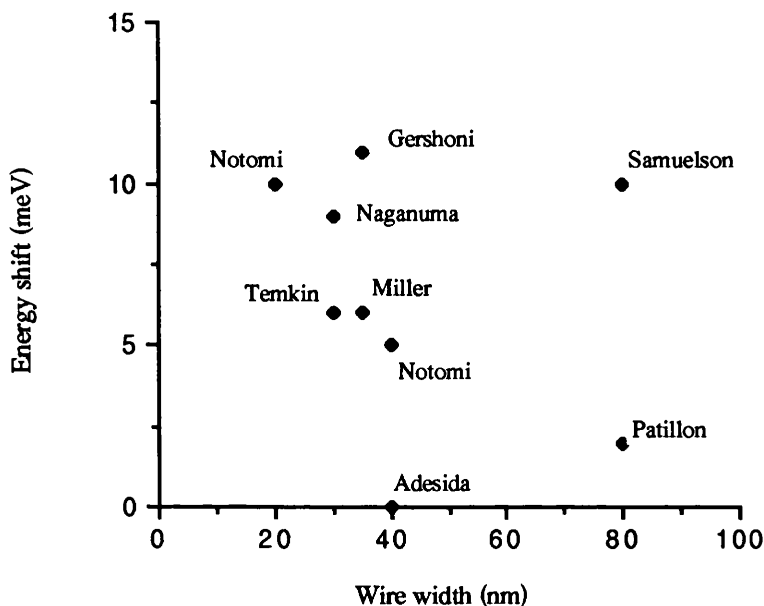

Figure 2.2 Graph of PL peak energy shift versus wire width

Though much work has been done to obtain confinement using the InGaAs/InP material system there is still much confusion and debate over the processes which take place within the wire and dot structures. Many groups have reported energy shifts - some to higher energies, others to lower energies - but it is difficult to ascertain exactly what is happening or to attribute modifications of the PL spectra with any degree of certainty. Matters are complicated by the difficulty in obtaining any absorption or PLE measurements. Even a cursory glance at the above literature review is sufficient to reveal the absence of PLE measurements from all but a few of the papers. PLE or absorption data provides invaluable information regarding the internal energy states, and would greatly assist in ascribing any changes in the PL spectra.

The most lucid work done seems to be that of Notomi et al (1991) who use crystallographic wet chemical etching and have published a study of the energy shifts for various quantum wire widths within the region of greatest interest (10 to 80nm).

Some research groups rely on damage induced during the processing stages to lower the "electronic" width of the quantum wires or dots. Whilst this may give rise to energy shifts it is not an elegant way of achieving quantum confinement because of the inherent difficulty in ascertaining the "electronic" width (which requires the use of magneto-optics).

This present work uses electron beam lithography and RIE to fabricate dots and so it is unlikely to induce as little damage as wet etching would, but it does have the advantage of being more amenable to the fabrication of dots than wet etching.

References

Adesida I, Chang H, Ballegeer D, Liu X, Bishop S, Caneau C and Bhat R 1992 Proc SPIE Symposium on Compound Semiconductor Physics and Devices vol 1676

Cox H M, Lin P S, Yi-Yan A, Kash K, Seto M and Bastos P 1989 Appl. Phys. Lett. 55 (5) 472-474

Dingle R, Wiegmann W and Henry C H 1974 Phys. Rev. Lett. 33 (14) 827-830

Galeuchet Y D, Roentgen P, Nilsson S and Graf V 1990 in: Science and Engineering of One- and Zero- Dimensional Semiconductors, Eds S P Beaumont and C M Sotomayor Torres, Plenum Press, New York, 1 - 9

Galeuchet Y D, Rothuizen H and Roentgen P 1991 Appl. Phys. Lett. 58 (21) 2423 - 2425

Gershoni D, Temkin H, Dolan G J, Dunsmuir J, Chu S N G and Panish M B 1988 Appl. Phys. Lett. 53 (11) 995 - 997

Gréus Ch, Forchel A, Straka J, Pieger K and Emmerling M 1991 J. Vac. Sci. Technol.B9 (6) 2882 - 2885

Izrael A, Marzin J Y, Sermage B, Birotheau L, Robein D, Azouley R, Benchimol J L, Henry L, Thierry-Mieg V, Ladan F R and Taylor L 1991 Japanese Journal of Applied Physics 30 (11B) 3256 - 3260

Kash K, Bhat R, Mahoney D D, Lin P S D, Scherer A, Worlock J M, Van der Gaag B P, Koza M and Grabbe P 1989 Appl. Phys. Lett. 55 (7) 681 - 683

Lehr G, Bergmann R, Rudeloff R, Scholz F and Schwiezer H 1992 Appl. Phys. Lett. 61 (5) 517 - 519

Maile B E, Forchel A, Germann R and Grützmacher D 1989 Appl. Phys. Lett. 54 (16) 1552 - 1554

Miller B I, Shahar A,, Koren U, Corvini P J 1989 Appl. Phys. Lett.54 (2) 188 - 190

Naganuma M, Notomi M, Iwamura H, Okamoto M, Nishida T and Tamamura T 1990 J Crystal Growth 105 254 - 259

Notomi M, Naganuma M, Nishida T, Tamamura T, Iwamura H, Nojima S and Okamoto M 1991 Appl. Phys. Lett. 58 (7) 720 - 722

Patillon J N, Jay C, Iost M, Gamonal R, André J, Soucail B, Delalande C and Voos M 1990 Superlattices and Microstructures 8 (3) 335 - 339

Samuelson L, Georgsson K, Gustafsson A, Maximov I, Montelius L, Nilsson S, Seifert W and Semu A 1992 Proc SPIE Symposium on Compound Semiconductor Physics and Devices vol 1676 154 - 160

Temkin H, Dolan G J, Panish M B and Chu S N G 1987 Appl. Phys. Lett. 50 (7) 413 - 415

Weiner J S, Wang Y L, Temkin H, Harriot L R, Hamm R A and Panish M B 1990 J. Vac. Sci. Technol. B8 (6) 1371 - 1373

Chapter 3
Pattern delineation and lithography

3.1 Lithography - General principles

Lithography, in general, is a process used to create a pattern consisting of lines, squares, rectangles, etc. in a material which covers the sample surface. The material - usually an organic substance (resist) spun onto the sample to ensure uniform thickness - is sensitive to the radiation used in the lithographic process.

There are several different types of lithography, including x-ray lithography (Spears and Smith, 1972), ion beam lithography (Komuro et al, 1979), electron beam lithography (Watt, 1985) and optical (photo) lithography (e.g. Sze, 1988). Of these, the most commonly used process, particularly in industry, is photolithography.

In photolithography, ultra-violet light is projected through a mask (usually emulsion on glass or chromium) which has patterns 'cut' out of it. The light is incident on the resist, thus producing an image of the mask on the resist.

The minimum feature size which can be written using photolithography is chiefly determined by the wavelength of the radiation used, i.e. it is a diffraction limited process. Optical lithography typically uses an ultra-violet light source which emits light in the wavelength range 300 - 500nm and as a result of this the minimum achievable resolution is limited to approximately 0.3μm. Linewidths of this size are far too large to be of use in fabricating structures exhibiting quantum size effects (which need to be less than 100nm) and so optical lithography could not be used for this work.

In order to overcome the limitation due to the photon wavelength of ultra-violet light, electron beam lithography was used throughout this research. In a typical electron beam lithography machine the electron wavelength (which is dependent on its velocity) is many orders of magnitude lower than that of the wavelength of UV light.

Table 3.1 shows values of electron mass and wavelength for various electron velocities (Watt, 1985).

Voltage (volts)	Velocity (relative to velocity of light)	Mass (relative to rest mass)	Wavelength (nm)
1	0.0020	1.0000020	1.226
10	0.0063	1.0000196	0.3878
100	0.0198	1.0001957	0.1226
1000	0.0625	1.001957	0.03876
10 000	0.1949	1.01957	0.01220
100 000	0.5482	1.1957	0.00370

Table 3.1 Wavelengths and masses of moving electrons

The values of electron wavelength in table 3.1 show that in electron beam lithography the resolution (which is 2nm in good systems) is not limited by diffraction effects. Ultimately, the resolution of electron beam systems is limited by the beam size (which is influenced by abberations introduced by the electron optics), the lateral secondary electrons which are caused by electron scattering of the main beam, and development and related effects.

The relationship between accelerating voltage and electron wavelength is clearly shown in table 3.1: the higher the accelerating voltage the lower the electron wavelength. Using only this information it would appear that those electron beam lithography machines with high gun voltages would have better resolution than their lower voltage counterparts. This is usually true, not because the lower electron wavelengths associated with the higher energy electrons lead to reduced diffraction effects (since the resolution of electron beam systems is not diffraction limited), but because of the higher energies of the electrons, as will be discussed in section 3.2.4.

In contrast to photolithography, electron beam lithography is usually (though not always) a direct writing process: this means that there is no need for a mask because design patterns are entered as software files which the computer uses to control the electron beam. This gives tremendous flexibility in designing and altering patterns.

3.2 Resists

A resist is usually an organic substance which is sensitive to a particular kind of radiation. In photolithography the resist used is sensitive to photons, and in electron beam lithography it is sensitive to electrons.

There are certain desirable qualities of a good electron beam resist. It must be capable of being spun onto a sample, producing a smooth pinhole-free film, and be easily removed after subsequent processing stages. The resist should only be sensitive to electron radiation. The sensitivity of a resist is a measure of how much electron dose is required to produce a lithographically useful image (Deckman and Dunsmuir, 1983). In theory, low electron doses are preferable, otherwise the lithography process would be time consuming because of the direct writing nature of electron beam lithography. Finally, the resist should be capable of high resolution in order to utilise the high resolution of the electron beam lithography machines. As is often the case a trade-off is required because not all of these qualities are present in any one resist, e.g. the resists which have the highest sensitivity do not have the best resolution (Wilkinson and Beaumont, 1986) and so the choice of resist will be determined by the particular needs of the application. In this research high resolution is of paramount importance so the resist was chosen with this in mind.

Two types of resist, negative and positive, are in common use. Each has its particular application and usefulness, its own advantages and disadvantages, and both were used during the course of this research.

3.2.1 Negative resist

Negative resists are polymers which behave in such a way that any area exposed to electron radiation becomes insoluble in a developer whereas the unexposed areas are dissolved. This happens because the resist is composed of many short-chain resist molecules. Exposure to electron radiation causes these chain-like molecules to link together in a network forming larger molecules which have higher molecular weights than the unexposed resist. This is called cross-linking (Roberts, 1976). By choosing a suitable developer the areas of low molecular weight (the unexposed areas) are dissolved whereas the areas of high molecular weight (the exposed areas) remain because they are insoluble in the developer.

3.2.2 Positive resist

As suggested by the name, positive resist works in the opposite way to negative resist. Areas of positive resist exposed by electron beams are dissolved by the developer whereas the areas which were not exposed remain. Positive resist consists of long-chain resist molecules. When subjected to electron bombardment these long-chain molecules are fragmented and broken down to short chains, a process called chain scission (Roberts, 1976). These short-chain molecules have lower molecular weight than their long-chain counterparts and so can be dissolved in a suitable developer (a developer which dissolves areas of low molecular weight

but not areas of high molecular weight). Figure 3.1 shows the operation of both positive and negative resist.

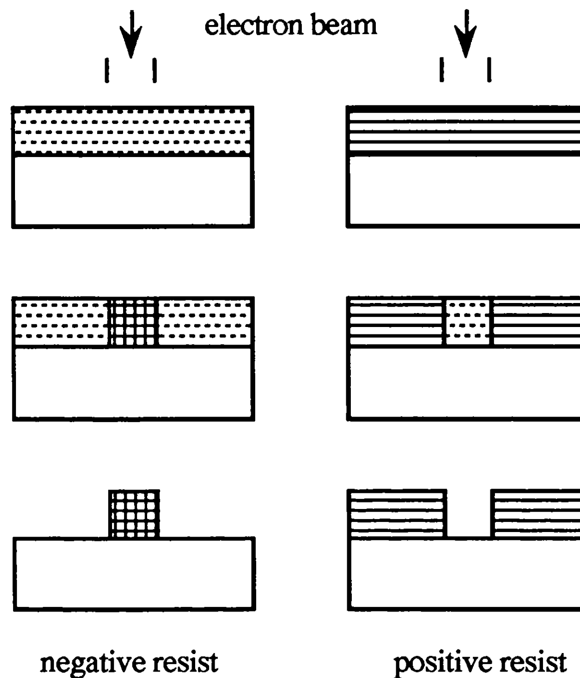

Figure 3.1 Positive and negative resist operation

3.2.3 Resist exposure

It has been stated (section 3.1) that electron beam machines can have resolutions of 2nm but this does not mean that 2nm wide lines can be written on any resist regardless of its thickness or chemical composition; other factors become important when small sizes are to be patterned on a resist. These factors include the thickness of the resist, the size of the resist molecules, the number of sites to be patterned in an area and how closely spaced these sites are. In order to understand how these factors will influence the resolution attainable it is necessary to consider electron scattering.

3.2.4 Electron scattering - the proximity effect

In electron beam lithography a narrow beam of electrons (sometimes as small as 1nm in diameter) is used to expose an area of resist. However, as this narrow beam enters the resist it is scattered by both the resist and the substrate atoms. When the electrons are scattered inelastically secondary electrons are produced. These secondary electrons usually have much lower energies than the electrons in the primary beam and are thought to be responsible for the exposure of the resist (Wilkinson and Beaumont, 1986).

When the primary beam is scattered by the resist then small angle forward scattering results. This inevitably broadens the narrow beam and causes exposure of an area larger than the original beam diameter. As the thickness of the resist increases forward scattering will increase the width of resist exposed. This explains why thinner resists are generally capable of higher resolution than their thicker counterparts.

Another effect which needs to be considered is the backscattering of electrons by the substrate. Unlike scattering due to the resist, substrate scattering causes electrons to scatter over a larger area, thus creating a background exposure over an area considerably broader than the main beam diameter. This is important because it suggests that the exposure required for two features which are close together will be different to the exposure they would require if they were much further apart. Both of these effects (small angle forward scattering and backscattering) are shown in figure 3.2 (Craighead, 1986).

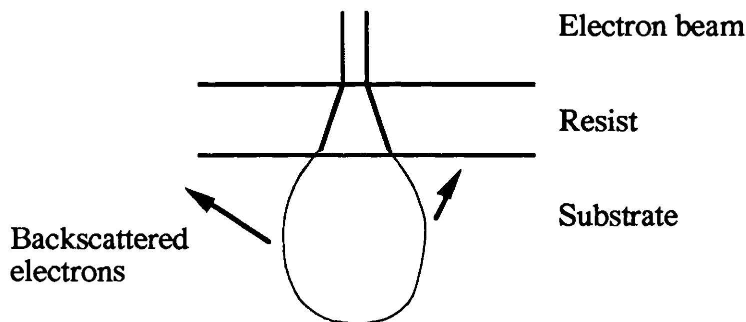

Figure 3.2 Diagram of forward scattering and backscattering of electrons

By using electron beams which have high particle energies (50-100kV) the forward scattering distribution is narrowed and the backscattered electrons are smeared out over a much larger area (Beaumont, 1991). It is for this reason (and not because of electron wavelength considerations) that higher accelerating voltages (e.g. 100kV) are used on electron beam machines in order to obtain high resolution (<30nm) lithography.

Having considered electron beam lithography, resist types, and factors affecting electron beam machines in general, the particular electron beam machines used in this research will now be considered.

3.3 PSEM500 electron beam machine

Three electron beam lithography machines were used during the course of this research, the first of these was the PSEM500, which was used for the initial two years because it was the only one available. The PSEM500 system at Glasgow University is a scanning electron microscope modified to facilitate electron beam lithography. The maximum accelerating

voltage available is 50kV, the nominal spot size can be varied from 1μm down to 8nm, and the range of magnification is from 20x to 80 000x. Table 3.2 shows some frame and pixel sizes for certain useful magnifications on the PSEM500. A diagram of the PSEM500 lithography system is shown in figure 3.3.

magnification	x pixel size	y pixel size	x frame size	y frame size
5 000	7.3 nm	5.4 nm	25 μm	22 μm
1 250	28 nm	21.3 nm	115 μm	87 μm
80	400 nm	317 nm	1640 μm	1300 μm

Table 3.2 Frame and pixel sizes and corresponding magnifications for PSEM500

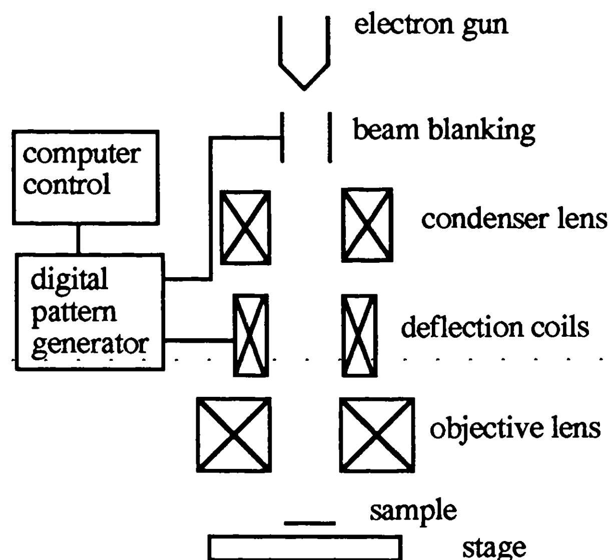

Figure 3.3 Modified PSEM500 lithography system

The magnification (given in table 3.2) is an important parameter because it determines the size of frame to be exposed. This frame is divided into an array of 4096 by 4096 pixels so the higher the magnification the smaller the pixel size. However, with increasing magnification the frame size decreases. The highest useful magnification for writing dots is 5000x because at this magnification the pixel size is less than the lowest nominal spot size.

3.3.1 Fabrication process for PSEM500

To pattern very small (100nm) features using electron beam lithography it is critical to focus accurately on the sample surface. To simplify the focusing process - and to make it more accurate - it is a good practice to pattern large alignment marks on the sample; these marks also

serve to locate the small patterned areas when performing PL experiments. Alignment marks should be made of a metal with a high atomic number because the number of backscattered electrons increases sharply with atomic number (Watt, 1985). A suitable material for alignment marks is gold, due to its ease of evaporation and high atomic number.

A sample of quantum well material, usually 5mm square, was cleaned using the following standard process: a 5 minute soak in trichloroethylene, followed by a 5 minute soak in methanol, followed by a 5 minute soak in acetone, followed by a 5 minute soak in isopropyl alcohol, all performed in an ultrasonic bath.

After this cleaning/de-greasing process, positive resist was spun at 5 000rpm producing a resist layer 1700nm thick, which was then baked for 12 hours at 180°C. The positive resist used was poly(methyl methacrylate) of molecular weight 185 000. This consisted of 18% BDH dissolved in chlorobenzene (Adams, 1990). Alignment marks were patterned using electron beam lithography, the resist was developed in developer consisting of one part of MIBK [methyl iso butyl ketone] to one part of IPA [isopropyl alcohol] at 23°C for one minute, and blown dry with nitrogen gas.

A layer of nichrome 20nm thick was evaporated onto the sample for good adhesion followed by a 150nm thick layer of gold. A "lift-off" was then performed by soaking the sample in acetone, which dissolves the resist and leaves only the nichrome/gold alignment marks. This "lift-off" process is shown in figure 3.4.

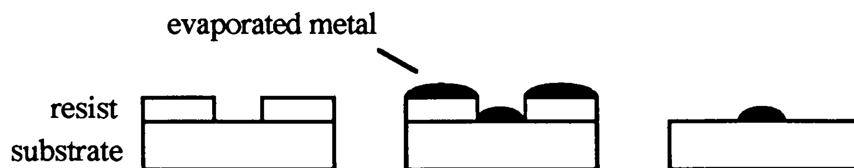

Figure 3.4 The "lift-off" process

There is a disadvantage associated with depositing gold alignment marks which becomes evident when performing photoluminescence measurements of small dots. The gold marks act as effective dry etching masks for the underlying quantum well material and so when high laser powers are used in PL experiments - as frequently occurs when trying to record the low intensity signals emanating from small quantum dots - luminescence is detected from the underlying material which obscures the true signal from the dots. For this reason it was decided to use wet etched alignment marks.

A suitable wet chemical etch should have a slow etch rate and be non-selective between InP and InGaAs. The etch used was a mixture of concentrated hydrochloric acid, concentrated ethanoic acid and hydrogen peroxide (35%) mixed in the ratio of 1:1:1 (Adachi et al, 1982). The actual mix quantities were:

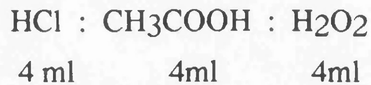

The sample was etched in this solution (at room temperature) for 1 minute, giving an etch depth of approximately 1.5μm. These wet etched alignment marks ensured that there would be no stray luminescence, but they did not serve as good marks for focusing the PSEM500; presumably this is because the etched sidewalls are smooth and rounded and so do not give an abrupt edge. Figure 3.5 illustrates the wet etch process

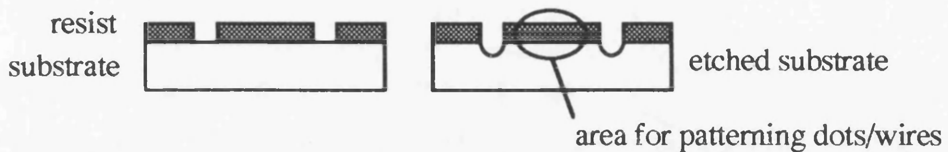

Figure 3.5 Wet etched alignment marks

Figure 3.6 shows a micrograph of the wet etched alignment marks.

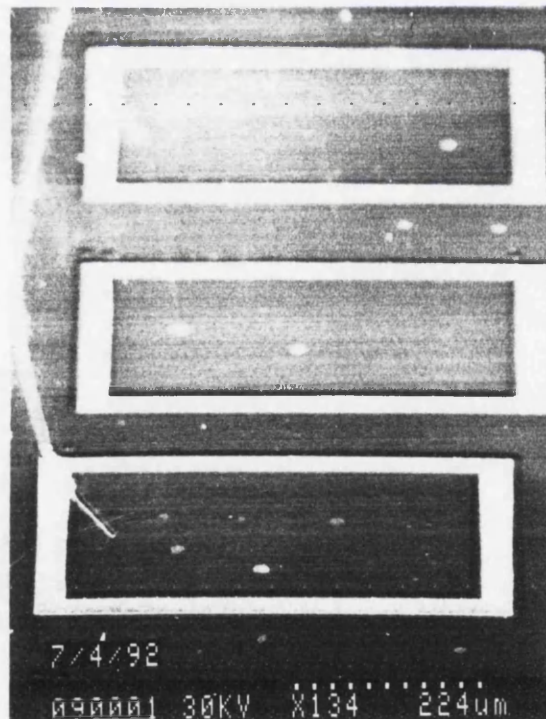

Figure 3.6 Wet etched rectangular alignment marks

Whether a wet etched or gold alignment mark was used the next stage was the same, i.e. to pattern the area within the rectangular alignment marks with quantum dots or wires.

High resolution negative resist of molecular weight 11 000 (8% HRN dissolved in Microposit thinner) was spun at 7 000rpm onto the sample surface producing a layer 110nm thick. The resist was baked for at least 3 hours at 120°C following which dots or wires were patterned. After exposure, the resist was developed using MIBK for 15 seconds then IPA for 15 seconds, followed by MIBK for a further 15 seconds and IPA again for 15 seconds. The remaining resist served as a suitable mask for dry etching. This process and the positive resist patterning process are illustrated in figure 3.7, the words in bold indicate process stages.

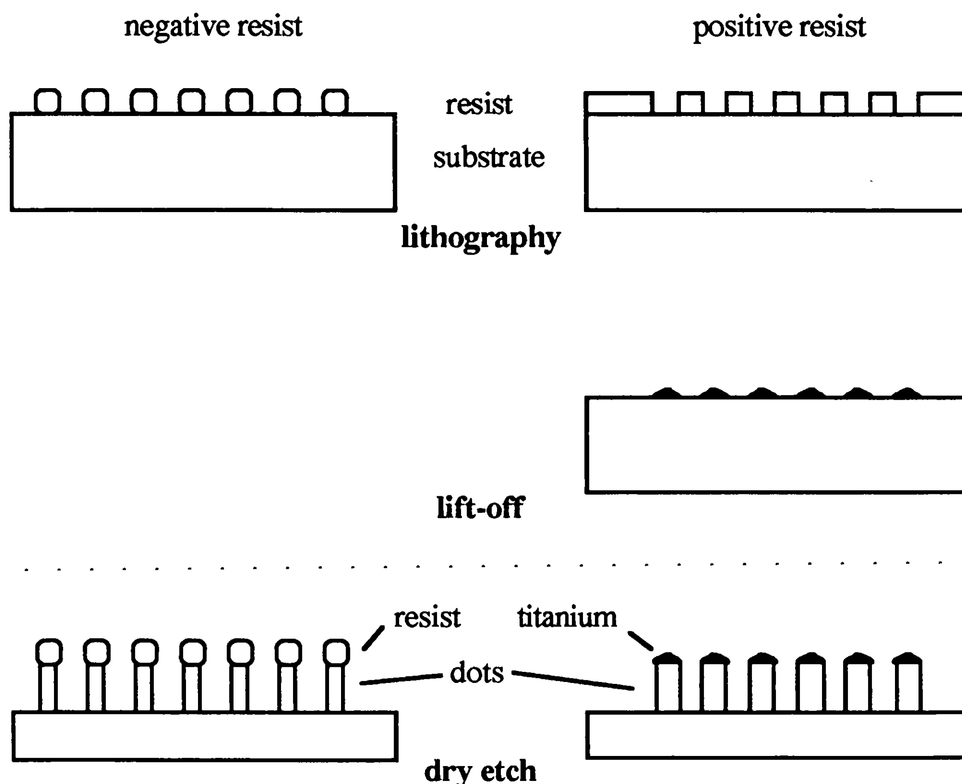

Figure 3.7 Fabrication of dots using positive and negative resists

Table 3.3 gives details of magnifications, spot sizes, pixel separation and exposure dose for some of the dot files used for patterning 8% HRN negative resist (these dot files were originally developed by Arnot, 1990).

Magnification	Dot size (nm)	No. of pixels	Exposure dose (μCcm^{-2})	Pitch (pixels)
5000	60	4x4	9000	50x65
5000	100	9x12	2000	82x108
2500	250	7x12	2000	52x68

Table 3.3 Details of exposure values for dot files using PSEM500

3.3.2 Sample layout and design

The sample layout was the same as that which was used previously by Arnot (1990). It was designed to make the PL experiments as simple as possible by arranging the arrays in two columns. This simplifies the PL experiments because with the particular optical cryostat used for this research it was easier to adjust the laser spot in the vertical direction than in the horizontal direction. It was necessary when designing a layout to include unpatterned areas - called mesas - which provide an area of original material for comparison with the etched areas. Ideally, these mesas should be located as closely as possible to the patterned areas, without being so close as to contribute stray luminescence when the patterned area is excited by the laser during PL experiments. The sample layout chosen has the advantage of having a mesa close to every dot array, so that spurious results are not recorded which are due to shifts in the PL peak position across the wafer. Figure 3.8 shows a diagram of the sample layout, and figure 3.9 is a micrograph of an actual sample.

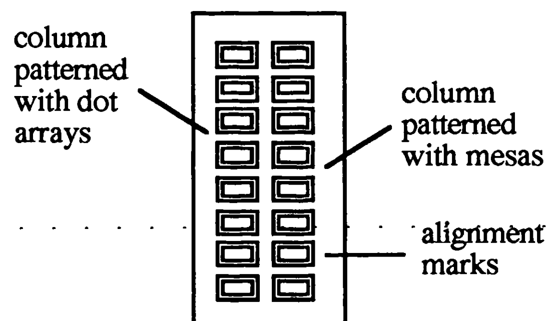

Figure 3.8 Sample layout for use with PSEM500

3.3.3 Disadvantages of the PSEM500

There are a number of disadvantages associated with the PSEM500. Not only is it slow at writing patterns - partly due to its low beam current - but, more importantly, its minimum linewidth is comparatively large.

By trial and error it was found that the inherent resolution of 8% HRN resist was approximately 60nm. This could be reduced by using a negative resist with a lower percentage content of HRN, such as 4% HRN (Thoms et al, 1988), but this resist would be too thin to work as an effective etch mask during the dry etching process. However, using positive resist together with the lift-off technique, linewidths down to 40nm can be obtained using the PSEM500; although this is still much greater than the inherent resolution limit of the positive resist. Although the PSEM500 has a nominal spot size of only 8nm, in practice it was suspected that this value was never really attained.

Considering the fact that quantisation effects only become apparent (dominating the luminescence spectra) as the lateral sizes of the dots approach the exciton Bohr radius (for InGaAs this is approximately 35nm at 4K), it seems unlikely that the PSEM500 could write dots which are sufficiently small to exhibit shifts due to quantisation.

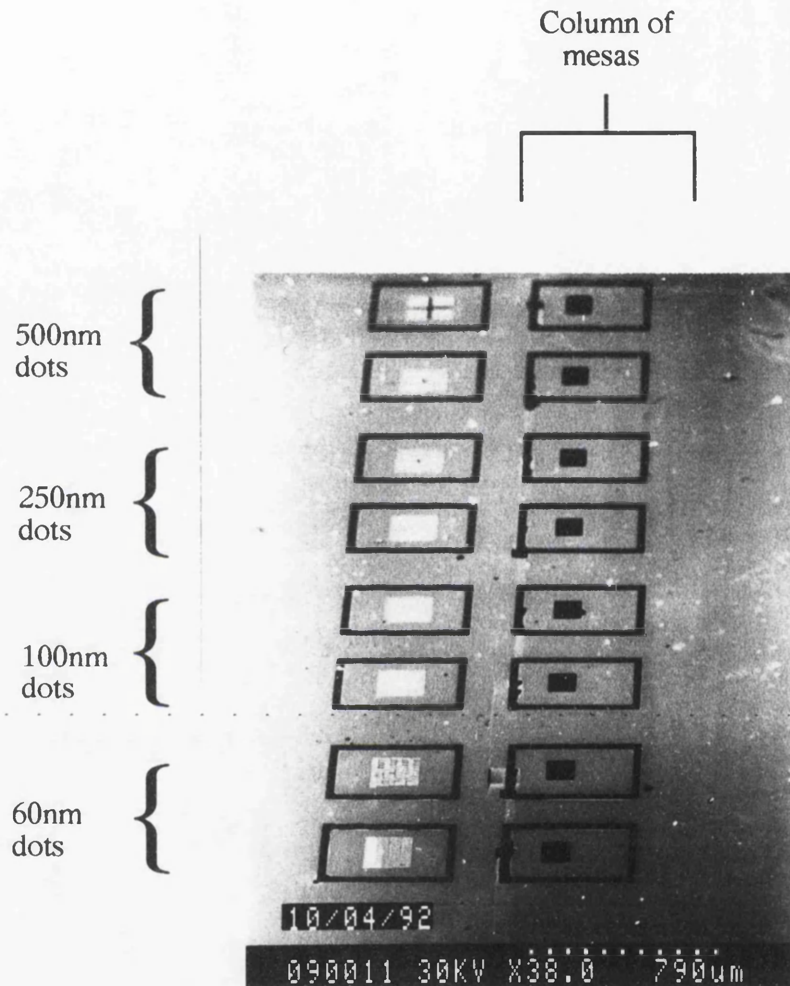

Figure 3.9 Micrograph of sample layout

Another problem associated with the PSEM500 concerned the need to pattern comparatively large (with respect to the frame size) areas with dots. Obtaining dots with diameters less than 100nm requires a magnification of 5 000 x, which gives a frame size of approximately 25 x 20μm. Performing PL measurements successfully requires patterned areas of at least 100μm square, and preferably 200μm square. Creating arrays of these dimensions requires "stitching" of the frames together. This might seem trivial, but what complicates matters is the fact that there is, not surprisingly, a positional error whenever the stage is moved; it is this error that causes the problems.

The disadvantage of the stitching technique lies in the inability of the PSEM500 to align adjacent frames to the stringent specifications required.

Stitching eighty frames together usually results in lines which resemble 'wires' where two frames overlap, and areas with no dots where frames do not quite touch each other. The latter problem is not too serious, it merely results in a slight change to the actual fill-factor and a lower luminescence signal. However, the creation of 'wires' presents a more sinister problem because it is possible that these pseudo-wires will emit with greater luminescence efficiency than the dots, rendering any luminescence intensity measurements useless.

A final problem connected with the fabrication process was the difficulty of focusing on the wet etched alignment marks. Obtaining an accurate focus was troublesome because the wet etched walls were very smooth, and there was little contrast between the etched and unetched areas. This focusing problem had serious ramifications because the depth of focus on electron beam lithography machines is small and when tiny feature sizes are being patterned the focus is critical.

Though none of the above mentioned disadvantages was intolerable, their cumulative effect represented a serious hindrance to the reproducible fabrication of small dots over large areas. However, by using another electron beam lithography machine, the Jeol 100 CXII, most of these problems were overcome.

3.4 Jeol 100 CXII electron beam machine

Unlike the PSEM500, the Jeol 100CXII is a converted transmission electron microscope (TEM) with a scanning attachment, which was extensively modified for use as a lithography system. Figure 3.10 shows a diagram of the column of the Jeol 100CXII.

The Jeol 100CXII has a maximum accelerating voltage of 100kV and a spot size of approximately 2nm (which it probably attains, unlike the PSEM500) which gives it greater resolution than the PSEM500. Its microscope functions and optics are completely computer controlled, and owing to its design the Jeol has larger electron beam currents for a particular spot size than the PSEM500, hence it is able to scan patterns much quicker than the PSEM500.

In a similar way to the PSEM500, the Jeol uses a frame which is divided into an array of 4096 by 4096 pixels. To pattern very fine lines (less than ~30nm) high magnifications (2400 or greater) are required in order to reduce the pixel size. However, with an increased magnification comes a diminished frame size, which introduces the problem of having to step and repeat the pattern more often than before in order to cover the array size required (usually at least 200μm squared for PL experiments).

This problem was eased however when the scan generator was modified. One of the modifications to the scan generator enabled more pixels to be addressed in the same frame

size. Previously, only 4096 by 4096 pixels could be addressed, but with the modification it was possible to set the scan generator so that it would allow 8192 by 8192 pixels to be addressed. This had the effect of reducing the pixel size (four new pixels were the same size as one old one) without reducing the frame size.

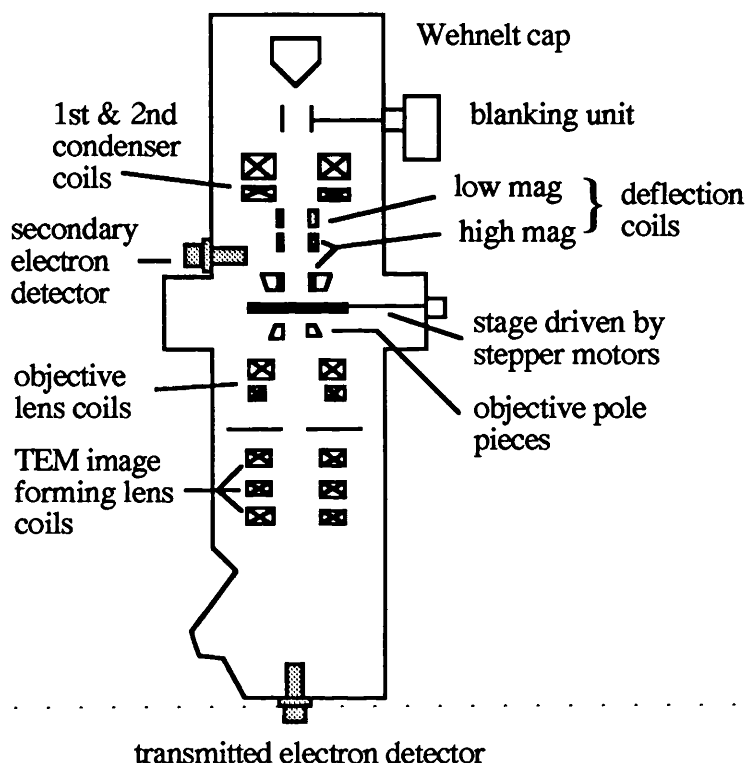

Figure 3.10 Modified Jeol 100CXII (from Jeol instruction manual)

Table 3.4 shows some frame and pixel sizes for certain useful magnifications on the Jeol, which relate to a frame composed of 4096 by 4096 pixels. When small dots (down to 35nm) were patterned using a magnification of 1200, the useful Jeol frame size was approximately 115μm by 80 μm. In practice, this enabled areas of 400μm square to be patterned with small dots, which was ideal for spectroscopy. Another advantage of the large frame size was the reduced effect of stitching on the actual fill-factor.

magnification	x pixel size	y pixel size	x frame size	y frame size
600	66.7 nm	54.9 nm	273 μm	225 μm
1200	33.4 nm	27.9 nm	137 μm	113 μm
2400	16.7 nm	13.8 nm	68 μm	56 μm

Table 3.4 Frame and pixel sizes and corresponding magnifications for the Jeol 100CXII

3.4.1 Fabrication process for Jeol 100CXII

Alignment marks are an essential part of the fabrication process when patterning samples using the PSEM500, but they are not necessary when patterning samples using the Jeol. The reason for this relates to the different ability of each machine to focus on the sample surface.

The standard method of focusing the Jeol is to focus at each corner of the sample. The Jeol then calculates the best-fit plane through the four points and gives the deviation of each point from the best-fit plane. This verifies the consistency of the focus across the sample.

Using the Jeol it is relatively simple to focus on scratches made in the resist; and since the patterned areas are large (400μm square) it is simple to locate them when doing PL experiments, thus obviating the need for alignment marks. With alignment marks redundant, the associated problems of stray luminescence from underneath the gold alignment marks and the difficulty of focusing when using wet etched alignment marks disappear.

By not using alignment marks several stages are removed from the over-all fabrication process, which is advantageous because with an increased number of process stages comes an increased probability of sample failure during the fabrication process.

Only positive resist was used on samples patterned by the Jeol. To ensure maximum posssible resolution and to aid the lift-off process very thin layers of PMMA were used in a bilayer structure. The lower layer of PMMA had a molecular weight of 185 000 (it consisted of 2.5% BDH dissolved in chlorobenzene) and the upper layer had a molecular weight of 350 000 (it consisted of 2.5% Elvacite dissolved in O'xylene). The higher the molecular weight of resist, the higher the exposure dose needs to be to expose it completely. Thus the linewidth of the upper layer of resist is narrower than the lower resist layer. This bi-layer resist structure raises the probability of performing a successful lift-off by giving an undercut profile, as shown schematically in figure 3.11 (Mackie et al, 1982). The combined thickness of the bi-layer resist structure was approximately 50nm.

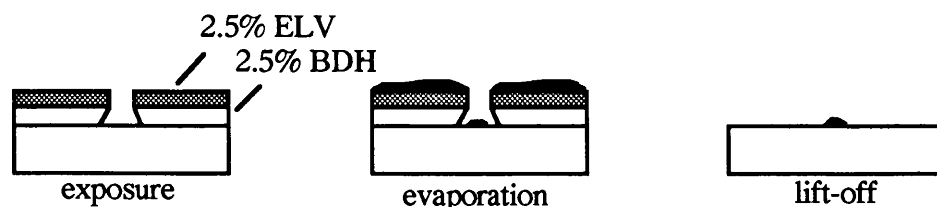

Figure 3.11 Lift-off with bi-layer resist

Once the resist had been patterned by the Jeol the next step was to evaporate a suitable material for use as a mask during the dry etch process.

The choice of this material was not trivial. In addition to the fundamental property of being resistant to etching during the rf discharge, a mask must also be amenable to any experiments which will be performed subsequent to the dry etching process.

If PL spectroscopy is to be done then it is vital to have an optically transparent mask such as negative resist or a strontium fluoride based mask (a mixture of 92% SrF_2 and 8% AlF_3 by weight). When patterning samples using the Jeol, the strontium fluoride based powder was favoured because it is easily evaporated and can be removed very rapidly in dilute HCl. This ability to remove the mask is essential if overgrowth is to be performed. Throughout this research the amenability of patterned samples to be overgrown subsequent to fabrication was a strong consideration.

As an alternative, a very thin layer (9nm) of nichrome was used as a mask. The aim of this was to discover whether a thin layer of metal would be transparent. The nichrome mask had the advantage of good adhesion, but it was not completely transparent; it reduced the PL signal by approximately 50%. This reduction in PL signal is unacceptable because the PL signal from small dots is difficult enough to detect without unnecessary attenuation introduced by the mask. Thus the need for an optically transparent mask precludes the use of even a thin nichrome mask.

If Raman scattering experiments are to be done, to investigate surface phonon effects, then a transparent mask is not required. A mask which is highly resistant to etching (e.g. titanium) is more suited to these experiments because very tall structures are necessary, and these need longer etch times than the standard quantum dot process.

A final caveat about the positive resist process: it is difficult to perform a successful lift-off with small patterns which are closely spaced, which is a problem that is not encountered when negative resist is used. Thus the change from using negative to positive resist, although enhancing the minimum achievable linewidths, greatly increased the number of sample failures during the fabrication process.

3.4.2 Sample layout and design

The layout of patterns on the sample surface was deliberately changed for use with the Jeol. Figure 3.12 shows a diagram of the new pattern layout, and figure 3.13 is a micrograph of an actual sample.

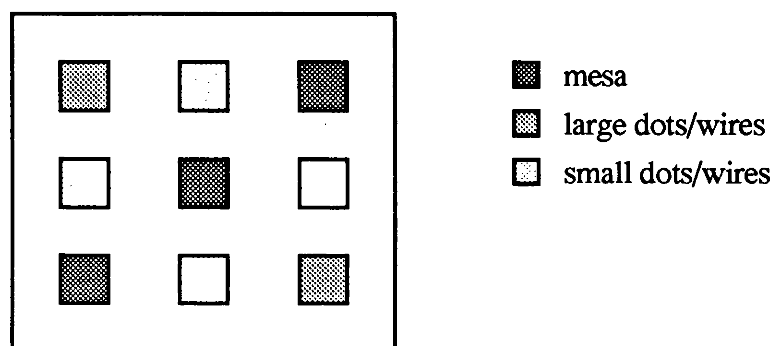

Figure 3.12 Sample layout for use with Jeol

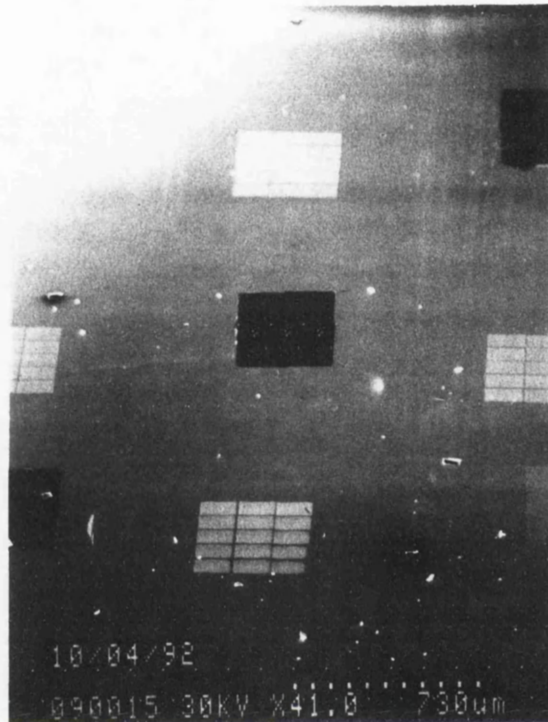

Figure 3.13 Micrograph of sample layout

The change of layout was needed because:

(i) the size of the individual dot arrays increased from 200μm square to 400μm square, which meant that fewer arrays could be patterned vertically.

(ii) the previous layout was inefficient because it used too many mesas. The new layout had the advantage that every pattern of small dots had two adjacent mesas.

The sample was patterned in two layers. Firstly, the small dots were patterned using a high magnification and small spot size. Secondly, the mesas and large dots were patterned with a larger spot size and lower magnification. A glance at figure 3.12 shows that the layout is symmetrical (ignoring the large dot patterns which merely act as areas for comparing the luminescence intensity between the mesas and small dot patterns) allowing the sample to be removed between layers and rotated through 90° or 180° without the risk of the patterns interfering with each other. Samples were sometimes removed from the Jeol and rotated which usually helped focusing. This was probably because of a fault with one of the registers used by the Jeol for calculating the focus error, which was only recently discovered.

3.4.3 High resolution lithography using the Jeol

The smallest wires produced on InGaAs quantum well material had a lateral width of approximately 20nm ± 5nm, although wires were patterned on GaAs substrates which had lateral dimensions of 15nm ± 5nm. When wires as small as this are patterned then the edges of the wire become very uneven because of the comparatively large variations in wire width along the length of the wire (the absolute variations in wire width may be only a few nm but this is large compared with the overall wire width).

Some examples of the small wires and dots produced by the Jeol are shown in figures 3.14 to 3.16. All of these structures were patterned using a magnification of 2400 and the 8192 by 8192 pixel format, which meant that each pixel was ~9nm by 7nm. Table 3.5 shows some of the conditions used for patterning wires and dots on the Jeol. The column headed "No. of pixels" refers to the number of pixels exposed in the structure (whether wire or dot), the number of scanbits refers to whether 4096 pixels (12 represents 2^{12}) or 8192 pixels (13 represents 2^{13}) were used for each frame and the beam current refers to the typical beam current available at the particular aperture/spot size combination used.

Magnification	Dot size (nm)	Wire size (nm)	No. of pixels	No. of scanbits	Exposure μCcm^{-2}	Beam current (pA)
2400		25	1 x 4400	13	2000	30
2400		50	2 x 4400	13	2000	30
600	60		1 x 1	12	1200	80
600	100		1 x 1	12	2500	80

Table 3.5 Details of Jeol parameters for fine line lithography

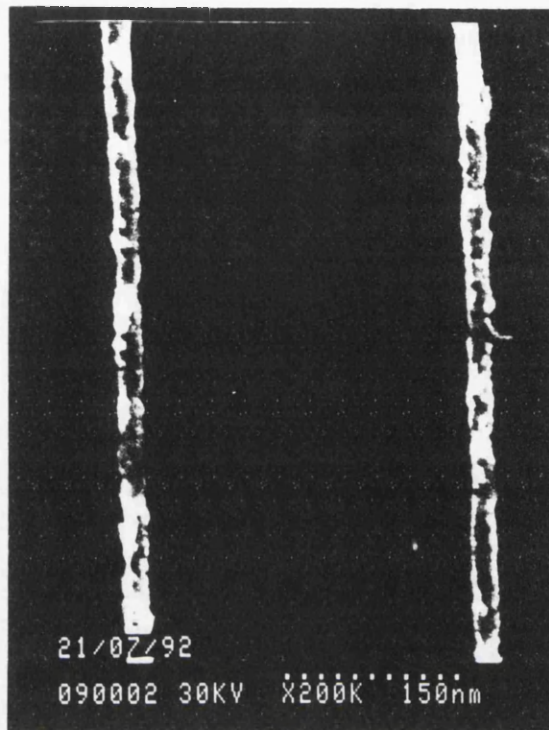

Figure 3.14 20nm wide wire array

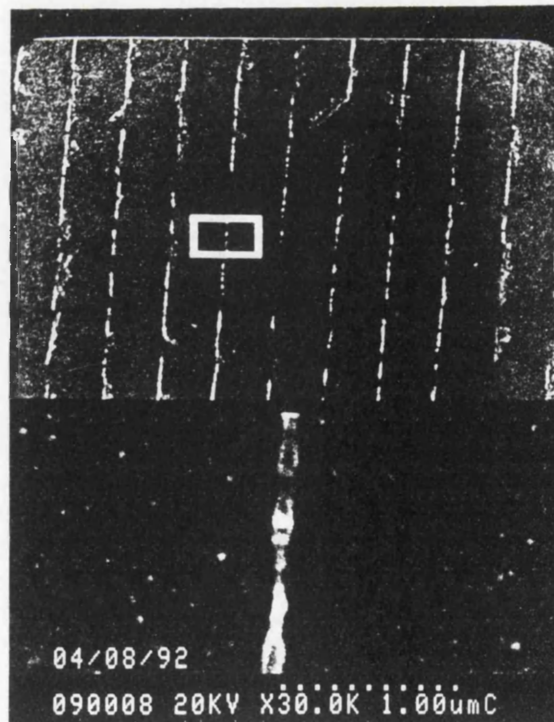

Figure 3.15 10nm wide wire array

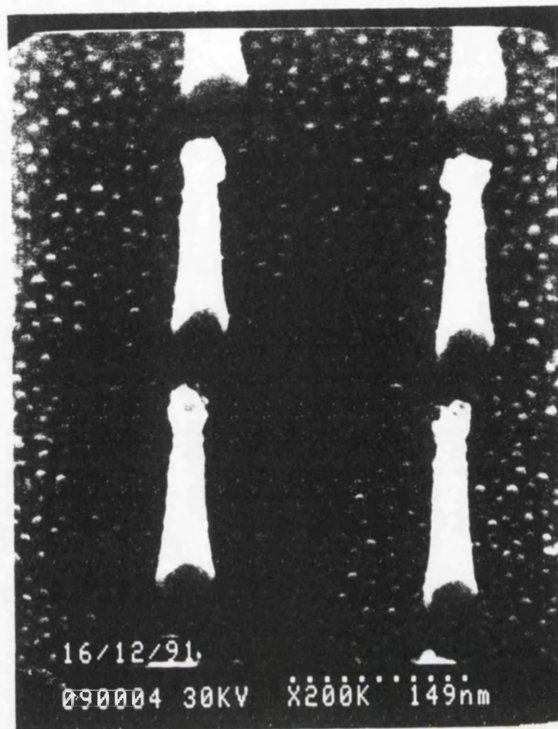

Figure 3.16 30nm dot array

3.5 The Electron Beam Pattern Generator (EBPG) HR5

The third, and final, electron beam lithography machine used during the course of this research was a Leica-Cambridge EBPG HR5, which will be referred to as the Beamwriter. Unlike the PSEM 500 (a modified SEM) and the Jeol 100CXII (a modified TEM) the Beamwriter is a purpose built lithography machine which is fully computer controlled with automatic focusing. The Beamwriter has an accelerating voltage of 50kV and a minimum spot size of 12nm. The stitching accuracy is 40nm and it has a beam step size which is continuously variable from 5nm to 312.5nm. A diagram of the Beamwriter column is shown in figure 3.17. Although the Beamwriter does not have resolution quite as good as the Jeol it does have one distinct advantage. The Beamwriter is capable of producing large arrays of wires and dots (e.g. 2mm square) of uniform dimensions with accurate stitching of the individual frames which make up the array. One of the major faults of the Jeol - perhaps the only major fault of the Jeol - is that it has a tiny depth of focus. The effect of this is to make it very difficult to pattern large areas with wires or dots, perhaps because of a drift in the focus with time (a typical 200μm square array of 25nm wires could take 2 hours to write) or a focus shift due to a slight tilt in the sample.

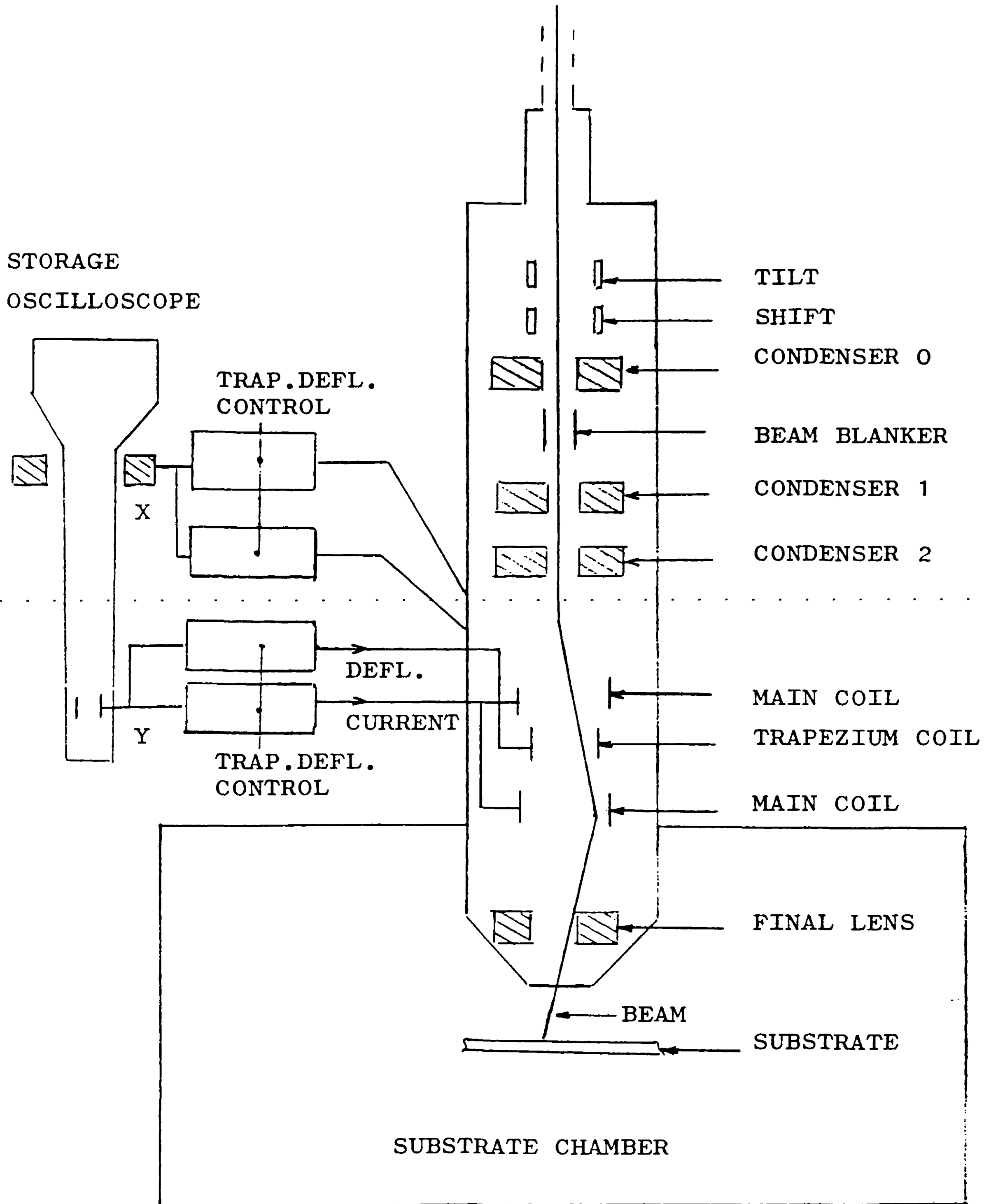

Figure 3.17 Diagram of Beamwriter (EBPG HR5) column

Due to the strength of the luminescence signal PL measurements do not require large arrays (e.g. 1mm^2) of wires and dots. However, for experiments which have notoriously weak signals, such as PLE with a white light source, large arrays of wires or dots are indispensable. It is in producing samples with large patterned areas that the Beamwriter excels.

3.5.1 Fabrication process for the Beamwriter

The fabrication process for the Beamwriter was very similar to that used for the Jeol. No alignment marks were required. The same bilayer resist structure was used for the Beamwriter as was used with the Jeol, 2.5% BDH and 2.5% Elvacite, and then a layer of SrF_2/AlF_3 approximately 25nm thick was evaporated and lifted-off.

3.5.2 Sample layout and design

The method of clamping samples in the Beamwriter obscures approximately 2mm of the sample and as a result, to reduce wastage, the minimum useful size of sample which could be patterned was approximately 10 by 5mm. Yet again this called for a new sample layout, which is shown in figure 3.18.

Each array is 500μm by 500μm and is separated from its nearest neighbour by 1mm. The layout of the sample is such that the sample is symmetric about its length.

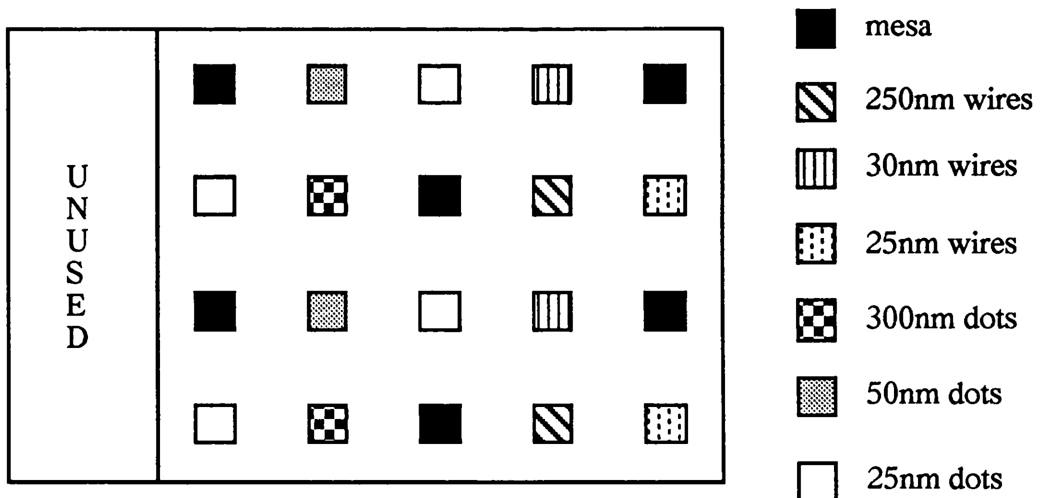

Figure 3.18 Sample layout for use with the Beamwriter

3.5.3 High resolution Lithography using the Beamwriter

Examples of some of the very small wire and dot structures which were patterned with the Beamwriter are shown in figures 3.19 to 3.21. Table 3.6 gives details of the exposure, spot size and resolution values which were used to fabricate these wire and dot structures.

Dot diameter (nm)	Wire width (nm)	Exposure dose μCcm^{-2}	Resolution	Spot size (nm)
15		36	0.14	12
25		1960	0.015	20
300		1000	0.025	112
	25	700	0.01	12
	50	644	0.01	20
	300	330	0.025	80
MESA		300	0.14	400

Table 3.6 Details of the parameters used for Beamwriter lithography

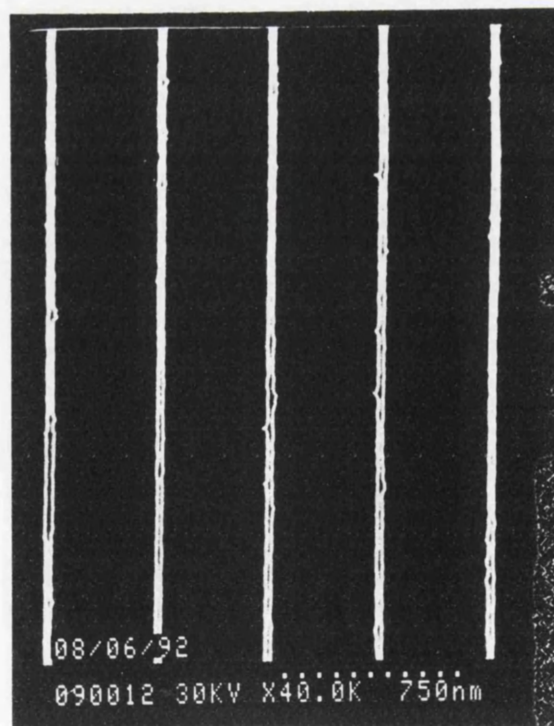

Figure 3.19 30nm wide wire array

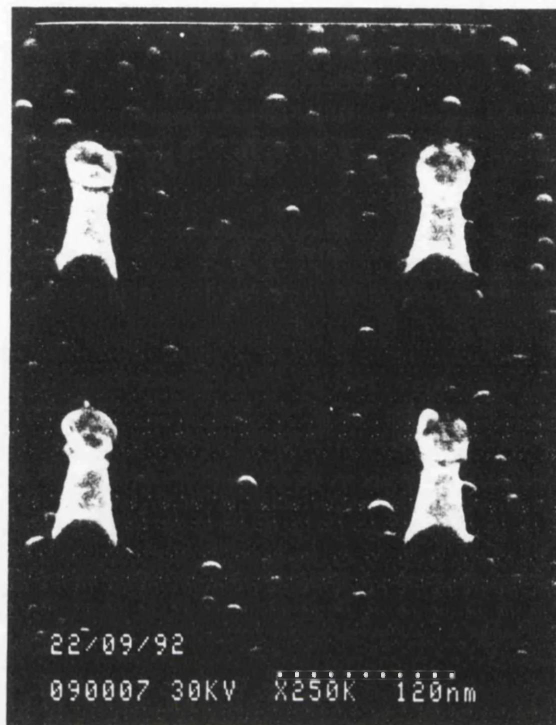

Figure 3.20 Array of 25nm diameter dots

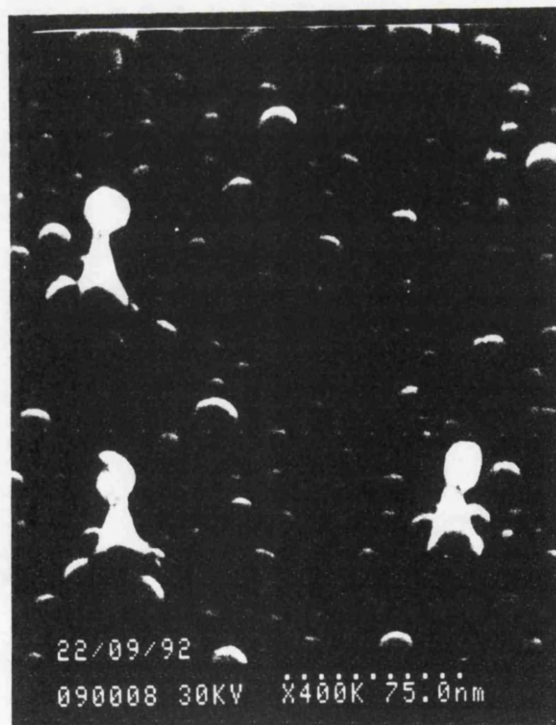

Figure 3.21 Array of 10nm diameter dots

References

Adachi S, Noguchi Y and Kawaguchi H, 1982 J Electrochem Soc Vol 129 No 5 p1053-1062

Arnot H E G, 1990 PhD Thesis, Glasgow

Beaumont S P, 1991 In "Low dimensional structures in semiconductors" Eds Peaker and Grimeiss. NATO ASI series B Physics Vol 281 Plenum press

Deckman H W and Dunsmuir, 1983 J Vac Sci Technol B1 (4) p1166-1170

Greeneich J S, 1975 J Electrochemical Society Vol 122 p970-976

Harris R A, 1974 J Electrochemical Society Vol 120 p270-274

Komuro M, Atoda N and Kawakatsu, 1979 J Electrochem Soc vol 126 p483

Mackie W S, 1984 PhD Thesis, Glasgow

Roberts E D, 1976 Vacuum vol 26 No. 10/11 p459-467

Spears D I and H I Smith, 1972 Electronics Letters Vol 8 p102

Sze S M, 1988 "VLSI Technology" 2nd Edition McGraw-Hill

Thoms S, MacIntyre I, Beaumont S P, Al-Mudares M, Cheung R and C D W Wilkinson, 1988 J Vac Sci Technol B6 (1) p127

Watt I 1985 "Principles and practice of electron microscopy" (Cambridge University Press)

Wilkinson C D W and S P Beaumont, 1986 Proc. Winter School, Les Houches, France, March, Eds M J Kelly and C Weisbuch. Springer proc in Physics 13 p36-50.

Chapter 4
Pattern transfer and reactive ion etching

4.1 The Need for dry etching

Wet chemical etching is a simple, useful, low damage technique for transferring a large (several microns) pattern from a mask to the underlying substrate. The problem with wet etching lies in the isotropic nature of the etch profile, which renders it unsuitable for patterning small (a few hundred nanometres) feature sizes, and completely useless for producing narrow cylinders which are etched to a depth very much greater than the mask thickness.

Although wet etches have been used (most notably by Notomi et al, 1991) to produce very narrow wires, the wires were carefully aligned along etch planes and the etch chosen was selective, in that it was specific to one particular etch plane. It is a process which requires painstaking preparation to ensure alignment of the wires and a tightly controlled etch time. This crystallographic etching process lends itself to making wires but is not so well suited to fabricating dots.

In view of the unsuitability of wet etching for creating structures of small dimensions on randomly oriented substrates, an alternative process is required which is anisotropic in nature; the only suitable candidate is the dry etching process. One of these processes is reactive ion etching.

4.2 Reactive ion etching - general introduction

A typical reactive ion etching machine has a vacuum chamber containing two parallel electrodes, one of which is grounded and the other is connected through a blocking capacitor to a radio-frequency generator (van Roosmalen et al, 1985). RIE is a term given to the process of etching a substrate in a neutral, partially ionised gas which contains mainly neutral radicals,

free electrons and ions - most of which are positive: this neutral, partially ionised gas is called a glow discharge.

Unlike wet etching, where the substrate is immersed in the etching reagent, RIE proceeds with the substrate being subjected to ions, atoms, molecules and radicals (a radical is a fragment of a molecule with an odd number of unshared electrons {Lehmann, 1985}). The areas exposed to the plasma are removed by either physical bombardment (sputtering) of the substrate, or a chemical process whereby a volatile etch product is formed; or perhaps a combination of these two processes, with ion bombardment aiding chemical etching by locally heating the substrate and loosening the chemical bonds. Figure 4.1 shows a diagram of two of these processes, sputtering and chemical etching (after Ruska, 1987).

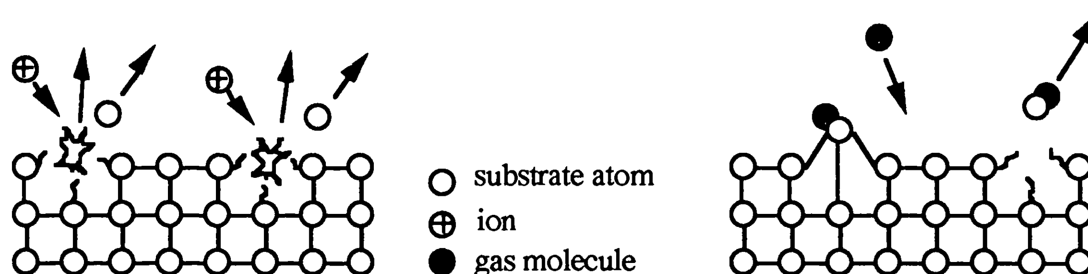

Figure 4.1 Sputtering of substrate with ions, and chemical etching with gas molecules

The basic processes involved in RIE are: generation of reactive species, transport of the reactive species to the substrate surface, absorption onto the surface, reaction with the substrate forming a volatile product, transport of the product species away from the substrate, and removal of the species from the chamber via the pumping process (Carter et al, 1989).

4.3 Basic theory of RF discharges

The etching mechanism of an rf discharge process relies on having highly reactive species which will react with the substrate to form a volatile product.

4.3.1 Generation of active species

These species are created by a radio-frequency discharge, which generates chemically reactive species from molecular gases which are sometimes relatively inert proir to dissociation (Coburn & Winters, 1979).

The rf electric field causes acceleration of the electrons in the plasma and the resulting high energy collisions precipitate changes in the gas molecules. Some examples of these processes are shown in equations 4.1 to 4.3:

Ionisation $Ar \xrightarrow{e^-} Ar^+ + 2e^-$ 4.1

Electron impact ionisation $H_2 \xrightarrow{e^-} 2H + e^-$ 4.2

Excitation $Ar \xrightarrow{e^-} Ar^* + e^-$ 4.3

These species - ions and atomic hydrogen (for example) - are highly reactive, and will either react with the substrate or recombine. To minimise this recombination process the etch gas is kept at low pressures in a vacuum chamber, thus increasing the average distance between collisions (low pressures also ensure that there is a high dc bias). The applied rf electric field offsets the continual relaxation and recombination by imparting energy to the electrons which enables them to ionise, dissociate and excite the gas molecules (Chapman, 1980).

Due to the presence of some high energy electrons in the plasma (most of the ions in the plasma have low energy but the ions traversing the dark space have high energies), which are considerably higher than a chemical bond energy (Ruska, 1987), the etch gases are broken down into every conceivable fragment, e.g.

CH_4 , CH_3 , CH_2 , CH , C , H and other combinations including the ionised versions of all of these.

4.3.2 Anisotropic etching

In an rf discharge process the plasma contains charged particles - ions and electrons - which are mobile; therefore, the plasma is a good electrical conductor and so it is at a uniform potential throughout. However, the plasma cannot exist in contact with an object and so it is separated from both the walls of the chamber and the substrate to be etched by an area with few electrons. This region is comparatively dark due to the lack of excited molecules and atoms relaxing and emitting photons, whereas within the plasma the constant relaxation of excited atoms ensures a bright glow. These dark spaces (or ion sheaths) act as small capacitors.

The positive ions and electrons can escape from the plasma to the sidewalls; electrons (being lighter) escape more readily than the ions, but this is soon balanced out because the plasma gradually becomes positively charged due to the preferential loss of electrons, and so electrons are then retained by the attraction of the overall positive charge of the plasma.

With the application of an external alternating electric field it would seem reasonable to assume that the substrate would only experience ion bombardment for half of the voltage waveform cycle, but this is not the case. The reason lies in the fact that the electrons are far more mobile than the ions. The effect of this is to offset the substrate voltage waveform, and to displace it to a negative value known as the dc self bias, as shown in figure 4.2 (Chapman, 1980).

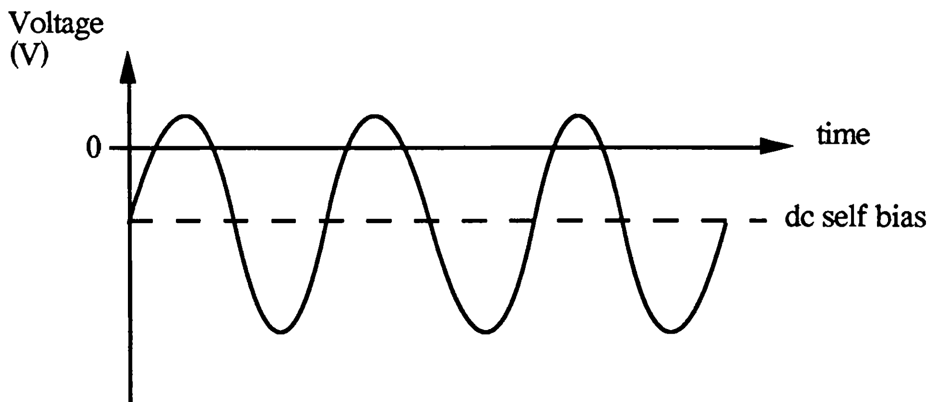

Figure 4.2 Effect of rf signal on substrate

As can be seen from figure 4.2, the substrate voltage is negative for almost all of the cycle, and so the substrate is bombarded with ions almost continually. Positive ions are accelerated away from the glow and across the sheath, giving a salvo of ions on the horizontal surfaces, whereas the vertical surfaces are subjected to a greatly diminished flux of ions, which arise from reflection of particles from nearby horizontal surfaces. It is this almost continuous bombardment of the sample with ions normal to the surface which aids and encourages vertical (anisotropic) etching, without promoting sidewall etching.

4.4 Etching with a methane/hydrogen gas mixture

During the last few years many different etch gases have been used to etch InP and its related compounds (InGaAs and InGaAsP). These include gases as diverse as: $CCl_2F_2/Ar/O_2$ (Hu and Howard, 1980), Cl_2/O_2 (Coldren and Rentschler, 1981), $SiCl_4$ with and without Ar (Stern and Liao, 1983), CH_3I/O_2 (Doughty et al, 1986), Ar with and without O_2 (Germann et al, 1989), CH_4/He, CH_4/Ar (Andideh et al, 1989), and CH_4/H_2 with Ar (Henry et al, 1987) or O_2 (McNabb et al, 1991).

During this research the etch gases used to etch InP nanostructures were methane (CH_4) and hydrogen (H_2). The main advantage of this etch mixture over the chlorine containing gas mixtures was that the etch did not need to be performed at high temperatures, which would not have been acceptable for etching samples with a negative resist mask because this would have caused the resist to flow and hence change the shape of the mask. RIE of InP in chlorine containing etch gases needs to be performed at high temperatures because of the low volatility of $InCl_x$ compounds (McNevin et al, 1986).

Andideh et al (1989) compared the results of etches which used CH_4/H_2, CH_4/He and CH_4/Ar gases. They found that all three etches had similar etch rates and characteristics. CH_4/H_2 had a higher etch rate than CH_4/He although helium being heavier should be a better sputtering species, from this they deduced that the etching role of hydrogen was more

chemical than physical in nature. CH_4/Ar had the highest etch rate of all due to the physical nature of argon etching as a sputtering species. The most anisotropic profiles they obtained used hydrogen to dilute the methane.

Although much of the methane/hydrogen etching process remains recondite, several theories for the etching mechanism have been proposed and substantiated by some experimental evidence.

The etch process is generally thought to be the reverse of the MOVPE growth process. It has been shown that phosphine (PH_3) is the primary phosphorous-containing volatile product (Hayes et al, 1989) and it is postulated (although not proved) that trimethyl indium is the primary indium containing volatile product. It is not easy to verify this because the methyl radical species (CH_3) is so reactive that it is difficult to detect by mass spectrometry, which tends to detect the products of reactions rather than the reactants themselves. Equations 4.4 and 4.5 show possible dissociation processes involving the etch gases and equation 4.6 shows how these gases are thought to react with the InP.

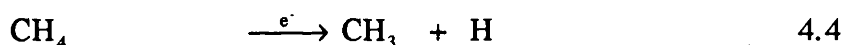

$$CH_4 \xrightarrow{e^-} CH_3 + H \qquad 4.4$$

$$H_2 \xrightarrow{e^-} 2H \qquad 4.5$$

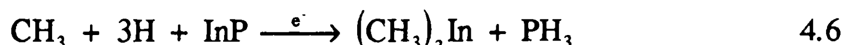

$$CH_3 + 3H + InP \xrightarrow{e^-} (CH_3)_3In + PH_3 \qquad 4.6$$

It is observed that after CH_4/H_2 etching there is a polymer coating on the etch mask. This polymer is thought to be an organic substance originating from the methane because the polymer thickness increases with methane content. It is postulated that the methyl groups interact with each other because they cannot react with the substrate.

There appears to be two competing reactions in equation 4.6. The methane seems to be responsible for removing the indium, and the hydrogen atoms - from both the hydrogen and methane gases - for removing the phosphorous. It has been observed that as the amount of hydrogen in the gas mixture increases the sample surface becomes more and more depleted of phosphorous. This is evidenced by small (30nm) rounded features on the sample surface which have been attributed to both ion induced topography (Hayes et al, 1989) and islands of metallic indium (Pajot et al, 1989). As the amount of methane in the gas mixture increases so the etch rate increases and the polymer deposition increases until a certain point is reached, beyond which the etch rate decreases. Thus the etch gas mixture is critical in order to obtain a good etch.

4.5 Surface damage due to RIE

In order to create structures in a substrate material it is necessary to remove the unwanted material - the etching process. With the removal of this material it is inevitable - with wet or dry etching - that damage is inflicted on the substrate; but what is most important is the level and type of damage inflicted.

There are three types of defect which commonly occur in dry etching: deposition of a substance onto the mask and/or substrate, diffusion of some of the plasma species or products into the substrate, and dislocation of the crystal lattice (Doughty et al, 1986).

Quantitatively assessing the extent of the damage inflicted is a difficult process, many of the techniques which are used give results which are more qualitative than quantitative in nature. A further complication arises from the possibility that the sidewall damage is different to the surface damage. It is simpler to assess the surface damage, but it is more important in fabricating quantum dots and wires to know the sidewall damage as this affects the luminescence intensity.

Needless to say, the best dry etching process is the one which produces least damage yet still manages to etch the material anisotropically.

4.6 The ET340 reactive ion etch machine

The first dry etch machine used during the course of this research was an Electrotech SRS Plasmafab 340 RIE machine, which, at that time, was the only one available in the department for CH_4/H_2 etching. It is a reactor which has a 3.3 to 1 ratio of anode area to cathode area, and both electrodes are made of aluminium. The sample to be etched is placed on a titanium oxide coated cathode which has a diameter of 17cm. The cathode (driven electrode) temperature was regulated by circulating cooling fluid which was maintained at a constant temperature of 30°C during etching. A diagram of the ET340 is shown in figure 4.3.

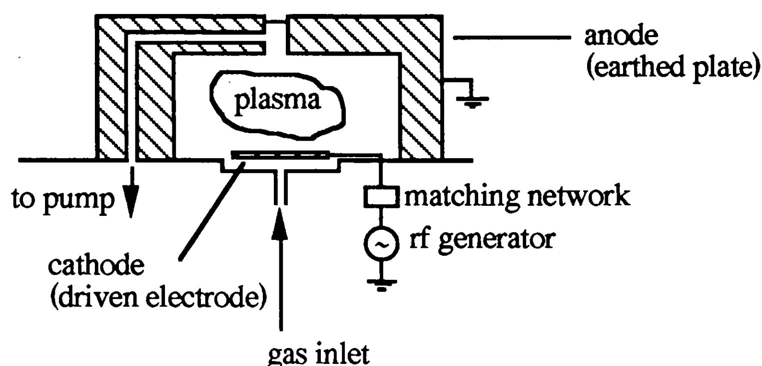

Figure 4.3 Diagram of the ET340 etch chamber

The ET340 permits control of the gas flow rates and forward power but the pressure cannot be controlled independently of the flow rates (the machine has been modified since this work so that the pressure can now be controlled independently), it can only be adjusted by varying the flow rate of the etch gases. As a result of the chamber geometry, the dc self bias was usually in the range from -600 to -1100V. This is quite high compared with other machines which would only generate a dc self bias in the range from -200 to -400V. This high dc self bias arouses suspicion that the etching process will inflict serious damage due to the large potential accelerating the active species in the plasma, and the corresponding high momentum of species as they impinge on the sample substrate, perhaps causing crystal dislocation.

Much work has been published on CH_4/H_2 etching since it was first reported as suitable for etching InP by Niggebrugge et al, 1985. However, there are many different reactive ion etch machines used in research establishments, and as the etching conditions (gas flow rates, chamber pressure, etc.) generally differ for different chamber geometries there is no standard optimum recipe for all machines, but each brand of machine will have its own optimum etch conditions. These conditions can vary considerably between machines.

It is also likely that the etching conditions could be different depending on what features of the etched structures are the most desirable: whether it is more important to obtain vertical sidewalls or smooth surfaces. The etch conditions could also be different depending on whether large structures (several microns) such as waveguides, or small structures (100 nm) such as quantum wires are to be etched.

For these reasons it was decided to do a wide range of tests in order to optimise the etching conditions for the ET340 and especially for the particular feature sizes - quantum wires and dots - which were of interest during this research.

4.6.1 Optimising the ET340 CH_4/H_2 process

With dry etching it is difficult to predict accurately what changes will occur in the etch if one parameter is changed, the best way to find out is to use an empirical approach and perform the particular etch. However, matters are complicated by the large number of parameters which can be altered. Those parameters which can affect the etch include: methane flow rate, hydrogen flow rate, etch pressure, forward power, methane to hydrogen ratio and electrode temperature. It is also not certain whether it is the methane to hydrogen ratio or the absolute methane flow rate which determines whether or not the etch mixture is methane rich.

Previously, InP had been etched in the ET340 machine within the department (Arnot, 1990), but that etch process used forward powers of approximately 180W which gave rise to a dc self bias of approximately -1100V. This value of dc bias was considered to be likely to produce some form of damage on the sample surface (as a comparison the work done on

etching GaAs to fabricate dots uses a dc bias of approximately -300V) due to the high energy of the ions traversing the dark space and impinging on the sample.

In attempting to optimise the etch process this forward power of 180W was used initially but the power was gradually reduced to the minimum possible value which would support anisotropic etching.

The results obtained are summarised in Table 4.1. Each etch was performed for 3 minutes to ensure that the results could be compared directly, and the chamber was conditioned prior to etching by doing a short (1 minute) etch, as suggested in the literature (Hayes et al, 1989). Negative resist (8% HRN) was used as the etch mask. The dot profiles always exhibited an overcut profile (the thickness at the top of the structure was always less than the thickness at the bottom of the structure). The overcut is thought to be due to build-up of organic polymer on the mask surface: as the polymer builds-up less of the substrate area is exposed to the etch and so the etched feature inevitably broadens, thus exhibiting an overcut profile. This is shown schematically in figure 4.4.

CH_4:H_2 Ratio	CH_4 Flowrate (sccm)	Pressure (mTorr)	Power (W)	Indium droplet size (nm)	Overcut (estimate)	Etch rate (nm/min)
3:2	7.5	7.3	180	30	big	120
3:2	6	5.5	180	40	small	130
1:7	6	20.5	180	80	small	120
3:2	7.5	6.6	150	50	medium	104
1:5	7	18	120	75	medium	104
1:3	8	15	110	40	big	120
1:1	8	9.2	110	30	medium	120
4:3	8	8.9	110	40	medium	140
2:1	8	8.6	110	40	big	140
3:2	12	8.9	110	45	medium	93
5:4	10	10.4	100	25	small	89
9:8	9	8	100	35	medium	82

Table 4.1 Summary of important etch results

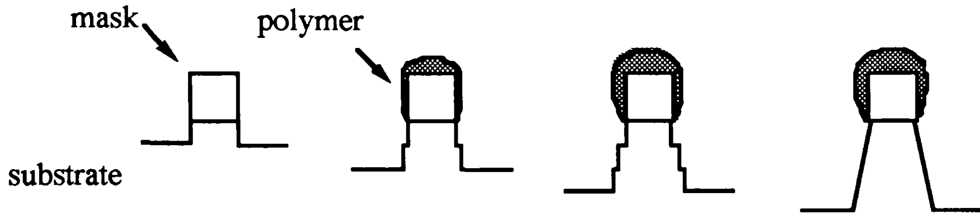

Figure 4.4 Changes in etch profile with time, showing origin of overcut profile

The column which is headed "overcut" is intended to serve only as a qualitative indication of how steep this angle of overcut is. The reason that more accurate results are not given is that the overcut is not always reproducible as it depends on the polymer deposition, and it is difficult to measure the overcut with any degree of certainty as the polymer build-up on the mask is not uniform and the dots were only etched to comparatively shallow depths (300nm).

On examining the etch rates shown in table 4.1, it is clear that the highest etch rates are achieved by a judicial choice of gas ratios and flow rates, and they do not correspond solely to the etches with highest values of forward power.

The etch conditions which were chosen as giving the optimum etch are recorded in the penultimate row of table 4.1. This etch uses a CH_4 to H_2 ratio of 5:4 with a CH_4 flowrate of 10sccm. Several other etches were performed to ascertain the etch rate more accurately. The mask used for these etches was titanium, and the etch depths were measured using a Tally-Step surface profiler. The results are plotted in figure 4.5.

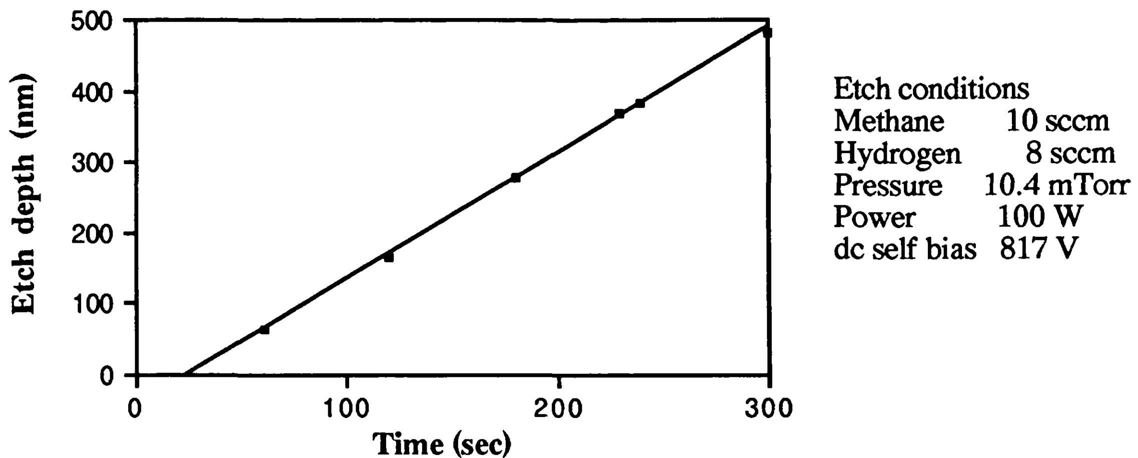

Figure 4.5 Etch depth versus time for optimum CH_4 / H_2 etch conditions

The etch rate determined from the slope of the best-fit line in figure 4.5 is 105 nm/min. At first it might seem surprising that this line does not go through the origin. However, one explanation for this is that there is an induction time when the plasma stabilises during which no etching takes place. Another possible explanation for the delay in the etch process starting

is that there could be some native oxide on the sample surfaces and so this oxide would have to be removed before etching could proceed. From the graph this induction time corresponds to 23 seconds.

An etch was also performed under identical conditions, except with the forward power increased to 150W, giving a dc bias of 973V. The measured etch rate was 160 nm/min.

The criteria used for selecting the optimum etch for fabricating dots and wires were the following: as smooth a surface, as small indium droplets, and as low a dc bias as possible. However, for certain experiments (notably those on surface phonons) the important feature of the etched structure needs to be vertical sidewalls. These are most readily obtained when the mixture has little methane and so the optimum etch for these experiments could be different.

Figure 4.6 shows two micrographs with near horizontal views of two different dot sizes etched in conditions which were considered to be the optimum for fabricating dots. Figures 4.7 and 4.8 show the micrographs, taken at an angle of 40° from the vertical, of some of the other etch results obtained. These results are all documented in table 4.1.

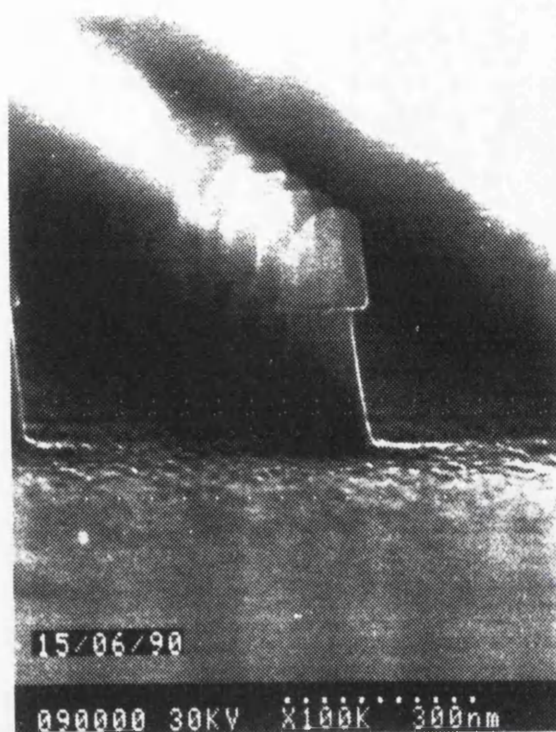

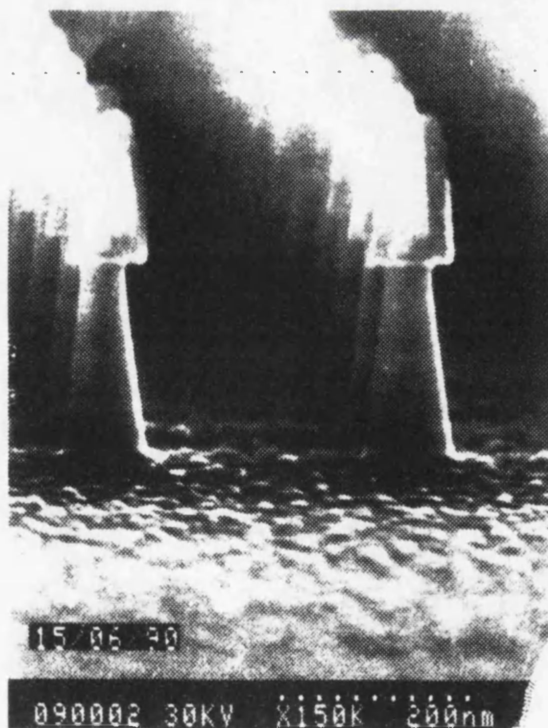

Figure 4.6 Two micrographs showing 100nm (upper micrograph) and 60nm (lower micrograph) wide pillars of InP, etched under optimum conditions

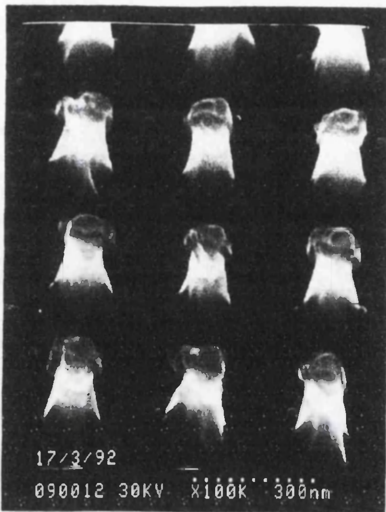

CH_4/H_2 ratio 3:2
Etch pressure 7.3mTorr
Power 180W
dc self bias 1070V

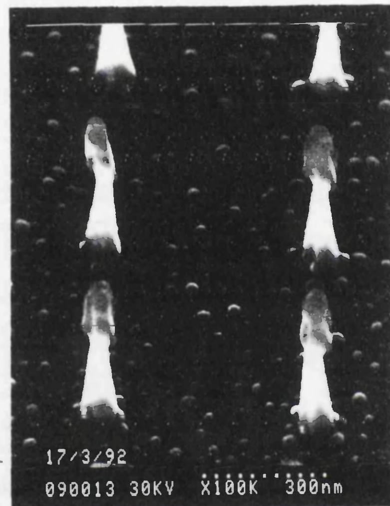

CH_4/H_2 ratio 3:2
Etch pressure 5.5mTorr
Power 180W
dc self bias 1115V

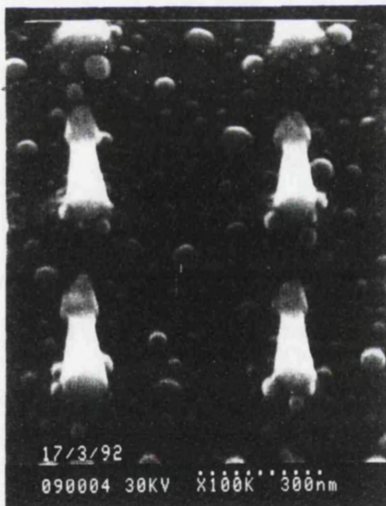

CH_4/H_2 ratio 1:5
Etch pressure 18mTorr
Power 120W
dc self bias 805V

Figure 4.7 Micrographs of dots etched in various etch conditions, as shown in table 4.1

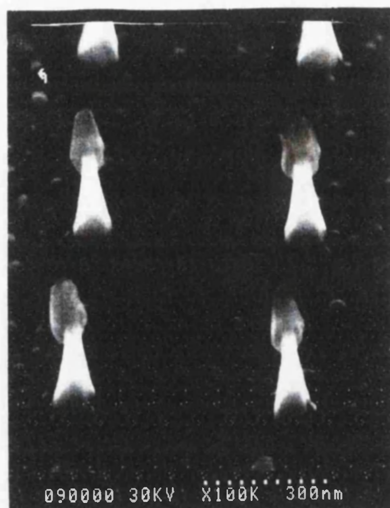

CH_4/H_2 ratio 1:3
Etch pressure 15mTorr
Power 110W
dc self bias - 805V

CH_4/H_2 ratio 3:2
Etch pressure 8.9mTorr
Power 110W
dc self bias 877V

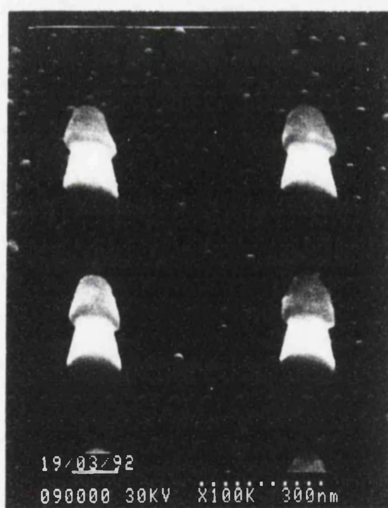

CH_4/H_2 ratio 9:8
Etch pressure 8mTorr
Power 100W
dc self bias 835V

Figure 4.8 Micrographs of dots etched in various etch conditions, as shown in table 4.1

4.6.2 Damage inflicted by ET340 during CH_4/H_2 etching

The aim of this research is to examine the effects of fabricating submicron structures such as wires and dots. Optimising the etch process is not an end in itself but a means to an end; the end being the fabrication of quantum dots - pillars which exhibit effects caused by quantum confinement of the carriers.

Optimising the etching conditions to produce smooth surfaces is aesthetically pleasing but it does not necessarily mean that the etched structure has only suffered a low level of damage; whether or not this is true must be assessed by other means.

The amount of damage that the etched material has sustained is very important. If a high degree of damage has been inflicted then there could be a large number of non-radiative centres, the result of which would be to reduce drastically the luminescence intensity. Such an outcome would be catastrophic.

The reason for this is that after etching the surface into free-standing pillars only a small fraction of the quantum well material remains. This small volume of active material must produce a large enough signal to allow detection with the germanium detector. With the decrease in dot size there comes a corresponding decrease in the luminescence signal because of the increase in the surface area to volume ratio. This research being chiefly concerned with fabricating structures which are as small as possible, it is vital to maintain as strong a luminescence signal as possible in order to be able to detect any signal, and thereby furnish experimental data on quantum confinement effects. This problem of a weak luminescence signal is exacerbated by the fact that there is a fundamental limit on how close the dots or wires can be spaced - this limit is imposed by resist and lift-off considerations - and so the pattern cannot simply be made more dense to counteract the decreasing luminescence signal. This shows the importance of the etch process being one which inflicts minimal damage to the sample surface, and the catastrophic effects of an etch process which inflicts a large degree of damage.

As previously mentioned, it is not a trivial task to assess the extent of the damage which is inflicted on the sample surface and especially on the sidewalls during etching.

In order to assess the damage both photoluminescence spectroscopy and phonon Raman scattering were performed. Whilst photoluminescence has been used previously to assess etching damage, it is difficult to interpret the data obtained and derive any meaningful conclusions from the luminescence data alone. However, when used in conjunction with Raman scattering it can provide useful information. Raman scattering is used because it is sensitive to any disorder of the crystal lattice, showing up any slight lattice disorders with a broadening of the LO (longitudinal optic) phonon peak. It might also show a peak associated with the TO (transverse optic) phonon after etching, which is normally symmetry forbidden for (100) surfaces in cubic crystals (Watt et al, 1988).

4.7 The μP80 reactive ion etch machine

During the course of this research another RIE machine suitable for CH_4/H_2 etching was purchased. It was a Plasmafab Microprocessor RIE 80, which is a parallel plate reactor with a 2.8:1 ratio of anode area to cathode area. The sample to be etched is placed on a graphite plate which completely covers the lower electrode (the cathode). Both the methane and hydrogen gases are introduced into the chamber via a shower head in the anode. During etching the cathode temperature was regulated by circulating cooling fluid at a constant 25°C because the electrode temperature rises during the etching process. A diagram of the μP80 etch chamber is shown in figure 4.9.

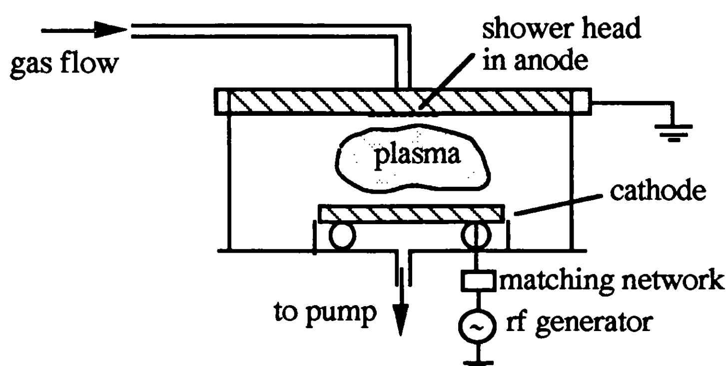

Figure 4.9 Diagram of the μP80 etch chamber

4.7.1 Advantages of the μP80 RIE machine

Since so much time and effort was devoted to optimising the etching conditions for the ET340 RIE machine, the question that naturally arises is, why change to a different RIE machine which uses exactly the same etch gases?

There were several reasons for pursuing etching using the μP80. The most notable among these was the lure of the low dc self bias. During etching the μP80 typically develops a dc bias of approximately -300V for a forward power of 100W, this is only a third of the typical value developed by the ET340. This low accelerating voltage tantalises with the prospect of a low level of sample surface damage; and with low damage comes the boon of a stronger luminescence signal - and hence of dots and wires which will emit light when fabricated to smaller lateral dimensions, thus increasing the possibility of achieving the goal of this research, namely, observing quantum confinement effects. So for this reason alone - the possibility of lower surface damage - etching on this machine had to be pursued.

There were also other advantages associated with the μP80. It allowed the user to control the chamber pressure independently of the gas flow rates - a facility not available on the

ET340. A further advantage was related to the fact that, as the name suggests, the μP80 was microprocessor controlled, and so it could accommodate a multi-step etch process. The usefulness of this function, although perhaps not immediately apparent, will become clear later, in the surface phonon section (section 4.7.3).

4.7.2 Optimising the μP80 CH_4/H_2 process

It was thought probable that the optimum etch conditions of the μP80 would differ from those of the ET340 because the chamber geometry of the μP80 is different to that of the ET340. In order to verify this and to obtain the optimum process conditions a series of experiments was embarked upon.

Rather than expending copious amounts of time and effort characterising the etching process on the μP80, as was done on the ET340, it was decided that only a few tests would be done and thereby an acceptable etch process would be developed. This procedure was adopted because there was a paucity of time available and, as stated previously, the etching process is only a means to obtaining quantised structures. If, however, after doing PL on structures etched using this process the signal was very low then it would still be possible to return to the etch process and adjust some of the parameters to obtain a more critically optimised etch process. If a strong PL signal was obtained then this would confirm that the etch process was suitable for the fabrication of small structures and so verify that it would be sufficient for the needs of this work.

As with etching using the ET340, when using the μP80 the forward power was kept constant at 100W. Although this decision was taken somewhat arbitrarily, it did serve to allow comparisons to be made between etches performed on the two machines.

Initially, only three etches were performed. The methane flow rate and etch pressure were held at a constant value and the hydrogen flow rate was varied. Adesida et al (1990) used exactly the same machine (μP80) and etch gases for RIE of InP and they quoted a methane to hydrogen flow rate of 1:3 as the optimum etch conditions. With this in mind it was decided to perform some tests with parameters which were similar to these conditions, hence methane to hydrogen flow rate ratios of 1:2, 1:3, and 1:4 were used. These parameter are shown in table 4.2, along with the etch rates and maximum surface indium droplet size. Micrographs of two of the etch processes are shown in figure 4.10.

As can be seen from table 4.2 and the micrographs shown in figure 4.10 the variation in hydrogen gas flow rate has little effect on the etch profile. However, with low hydrogen concentrations there is a more noticeable amount of polymer build-up. These results seem to be in agreement with those obtained by Thomas and Clements (1992), who suggest that the etch rate is chiefly determined by the partial pressure of methane, and not by the ratio of CH_4 to H_2.

CH_4 flowrate (sccm)	H_2 flowrate (sccm)	Pressure (mTorr)	Power (W)	Indium droplet size (nm)	etch rate (nm/min)
8	16	19.8	100	15	28
8	24	20.0	100	15	24
8	40	21.5	100	15	24

Table 4.2 μP80 etch results for constant rate of CH_4 flow

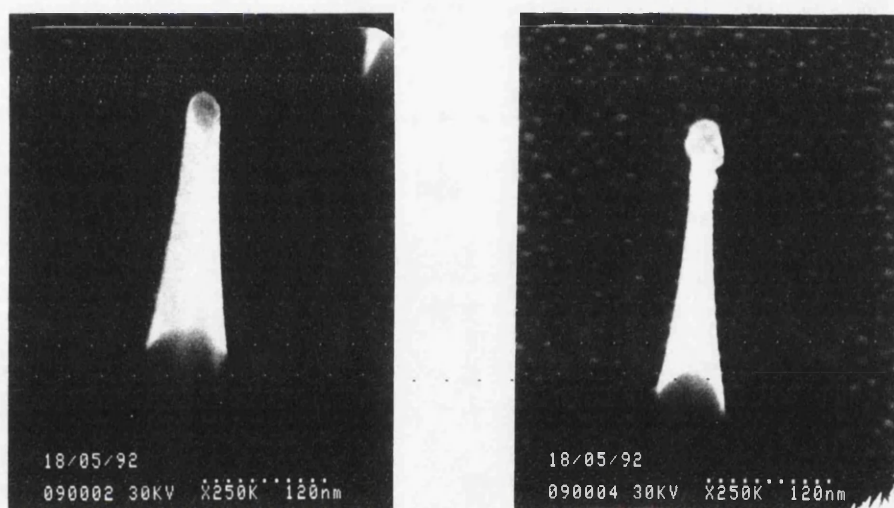

Figure 4.10 The micrograph on the left shows a 35nm dot etched in a CH_4/H_2 ratio of 1:3, and the micrograph on the right shows a 25nm dot etched in a CH_4/H_2 ratio of 1:2.

A few more etch tests were performed, this time the methane to hydrogen ratio was held at a constant value of 1:2.3 (there were some minor variations, but these were less than 10%), but the methane and hydrogen flow rates were both altered and the etches were performed at different chamber pressures. The results of these tests are given in Table 4.3.

CH_4 flowrate (sccm)	H_2 flowrate (sccm)	Etch pressure (mTorr)	Indium droplet size (nm)	Etch rate (nm/min)
4.2	11.0	8.5	40	23
14	32.1	19.5	15	28
24.3	53.0	30.0	15	31
34.2	73.9	39.3	15	33

Table 4.3 Etch results for µP80 with constant CH_4 to H_2 ratio

The graph of etch rate versus pressure for the data given in table 4.3 is shown in figure 4.11. The points are joined by a quadratic curve which serves as a guide for the eye.

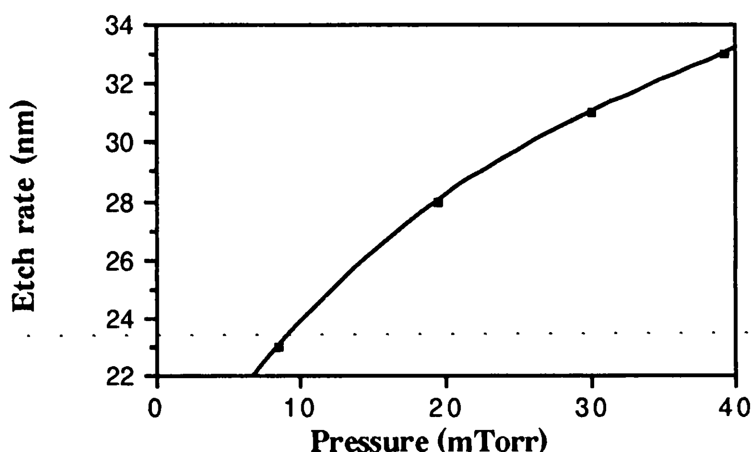

Figure 4.11 Etch rate versus pressure for etching InP in the µP80

From the graph it is clear that the etch rate increases with pressure quickly at low pressures but this increase reduces gradually. The sample etched with a methane flowrate of 4.2sccm had a very rough surface, however, the other three samples displayed similar characteristics - they had smooth surfaces with a regular layer of small indium droplets.

It is interesting that similar etch characteristics were returned by such diverse etching conditions: the pressures varied from 20 to 40mTorr and the CH_4 flowrates varied from 14 to 34sccm. The highest CH_4 flowrate probably produced the most polymer build-up but this is only an estimate from the micrograph. The only quantifiable difference between the etches was the different etch rates shown in table 4.3, which only change by 5nm/minute over the 20mTorr pressure change.

4.7.3 The multi-step etch process

Adesida et al (1990) obtained highly anisotropic etch profiles by regularly removing the polymer build-up on the inert mask surfaces using an oxygen etch. Thus the overall etch process consisted of CH_4/H_2 etching for a few minutes, followed by a brief oxygen clean, then another CH_4/H_2 etch and a further oxygen clean, etc. This process was continued until the required etch depth was reached. By using this process Adesida et al (1990) obtained structures which had an anisotropy ratio of 25:1 (i.e. for every nanometre etched horizontally 25nm were etched vertically) which they claim to be unprecedented in RIE.

Were it not for the polymer build-up CH_4/H_2 etching of InP would be an anisotropic process, but in order to obtain smooth surfaces high CH_4 percentages are required which tend to encourage polymer build-up. If the CH_4 percentage is drastically reduced then the concomitant polymer build-up is also reduced and anisotropy increases, but only at the expense of an intolerably rough sample surface.

From the evidence provided by these etches, it would seem that it is a fundamental impossibility to obtain etched samples which have smooth surfaces and highly vertical sidewalls, but this is where the elegance of the multi-step etching technique becomes apparent. It allows a high CH_4 content to be used in the gas mixture, which ensures that the surfaces are smooth, whilst combating the overcut profiles expected by removing the polymer which builds up (as shown in figure 4.4), thereby enhancing the anisotropy of the etch.

Although vertical sidewalls on dots and wires are pleasing to the eye they are not absolutely essential for this research work. The reason that truly vertical sidewalls are not necessary for this work is that the samples used generally contain only a single quantum well (typically 8nm thick) within 50nm of the sample surface. This means that even though the sidewalls are sloping, there is still only a slight increase in dot or wire width at this shallow depth compared with the mask size. This would not be the case if a sample with multiple quantum wells extending over a large depth was being used.

However, there is a realm in which the multi-step etch process stands aloft as being eminently suitable - it is within the sphere of surface phonon work.

The principal etch features required in producing a sample suitable for detecting surface phonons are: a large height to width ratio of the wires or dots and highly anisotropic sidewalls.

Two measures were taken in an effort to achieve such etch features: the standard CH_4/H_2 etch process was altered, with the CH_4 percentage being shifted to a lower value to minimise the polymer deposition; and a multi-step etch was used to remove any polymer deposit. The reason for using a lower CH_4 percentage may not be immediately obvious, but it is important. This is because the oxygen cleaning process does not remove all of the polymer; and so the lower the polymer build-up rate, the longer the allowable etch time between oxygen cleans.

Figures 4.12 and 4.13 show wires which were etched in different multi-step etch processes and have better etch anisotropy than the standard etch processes.

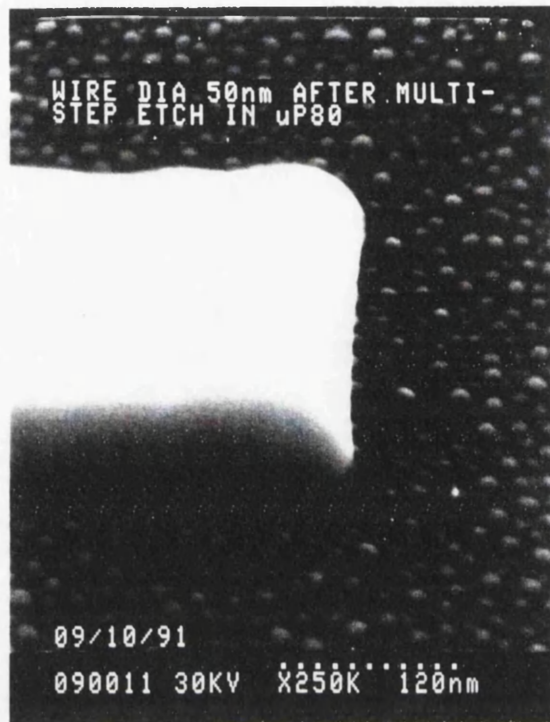

CH4 flow rate 7.8sccm
H2 flow rate 21.4sccm
Pressure 16mTorr
Power 100W
Mask 30nm titanium

Figure 4.12 A 50nm wide wire after a multi-step etch consisting of three 5 minute etches

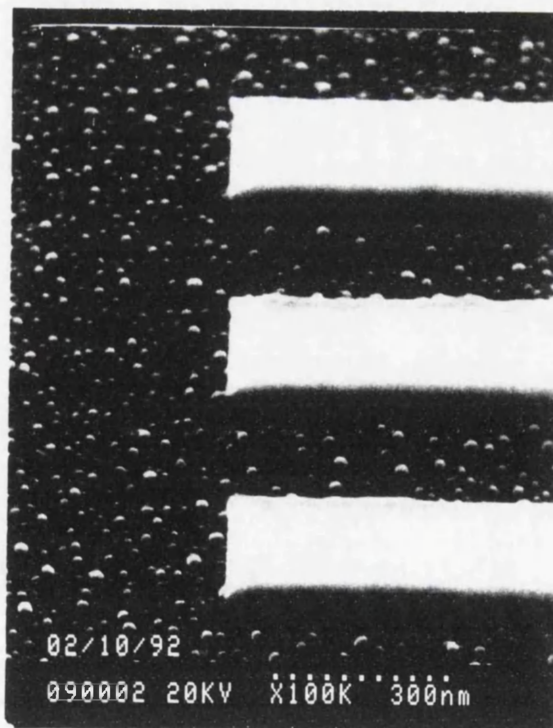

CH4 flow rate 7.8sccm
H2 flow rate 21.4sccm
Pressure 16mTorr
Power 100W
Mask 30nm titanium

Figure 4.13 50nm wide wire after a multi-step etch consisting of five 3 minute etches

4.7.4 Damage inflicted by μP80 during CH_4/H_2 etching

Highest among the advantages proffered by the μP80 was the possibility of a low damage etch process. Ultimately, the only surface damage with which this work is concerned is sidewall damage to the quantum well layers during etching.

When samples were patterned with dots using the PSEM500 and etched using the ET340 then a luminescence signal from dots down to 100nm in diameter could be obtained, but not from dots of diameter 60nm (see section 6.2 for details of the PL experiments). However, using the Jeol CXII to pattern dots and the μP80 to etch them, luminescence from dots down to 35nm in diameter could be obtained (see section 6.3 for further details).

Perhaps it would be unwise to attribute this large difference in the luminescence signal solely to the changeover from the ET340 to the μP80. The following circumstances should also be considered as possibly exerting an influence on the PL signal:

(i) Both the electron beam lithography and the dry etch machine were changed, not just the etch machine. Whether or not the lithography process introduces damage is a moot point, but it seems unlikely because the PL signal from a mesa area is identical to that of the original, unprocessed sample.

(ii) The etch masks used were also different - a negative resist mask was used with the ET340, and a strontium fluoride mask was used with the μP80.

(iii) There was also a slight difference in fill-factor between the samples, with the μP80 sample having closer spaced dots.

Notwithstanding those other factors which tend to obfuscate the principal cause of the lower etch damage, the stronger luminescence signal and the signal detected from smaller dots was a welcome discovery, and one that merited further examination.

4.8 Comparisons between CH_4/H_2 etching in the ET340 and μP80

As stated above, too much had changed and too many factors had been introduced between etching with the ET340 and with the μP80 to allow any definite statements to be made about which process caused greater optically detectable damage. It was mentioned previously (section 4.5) that obtaining a quantitative value of the sidewall damage due to dry etching is not trivial, and because of the necessary work involved and time and expertise required, such experiments are outwith the scope of this present work.

This does not mean that evaluation of the etch damage is impossible, merely that absolute values of the damage inflicted will not be obtained. However, there is still plenty of scope for experiments which compare the level of damage introduced by the two machines, and thereby give a relative indication of the most innocuous etch process.

In order to find the etch process which produced the least damage a series of experiments was initiated. These experiments were tailored to suit the particular needs of this research work - namely, to give an indication of the optically detectable damage. It seemed that the best way of achieving this objective was to choose a multiple quantum well sample (with different quantum well layer thicknesses) as the starting material and to etch a known distance into the material. This could be done for both the ET340 and the μP80, using parameters which were as similar as possible, and the spectra obtained from each could then be compared and any differences examined.

Though simple in theory, these experiments raise several practical problems. Amongst these problems is the need to know the exact etch depth - if this cannot be ascertained accurately then any data obtained is meaningless - and the need to etch the two samples in two different machines to the same depth.

The mask material chosen was a piece of silicon wafer which lay on - and partially covered - the sample surface. Although far from ideal, this mask system was used because it could be removed and replaced very simply and quickly. A Tally-step depth profiler was used to ascertain the etch depth and the sample was re-etched if necessary. As a result of the different etch rates of the two machines those samples etched in the μP80 were inevitably exposed to the gas plasma for a longer period of time than those etched to the same depth in the ET340.

The structure of the samples which were used for these experiments, and also the different depths to which they were etched are shown in figure 4.14. These samples were grown at Thomson-CSF by MOVPE.

Although the diagram indicates that there is a 1nm thick quantum well near the sample surface, this was never detected in the PL spectrum of any of the samples. The absence of this well will not affect the reliability of the etch results because the success of this experiment hinges on the comparison between two etching techniques, and so it only requires that the starting materials are identical (here identical means very similar, there will be some variations across the wafer surface) for each etching process. Since the samples came from the same wafer this is certainly the case.

The first two samples examined were etched to a depth of 30nm (not shown in figure 4.14) and their PL spectra were compared. These spectra are not shown as they are almost identical to the spectrum of the unetched portion. Three quantum wells were detected before and after etching, corresponding to the 5nm, 15nm and 150nm thick wells. After etching there was a slight decrease in the peak luminescence intensity and a slight broadening of the 5nm well but there was no change in the other two wells. This behaviour was the same for the samples etched in both the ET340 and the μP80. The variation in the quantum well PL intensity across the original wafer was such that any attempt to compare PL intensities of the

etched and unetched areas would be hazardous and the results would be accompanied with considerable uncertainty.

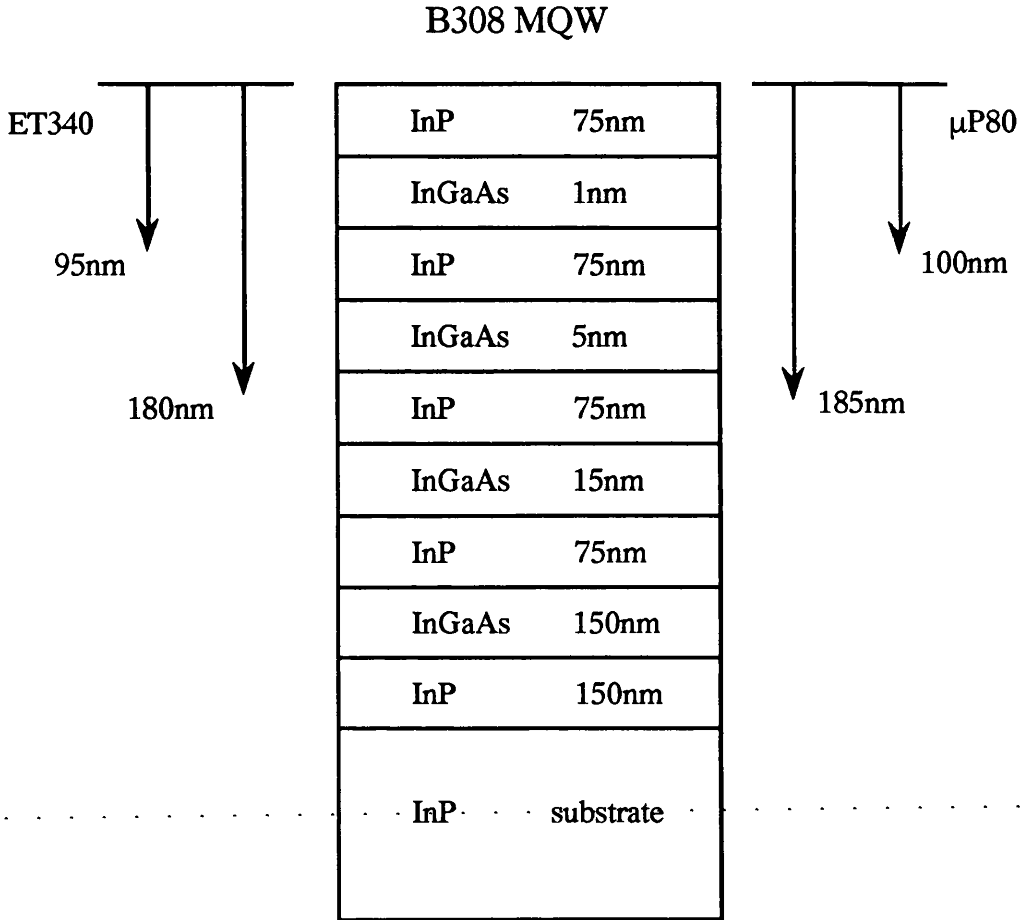

Figure 4.14 Structure of the samples which were used for etch tests, and some examples of the different depths to which these samples were etched.

Another two samples were taken and the topmost 100nm of each sample was removed by etching, one in the ET340 the other in the µP80. The spectrum obtained for the unetched sample, along with the spectrum of the ET340 etched sample are shown in figures 4.15 and 4.16, respectively. The spectrum of the unetched sample, along with the spectrum of the µP80 etched sample are shown in figures 4.17 and 4.18, respectively. The PL spectroscopy conditions were the same for each spectrum, allowing direct comparison between the four

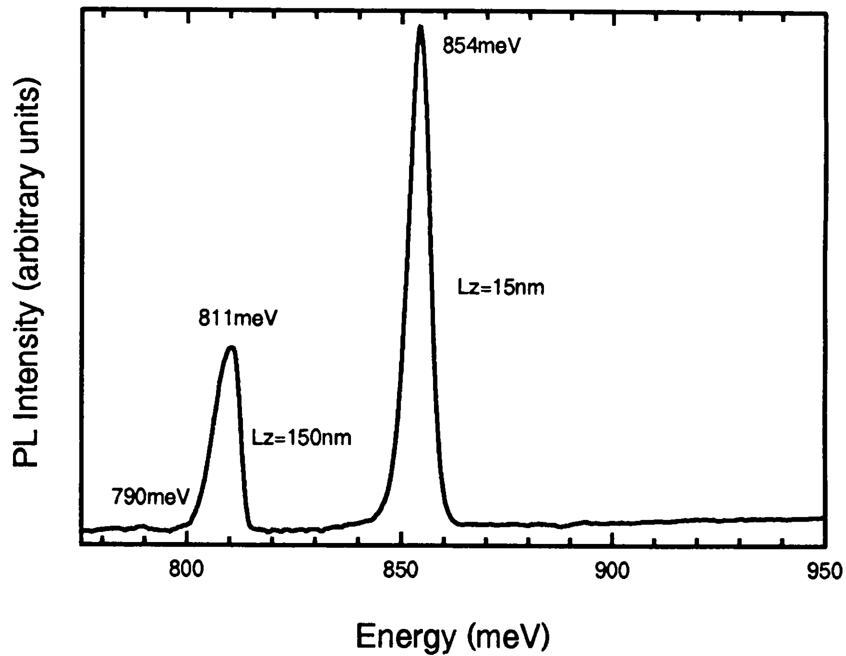

Figure 4.15 PL spectrum of an unetched sample (B308) excited with 100μW of laser power from the 488nm line of an Ar^+ laser. The sample was maintained at 6K while the measurements were taken.

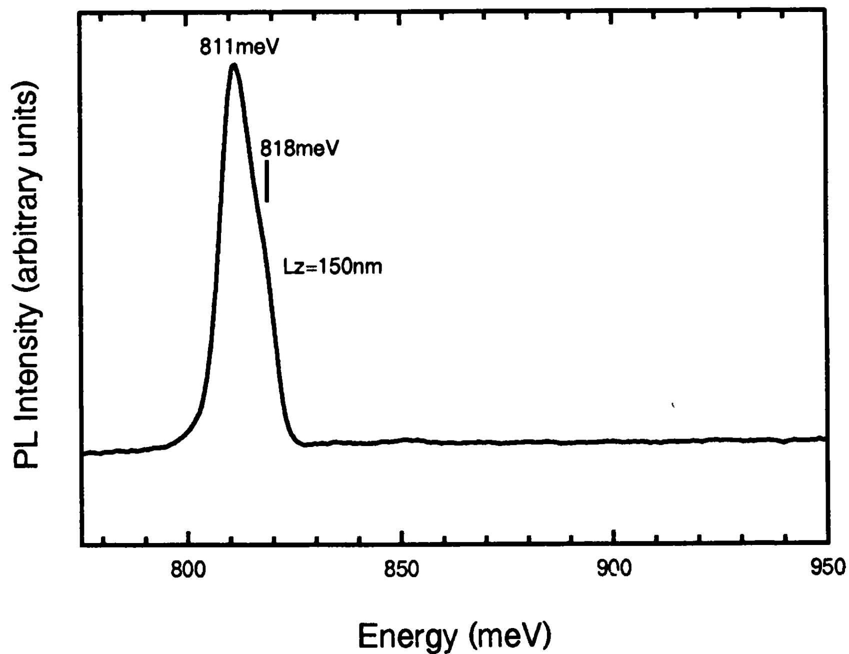

Figure 4.16 PL spectrum of sample B308 after having 95nm removed from its surface by etching in the ET340. The sample was maintained at 6K and probed with 100μW from the 488nm line of an Ar^+ laser. This spectrum shows the absence of the L_z=15nm quantum well.

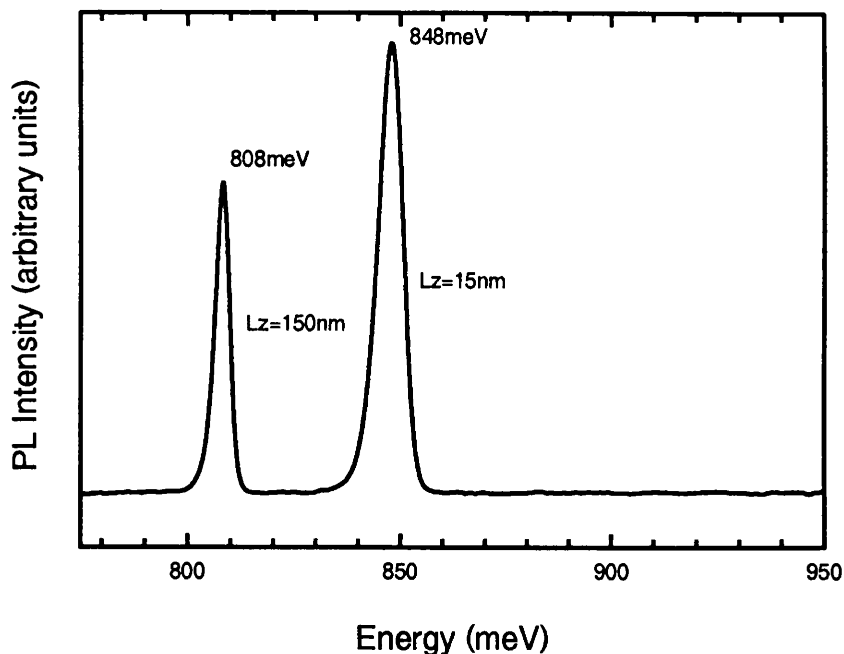

Figure 4.17 PL spectrum of an unetched sample (B308) excited with 100μW of laser power from the 488nm line of an Ar^+ laser. The sample was maintained at 6K while the measurements were taken.

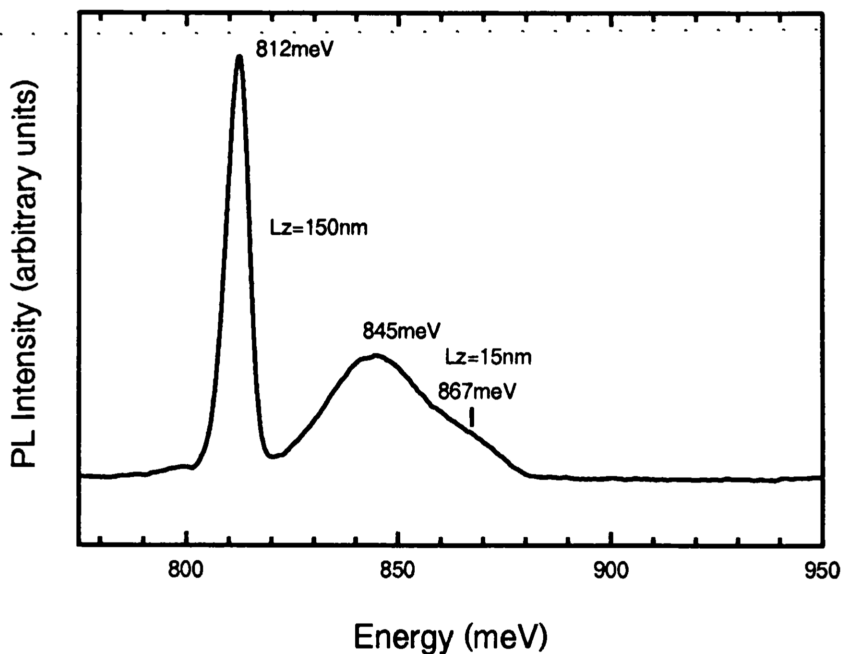

Figure 4.18 PL spectrum of sample B308 after having 100nm removed from its surface by etching in the μP80. The sample was maintained at 6K and probed with 100μW from the 488nm line of an Ar^+ laser. This spectrum shows broadening of the L_z=15nm quantum well.

spectra. The 488nm line of an Argon ion laser was used to excite the samples, the power used was 100μW, and the spectrometer slits were set to a width of 1mm. Table 4.4 shows the positions and full width at half maxima (FWHM) of the peaks shown in figures 4.15 to 4.18, as well as values of the integrated PL intensity of each peak.

Quantum well thickness (nm)	ET 340 unetched	ET340 etched	μP80 unetched	μP80 etched
L_Z=15nm	811meV	811meV	808meV	812meV
L_Z=150nm	854meV	—	848meV	845meV
FWHM of L_Z=15nm	6.9meV	10.9meV	3.7meV	5.8meV
FWHM of L_Z=150nm	9meV	—	6.7meV	26meV
PL Intensity of L_Z=15nm (a.u.)	27	30	14	23
PL Intensity of L_Z=150nm (a.u.)	50	—	32	26

Table 4.4 Positions, FWHM, and Integrated intensities of PL peaks on figures 4.15 to 4.18

The 5nm well is not shown on any of the spectra detailed in figures 4.15 to 4.18. This is because it did not luminesce in either the ET340 or μP80 etched samples (not even so much as a blip in the spectrum was recorded at this energy). However, it did luminesce (at ~1000meV) in both spectra recorded from the unetched portions of sample B308. Omitting the 5nm well from the spectra of figures 4.15 and 4.17 allowed a more expanded energy scale to be used which makes comparisons between the etched and unetched samples easier, while detracting nothing from the useful information.

On comparing figures 4.15 and 4.16 (using the values shown in table 4.4) it is clear that the 5nm (see note immediately above) and 15nm quantum wells did not luminesce after etching in the ET340. This could be due to the introduction of non-radiative recombination centres into the quantum wells. This evidence suggests that etching the sample in the ET340 introduced considerable damage - destroying all optical emission from quantum wells to a depth of at least 150nm, and perhaps to as deep as 220nm. The emission from the 150nm quantum well reveals that the signal is broadened after etching, as shown by an increase in the FWHM (see table 4.4) of the peak, and possibly the introduction of another peak at a slightly higher energy (818meV).

On comparing figures 4.17 and 4.18 it is clear that both quantum wells still luminesce after etching in the μP80, albeit with a broadening of the 15nm quantum well and the appearance of a high energy hump with a peak at approximately 867meV. The 150nm quantum well layer emits strongly with a slight increase in the FWHM but no noticeable additional structure. This suggests that the extent of the damage (as detected optically) is limited to a maximum of approximately 150nm. The difference in the PL peak, which goes from 808meV to 812meV, is probably due to variations across the original sample surface, rather than a process/etching induced shift. Figure 4.17 shows this PL peak to occur at 811meV which is in good agreement with the value obtained for the etched sample in figure 4.18.

Contrasting the spectra of the samples etched in the two different machines it seems plain that the ET340 introduces more optically detectable damage than the μP80. Since this may seem to be too sweeping a statement to make in the light of just one experiment, a further experiment was performed in order to verify that this was indeed true.

Two fresh samples were prepared and the topmost 180nm of each sample was etched away. The spectrum obtained for the unetched part of the first sample and the corresponding spectrum of the portion etched in the ET340 are shown in figures 4.19 and 4.20 respectively. The spectrum of the unetched part of the second sample and the corresponding spectrum of the portion etched in the μP80 are shown in figures 4.21 and 4.22 respectively. Once again, the PL spectroscopy conditions were the same for each spectrum and the same as given above.

Even a cursory glance at figures 4.20 and 4.22 shows that the spectra of each sample - both the ET340 etched and the μP80 etched sample - shows additional features and considerable broadening of the peaks.

Comparing figures 4.19 and 4.20 certain features are immediately apparent. The 15nm quantum well which emits at 854meV on the control part of the sample (figure 4.19) is absent from the etched spectrum, which suggests that it is completely quenched after etching in the ET340. Figure 4.20 seems to be composed of three peaks, the first of these (a shoulder rather than a peak) occurs at 829meV, the next at 809meV (which corresponds to the 150nm quantum well) and the third at 796meV. Although neither figure 4.19 nor figure 4.21 show a peak at this energy, other PL spectra recorded from the original samples did reveal a weak peak at approximately 791meV. This suggests that this feature is part of the original sample and not an etching induced feature.

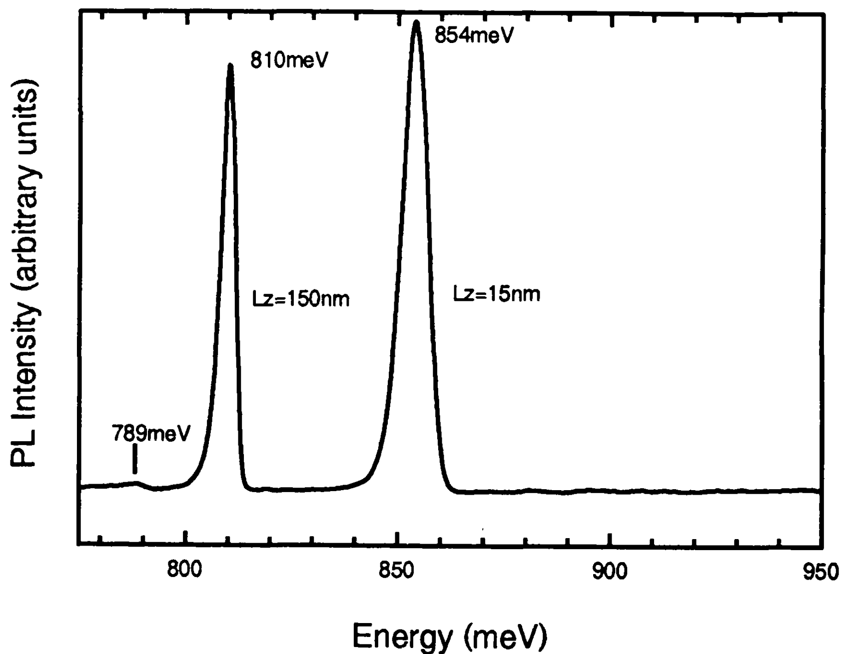

Figure 4.19 PL spectrum of an unetched sample (B308) excited with 100μW of laser power from the 488nm line of an Ar^+ laser. The sample was maintained at 6K while the measurements were taken.

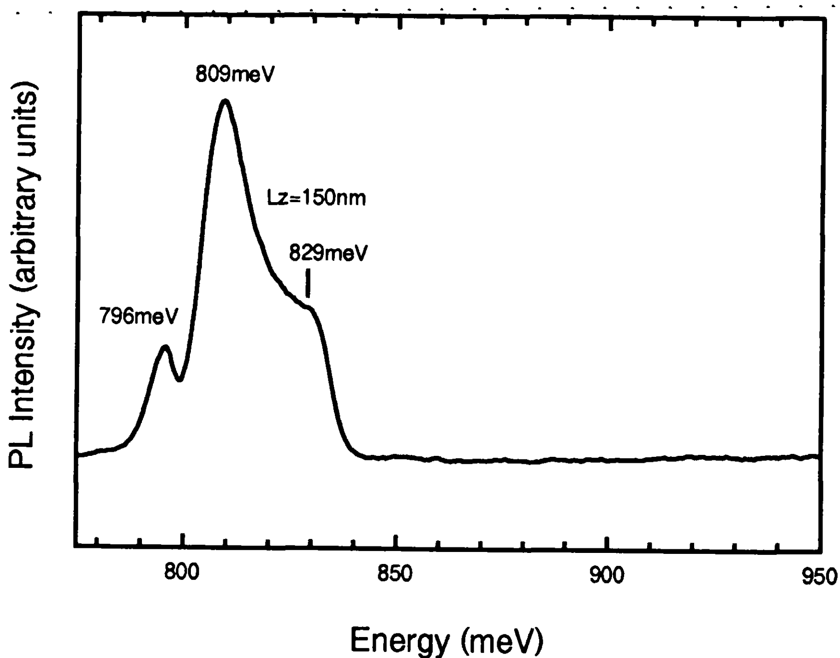

Figure 4.20 PL spectrum of sample B308 after having 180nm removed from its surface by etching in the ET340. The sample was maintained at 6K and probed with 100μW from the 488nm line of an Ar^+ laser. This spectrum shows the absence of the L_z=15nm quantum well and broadening of the L_z=150nm well.

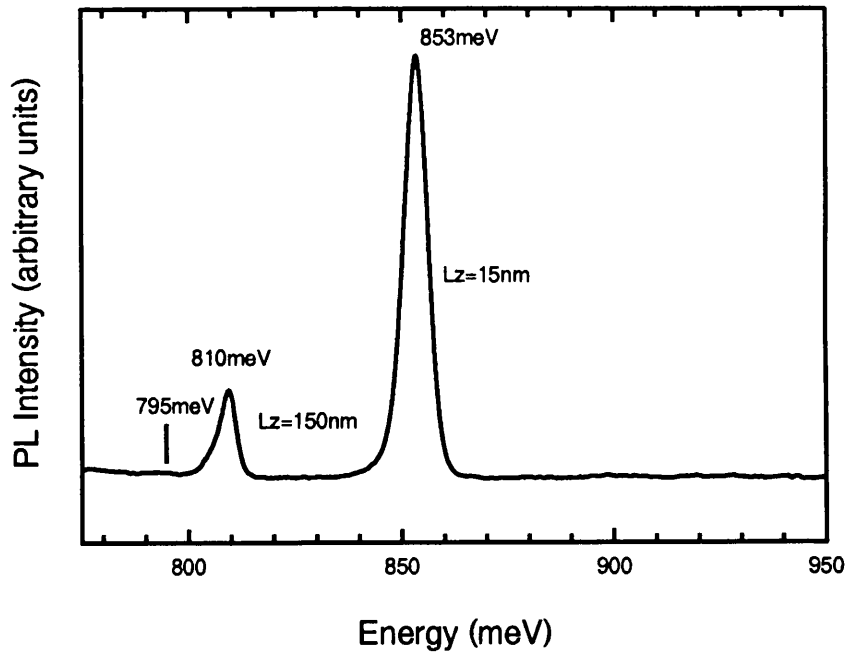

Figure 4.21 PL spectrum of an unetched sample (B308) excited with 100μW of laser power from the 488nm line of an Ar^+ laser. The sample was maintained at 6K while the measurements were taken.

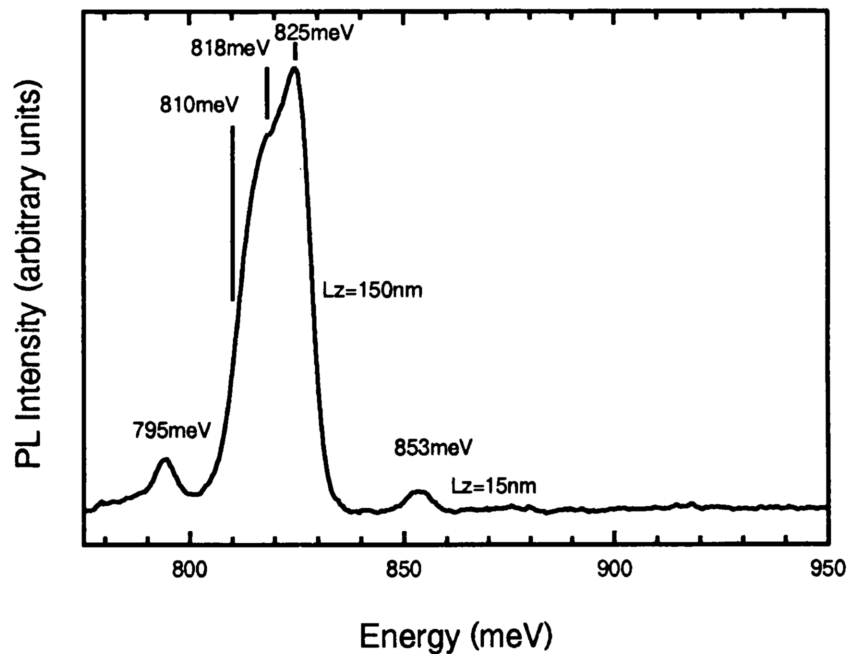

Figure 4.22 PL spectrum of sample B308 after having 185nm removed from its surface by etching in the μP80. The sample was maintained at 6K and probed with 100μW from the 488nm line of an Ar^+ laser.

The integrated luminescence intensity of figure 4.20 is 43×10^6 compared with a corresponding value of 46×10^6 for the control part of the sample shown in figure 4.19. This shows that the integrated intensities of the control and etched samples are very similar.

On examining figure 4.22 it is apparent that the 15nm quantum well still luminesces after etching, albeit very weakly. In addition to this peak there are another two peaks and a shoulder on the spectrum. The main peak on the spectrum occurs at 825meV and seems to correspond to the peak on figure 4.20 which occurs at 829meV. This peak has a shoulder at 818meV. Again, a small peak appears at 795meV which corresponds to the one occurring at 796meV on figure 4.20. The integrated luminescence intensity of figure 4.22 is 25×10^6 compared with a value of 30×10^6 for figure 4.21; again, these two values are very similar.

It is clear from both figures 4.22 and 4.20 that both etch machines produce large amounts of optically detectable damage. It seems that the µP80 produces less damage than the ET340 because luminescence can still be detected from the 15nm quantum well after etching, whereas the ET340 quenches all of this quantum well's luminescence. Both samples were etched to within 46nm of the 15nm quantum well; and so it is interesting that after etching in the µP80 this well still emits but there are also additional features which are probably associated with the much deeper 150nm quantum well.

One further sample was etched in the µP80 to a depth of 50nm. The spectrum obtained after etching was almost identical to the one of the unetched portion, the only difference being a 10% increase in the FWHM of the each well after etching. The integrated luminescence intensity after etching was the same as that prior to etching (it showed a 50% increase but this was within the experimental error).

From these experiments there seems to be some justification in saying that the µP80 induces lower optically detectable damage than the ET340 under the above etching conditions. It should be borne in mind, however, that these etches all relate to damage induced when the surface is etched without an etching mask being present. They give no clear, unambiguous indication of the extent of sidewall damage, which is the most important aspect of this work on quantum wire and dot fabrication.

References

Adesida I, Nummila K, Andideh E, Hughes J, Caneau C, Bhat R and Holmstrom R, 1990 J Vac Sci Technol B8 (6) p1357-1360

Andideh E, Adesida I, Brook T, Caneau C and Keramidas V, 1989 J Vac Sci Technol B7 (6) p1841-1845

Arnot H E G, 1990 PhD Thesis, University of Glasgow

Carter A J, Thomas B, Morgan D V, Bhardwaj J K, McQuarrie A M and Stephens M A, 1989 IEE proceesings Vol 136 No1 p2-5

Chapman B, 1980 "Glow discharge processes" John Wiley and Sons, New York

Coburn J W and Winters H F, 1979 J Vac Sci Technol 16 (2) p391-403

Coldren L A and Rentschler J A, 1981 J Vac Sci Technol 19 (2) p225-230

Doughty G F, Thoms S T, Law V and Wilkinson C D W, 1986 Vacuum vol 36 Nos. 10/11 p803-806

Germann R, Forchel A and Grützmacher D, 1989 Appl Phys Lett 55 (21) p2196-2198

Hayes T R, Dreisbuch M A, Thomas P M, Dautremont-Smith W C and Heimbrook L A, 1989 J Vac Sci Technol B7 (5) p1130-1140

Henry L, Vaudry C and Granjoux P, 1987 Electronics Letters Vol 23 No 24 p1253-1254

Hu E L and Howard R E, 1980 Appl Phys Lett 37 (11) p1022-1024

Lehmann H W, 1985 Springer Proc in Physics p65-82, Springer Verlong, Heidelberg

McNabb J W, Craighead H G, Temkin H and Logan R A, 1991 J Vac Sci Technol B9 (6) p3535-3537

McNevin S C, 1986 J Vac Sci Technol B4 p1216

Niggebrügge U, Klug M and Garus G, 1985 Inst Phys Conf Series No.79, Int Symp on GaAs and Related Compounds, Japan, p367-372.

Pajot B, Chevallier J, Jalil A and Rose B, 1989 Semicondustor Science and Technology 4 p91-94

Ruska W S, 1987 "Microelectronics processing" McGraw-Hill

Stern M B and Liao P F, 1983 J Vac Sci Technol B1 (4) p1053-1055

Thomas D J and Clements S J unpublished results

van Roosmalen A J, van den Hoek W G M and Kalter H, 1985 J Appl Phys 58 (2) p653-658

Watt M, Sotomayor Torres C M, Cheung R, Wilkinson C D W, Arnot H E G and Beaumont S P, 1988 Journal of Modern Optics Vol 35 p365

Chapter 5 Experimental techniques and apparatus

5.1 Introduction to luminescence spectroscopy

Luminescence is the term given to the optical radiation emitted by a material when its charge carriers are excited across the energy gap and then recombine radiatively. There are four processes which occur: creation of electron - hole pairs by absorption of the incident energy; relaxation of the carriers down to the lowest energy levels; radiative recombination of electron - hole pairs; and escape of the recombination radiation from the sample.

Throughout this research a number of spectroscopic techniques were used to evaluate the effects of patterning wire and dot nanostructures onto quantum well samples.

5.1.1 Photoluminescence spectroscopy (PL)

By far the most frequently used technique in this research was photoluminescence spectroscopy (PL). As the name suggests, PL uses photons to excite the sample and produce electron - hole pairs. The reason that this technique is so commonly used is because it is a very simple experiment to perform which is non-destructive and doesn't require meticulous sample preparation (Bebb and Williams, 1973).

The other photon based luminescence technique which is commonly used to assess samples is photoluminescence excitation (PLE). This experiment yields information which is complementary to that which can be obtained by PL, such as information on the higher energy levels, and so it greatly assists in interpreting the PL spectra (Rogers et al, 1991).

In PL, photons with energy greater than the semiconductor band gap energy are used to excite carriers in the semiconductor. The electron-hole pairs produced relax down to the

lowest energy levels in the conduction and valence band, respectively. In pure crystals they form an exciton and then recombine emitting a photon of energy which corresponds to the exciton energy. Thus when a spectrometer is used to scan across an energy range a sharp peak is detected at the particular energy (wavelength) which corresponds to the exciton recombination. In a quantum well system it is possible to select an excitation source which emits photons of sufficient energy to excite carriers in both the quantum well and barrier material; the other possibility is to choose an excitation source which emits photons with sufficient energy to excite charge carriers in the quantum well layer, but not in the barrier layer. These processes are depicted in figure 5.1.

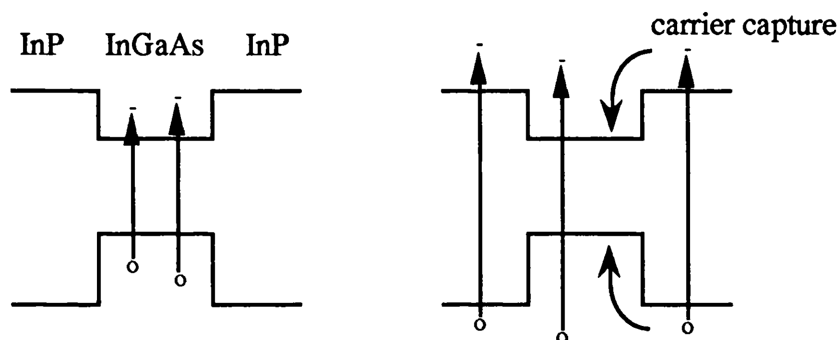

Figure 5.1 Excitation processes in quantum wells

In essence, a laser PL experiment consists of a coherent energy source to create carriers, a spectrometer to disperse the incoming light and to scan a wavelength (energy) range and a photodetector to record the luminescence intensity at each energy.

One disadvantage of PL spectroscopy is that it only probes the lowest energy level transition: no information is given about higher energy levels. Collating information on these higher energy levels requires the use of other techniques. One such technique is PLE.

5.1.2 Photoluminescence excitation (PLE)

In PLE of quantum wells a tunable excitation source is used (as opposed to PL which uses a source of fixed energy, e.g. a laser). The spectrometer which is used to detect the signal does not scan a wavelength (energy) range but is fixed at one set wavelength - the wavelength which corresponds to the lowest recombination energy. The excitation source - not the spectrometer - is then varied from low energies (equal to the lowest exciton energy) up to the energy of the band gap of the barrier material, and the luminescence of the lowest exciton level is recorded in conjunction with the excitation energy. These two parameters are then plotted against each other and a spectrum is obtained.

The intensity of the luminescence of the lowest exciton energy level depends on the strength of the absorption transitions available at a particular excitation energy. Thus the PLE experiment mirrors the absorption of a material because of the increased absorption whenever the exciting energy is sufficient to populate another energy level (Hamilton et al, 1988). This is shown schematically in figure 5.2. The upward arrows indicate an absorption process and the downward arrow indicates an emission process.

PLE is a useful technique because it gives similar information to absorption measurements whilst exploiting the high luminescence efficiency of quantum wells and thus providing stronger signals than would be expected with standard absorption measurements (Rogers et al, 1991). It also obviates the detailed sample preparation which is sometimes needed with absorption measurements.

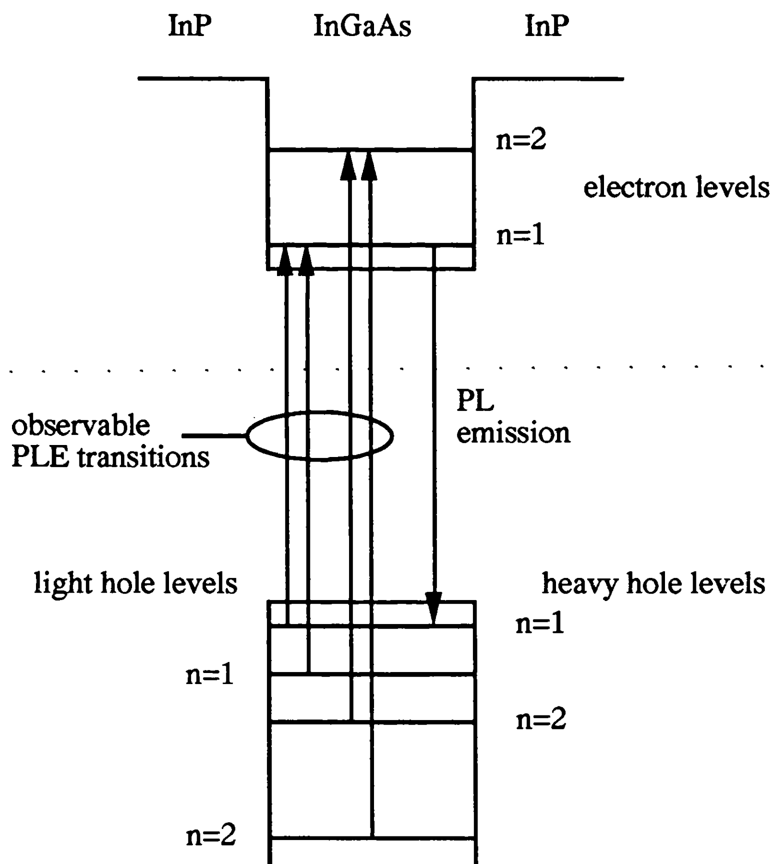

Figure 5.2 Schematic diagram of observable PLE transitions

5.1.3 Cathodoluminescence (CL)

A third luminescence technique is cathodoluminescence (CL). The main difference between PL, PLE and this process is that PL and PLE use photons to excite the carriers in the semiconductor, whereas CL uses an electron beam to excite the carriers. Although CL is less

efficient at producing carriers than techniques which rely on optically pumping a semiconductor, CL offers several useful features which account for its growing popularity in characterising nanostructure fabrication. One of the advantages of CL is that it can be used for imaging nanostructure arrays, and thus provide information on whether all of the dots in an array luminesce or whether some luminesce strongly and others don't luminesce at all (Williams et al, 1991, Sotomayor et al, 1992). CL has also been used to monitor the luminescence of wires, giving information on how the luminescence changes along a wire, with the appearance of dark areas and bright areas corresponding to poor and strong luminescence respectively (Samuelson et al, 1992).

The spatial resolution of a CL kit is typically of the order of 1μm; however, Nilsson et al (1991) claim that their CL apparatus yields a spatial resolution of 0.2μm. Another difference between CL and photon-based systems is that the electrons which are used in CL are highly energetic and so they penetrate much further into samples than photons.

5.2 Absorption experiments

Unlike PL, PLE, or CL experiments, which are all based on the emission of radiative recombination, absorption experiments - as the name implies - rely on the absorbing properties of the material.

The basic concepts which underlie the absorption experiments are as follows. When a material is subjected to light of sufficient energy it absorbs the radiation until all of the quantum states at that energy and within the absorption length at that wavelength are full. In low dimensional semiconductors which have comparatively few quantum states the absorption increases suddenly when a new energy level (which provides more quantum states) is reached.

The experimental apparatus usually consists of a light source which has an emission over a broad energy range. A monochromator is placed in front of the source and is used to select a particular wavelength (in reality it selects a small range of wavelengths). The monochromator is driven by a motor so that it can be scanned from one end of the wavelength range to the other.

The spectrum corresponding to the light source with no sample in place is recorded, then the sample is inserted between the monochromator and spectrometer and the spectrum corresponding to the light transmitted through the sample is recorded. The absorption spectrum is obtained by dividing the transmitted spectrum by the original spectrum (recorded with no sample in place). A diagram of typical absorption experimental apparatus is shown in figure 5.3.

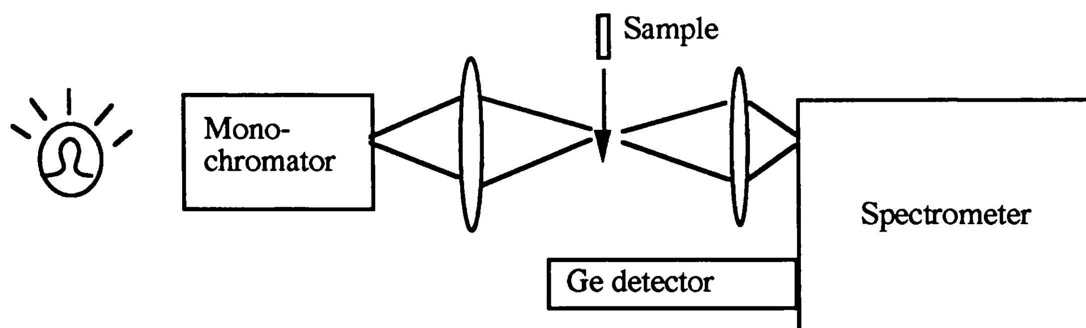

Figure 5.3 Typical apparatus for absorption experiments

The advantage of the absorption experiment is that it provides information on the different energy levels of the sample; in that respect it is like PLE. However, absorption experiments can only be performed on certain material types.

If the material which serves as the quantum well is also used as the substrate then the sample cannot be used without first removing the substrate, otherwise the substrate would absorb the incoming light and so yield spurious results. An example of this is the GaAs/AlGaAs system, where the GaAs substrate needs to be removed in a wet chemical etch.

In contrast, the InP/InGaAs system is ideal for absorption experiments because the quantum well layer is the ternary and the substrate is the binary (InP), and so absorption experiments can be performed on InGaAs/InP without the meticulous sample preparation required for the GaAs/AlGAs material system.

5.3 Photoluminescence apparatus

The experimental apparatus which was used for PL spectroscopy by the Nanoelectronics group at Glasgow University has been well documented in the PhD theses by Arnot (1990), Rodden (1993) and Leitch (1993) and so only a brief account will be given here. A diagram of the apparatus used is given in figure 5.4.

The numbers shown in figure 5.4 are used to identify a piece of equipment and a description of each item is given in the key below opposite each number.

Number 1 is the laser which is used to excite the sample. Two lasers were used throughout this research. One was a 5.6mW Helium-Neon 633nm laser and the other was a 2W Spectra Physics Stabilite 2016-05 Argon ion laser. The 488nm line of the Argon ion laser was the only line of that laser which was used for the PL experiments.

Number 2 is a Spectrolab electro-optics laserspec III laser filter monochromator which was used in conjunction with the Argon ion laser to ensure that only the 488nm wavelength line was used to excite the sample.

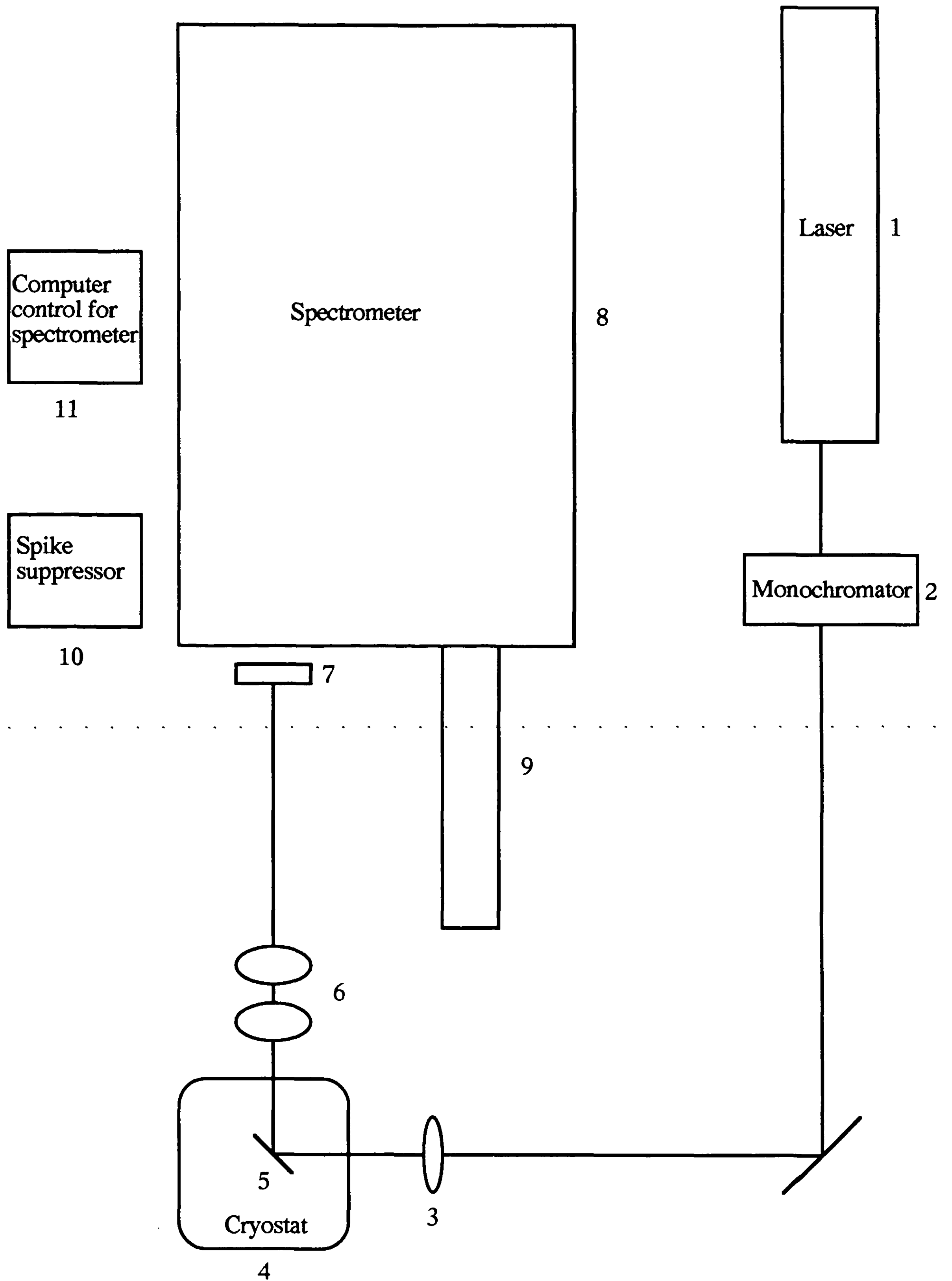

Figure 5.4 Plan diagram of the PL experimental apparatus

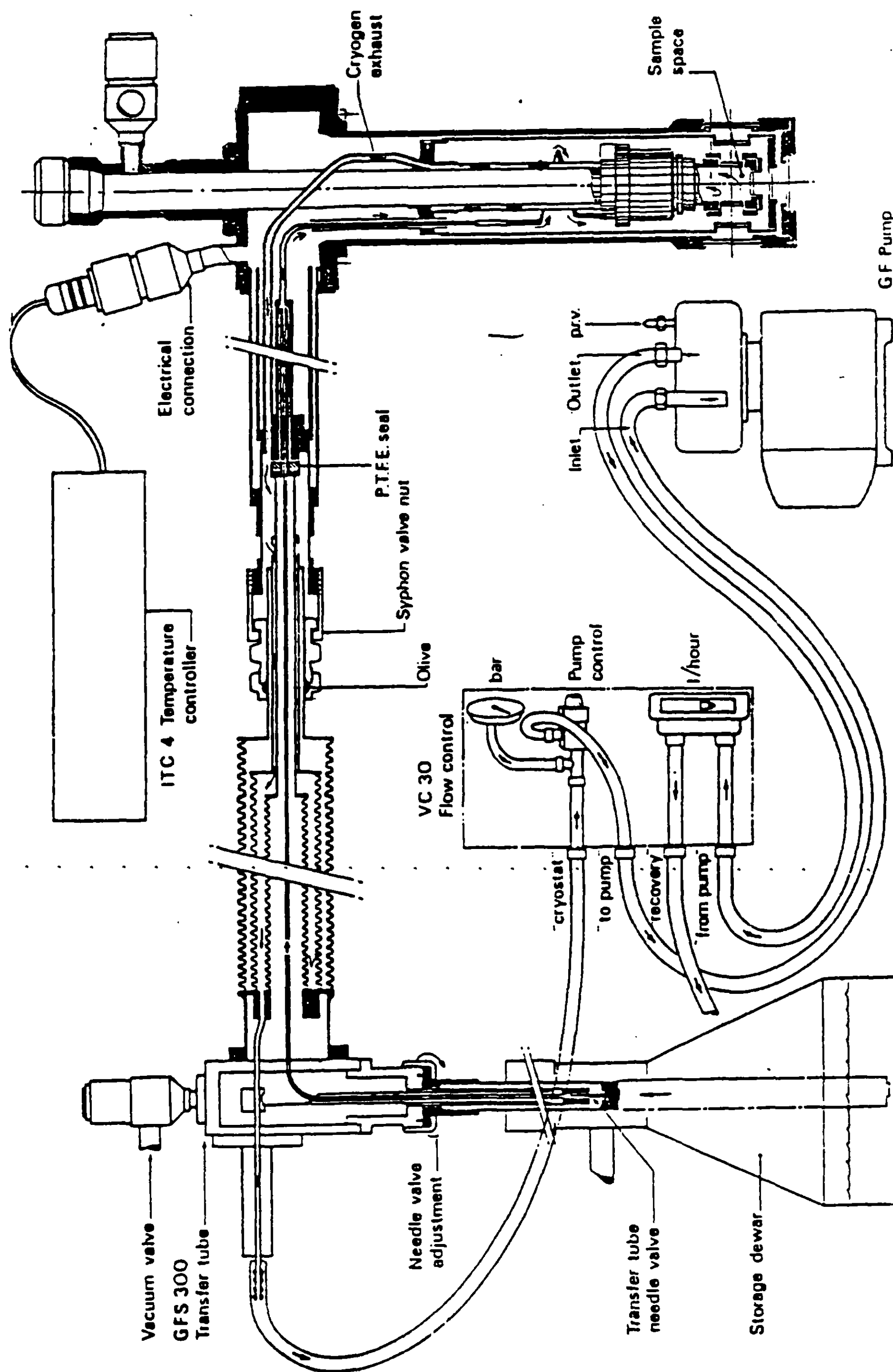

Figure 5.5 Diagram of helium cooling system (after Oxford Instruments manual)

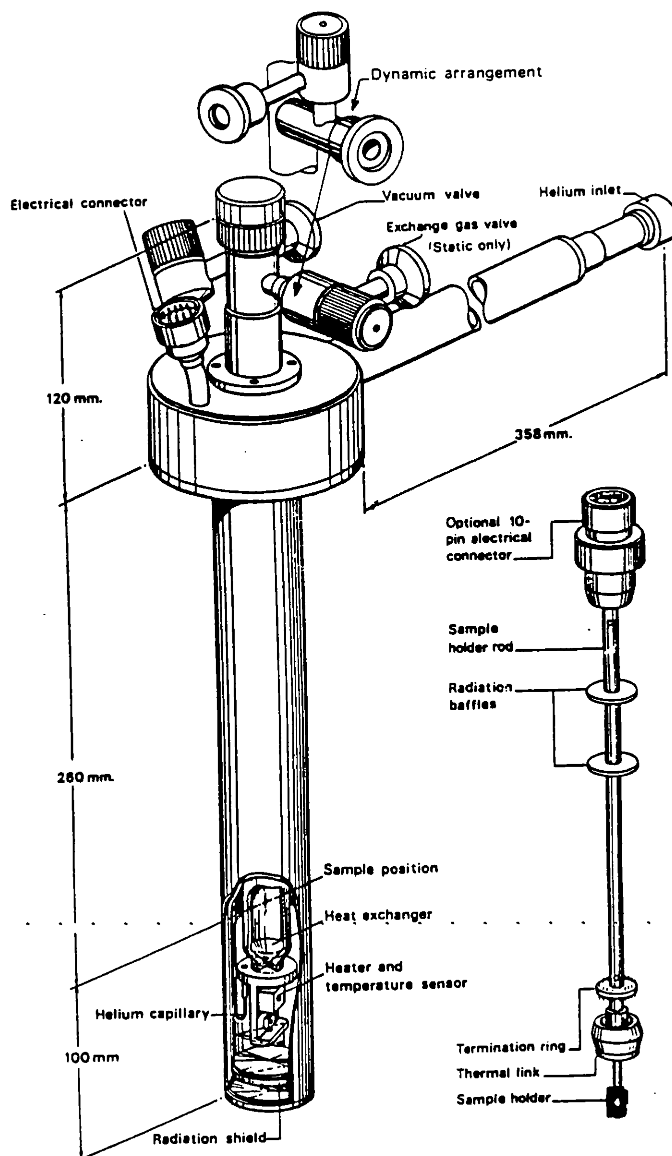

Figure 5.6 CF1204 cryostat and insert rod (after Oxford Instruments manual)

When the 633nm wavelength Helium-Neon laser was used the Spectrolab monochromator was not needed, instead a 35-5990 0990 Ealing bandpass filter was used to remove any plasma lines and allow only the 633nm line to be transmitted.

Number 3 is an Ealing 60mm focal length, 0.07 NA microscope objective lens which is mounted on an X-Y-Z translational mount. This lens is used to focus the laser beam down to a spot of approximately 70μm in diameter.

Number 4 is an Oxford Instruments CF1204 continuous flow cryostat. The cryostat has a dynamic facility, which means that it allows the sample space to be filled with liquid helium. The gaseous helium above the liquid helium is then continuously extracted by a two-stage rotary pump, creating a low pressure region above the liquid helium. This enables temperatures as low as 2.2K to be maintained in the sample space.

However, in these experiments the cryostat was not used in this way but in the gas mode. In this mode the sample was cooled by a continuous flow of cold gas which passed over it and then the helium gas was pumped out through an exhaust line.

Figure 5.5 shows the helium transfer tube and how it connects to the cryostat, and the cryostat itself is shown in figure 5.6. The inset of figure 5.6 shows a diagram of the cryostat insert which was used for holding the mounted samples.

Number 5 is the sample which is mounted on the cryostat insert rod. The sample is first mounted on a copper block by glueing it in place with a paste which consists of Bostick glue dissolved in acetone and then the copper block is screwed onto the base of the cryostat insert rod. A diagram of the cryostat insert rod is shown in the inset of figure 5.6 The insert rod was designed to enable the sample to be adjusted in the vertical direction. This vertical adjustment was of great use in obtaining photoluminescence from patterns with very low signals. This is because a signal can be obtained and optimised from a mesa - or other strongly emitting array - which is above the site of interest, and then without moving either the laser spot or collecting optics the insert can be adjusted to move the weakly emitting array to exactly the same position which was previously occupied by the mesa.

Number 6 is the collecting optics. It is a 60-300mm Sirius zoom lens (F4 - 5.6), which is a commercially available 35mm SLR camera lens mounted onto an X-Y-Z translational stage. As can be seen from figure 5.4, a 90° backscattering geometry was used for these experiments. This geometry has the advantage of providing accurate information on which part of the sample is being illuminated because the sample is enlarged and imaged by the collecting optics. The zoom lens enabled imaging of the sample onto a white screen placed temporarily in front of the entrance slit of the spectrometer. This technique permitted precise positioning of the laser beam onto a patterned area of the sample.

Number 7 is an RG695 filter which is placed immediately in front of the spectrometer entrance slit. This filter is a cadmium selenide sulphide doped glass which blocks the passage of radiation of wavelength less than 695nm (and so it ensures that the Ar and HeNe laser beams are not transmitted) but allows radiation of wavelength greater than 695nm to pass through without significant attenuation.

Number 8 is an Instruments SA THR1000 1metre spectrometer. The THR1000 has a maximum possible resolution of 0.001nm (although this level of resolution was not required for the PL experiments on quantum wires or dots) and a stray light rejection of 10^{-5} measured eight bandpasses of the spectrometer away from the 632.8nm line of a helium neon laser. The gratings used in this spectrometer measured 10cm by 10cm square and had 600 lines per mm. Figure 5.7 shows a graph of efficiency versus energy for light polarised perpendicular to the grooves, light polarised parallel to the grooves and unpolarised light (from THR1000 instruction manual).

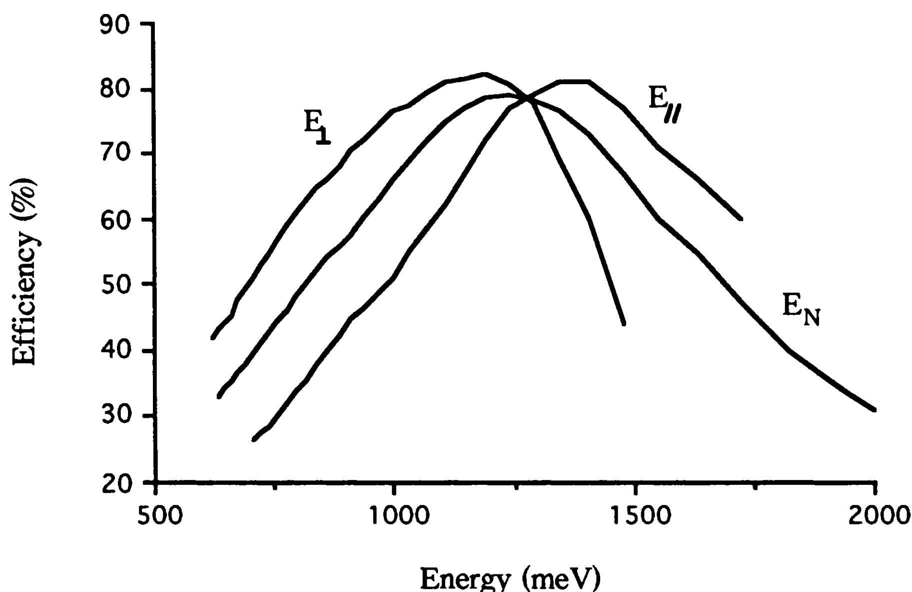

Figure 5.7 Grating efficiency curves for 600 grooves per mm gratings: $E_\perp$ for light polarised perpendicular to the grooves; $E_{//}$ for light polarised parallel to the grooves; and E_N for unpolarised light.

Number 9 is a North Coast Scientific Corporation EO-817L germanium detector, which is a germanium PIN diode device powered by a -250V power supply. The detector can be used to detect radiation in the wavelength range from 800nm to 1700nm.

Number 10 is an electronic device which is necessary because the reversed biased germanium PIN diode is also an excellent detector of nuclear radiation, particularly cosmic muons. These cosmic muons produce large, brief signal spikes which can seriously disrupt the computer software which is used to collate the signal data. For this reason these spurious spikes must be removed and this is done by using an electronic circuit originally described by Collins and Jeffries, 1982.

Number 11 is the computer control for the spectrometer and the automatic data acquisition which is done by Instruments SA PRISM software.

In order to obtain the overall spectral response of the apparatus, an 80W white-light lamp source was used which approximates the blackbody radiation spectrum at 3200K and a spectrum was recorded. This spectrum is shown in figure 5.8 together with the theoretical curve for a blackbody at 3200K. This curve is given by equation 5.1 (Handbook of Physics and Chemistry, 1982):

$$P \propto \frac{\lambda^{-5}}{\left[\exp\left(\frac{hc}{kT\lambda}\right) - 1\right]} \qquad 5.1$$

where P is the energy emitted per unit time between wavelengths λ and $d\lambda$, λ is the wavelength, h is Planck's constant, c is the speed of light, k is Boltzmann's constant and T is the absolute temperature (K).

Throughout this work, what is of primary concern is to obtain a comparison between a processed and an unprocessed sample and so the absolute values of intensity (which could be obtained by normalising all of the spectra using the difference between the experimental and theoretical curves shown in figure 5.8) are not particularly important. As a result of this, unless stated, none of the spectra has been normalised.

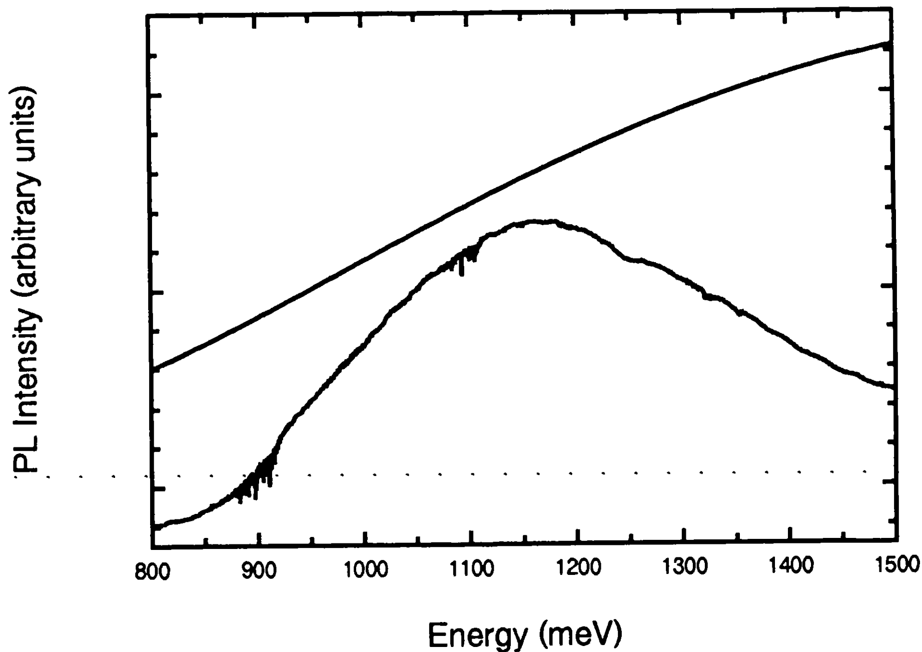

Figure 5.8 Experimental (lower) and theoretical (upper) spectra of a blackbody source

5.3.1 PL apparatus - experimental method

When PL experiments were performed on samples fabricated by the Beamwriter a problem was encountered. When a weakly emitting array was probed (with a necessarily high laser power) the PL spectra obtained was influenced by neighbouring arrays (such as mesas) and therefore it was unreliable. To overcome this problem the sample was scribed into individual arrays and these arrays were mounted onto the copper block holder for the cryostat, with each array spatially separated from its neighbour. This ensured that the PL signal recorded originated only from the array which was being probed.

5.4 The Fast Fourier Transform (FFT) spectrometer

Some experiments were performed in conjunction with Dr R Pritchard at UMIST using an FFT spectrometer. The FFT spectrometer is an extremely versatile piece of apparatus. It can be configured in several different ways, which allows PL, PLE and absorption experiments to be performed.

The particular FFT spectrometer used at UMIST was a BIO-RAD FT60A. It contains an infra-red source, a Michelson interferometer and the optics necessary to direct the modulated beam onto the sample. The spectrometer also houses the electronic components which are necessary to control the interferometer. A diagram of the BIO-RAD FT60A is shown in figure 5.9 and a diagram of the Michelson interferometer is shown in figure 5.10 (taken from the BIO-RAD instruction manual).

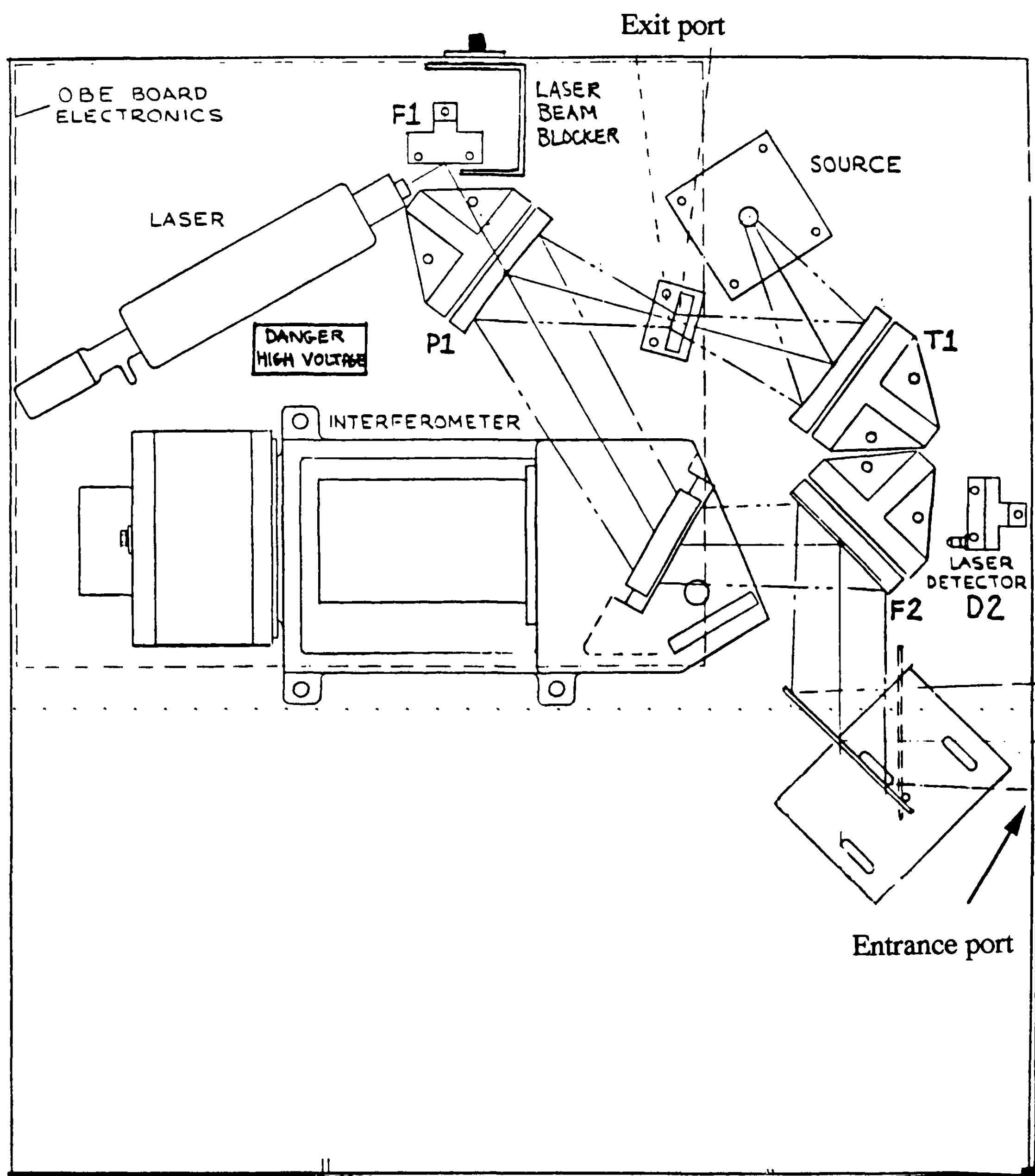

Figure 5.9 Diagram of BIO-RAD FT60A FFT spectrometer

Figure 5.10 Diagram of the Michelson interferometer used in the BIO-RAD FT60A FFT spectrometer

Absorption experiments are performed using a broad-band (almost black-body) source which is a quartz halogen lamp situated inside the FFT spectrometer. The light is collimated inside the FFT spectrometer, passed through the Michelson interferometer and emerges as a collimated, frequency encoded beam which is then focused onto the sample (Hamilton et al, 1988). For low temperature absorption experiments the sample is located inside an Oxford instruments cryostat (similar to the one described in section 5.3) and cooled to 5K. Initially, a reference spectrum is recorded with no sample in place. The sample is then inserted and further spectra are recorded. The computer control automatically divides the spectra obtained by the reference spectrum and so displays the actual absorption spectrum. A schematic diagram of the arrangement is shown in figure 5.11.

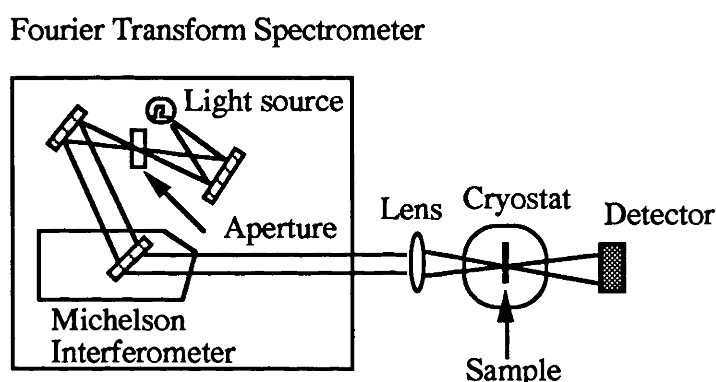

Figure 5.11 FFT spectrometer configuration for absorption experiments

The advantage of this technique, when compared with conventional techniques using a monochromator and spectrometer pair (see figure 5.3), lies in the multiplexing of the source and detection energies. The entire range of energies of interest are used to illuminate the sample and the transmitted energy/intensity relation can be recorded in a few seconds. In practice this means that hundreds of spectra can be recorded and accumulated thus reducing the effect of noise on the spectrum.

Some PL experiments were also performed using this spectrometer. For PL experiments the spectrometer was configured in its usual manner. The configuration of the equipment is shown diagramatically in figure 5.12.

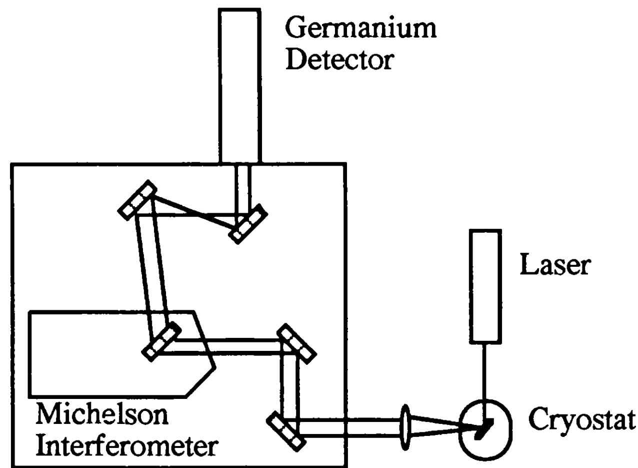

Figure 5.12 PL configuration of FFT spectrometer

PLE experiments could not be performed on any of the samples which were patterned with nanostructures for this research. The problem arose because of the need to separate spatially the excitation radiation and the PL emission, which gave rise to the experimental configuration shown in figure 5.13. As shown in figure 5.13 the PLE signal is extracted from the side of the sample - and so this method is only suitable for quantum well (unpatterned) samples.

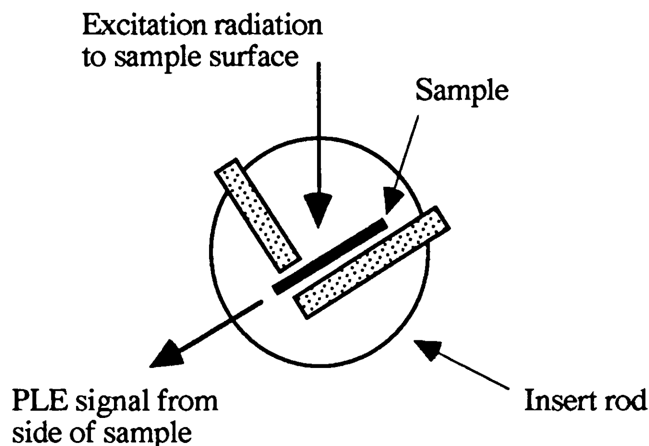

Figure 5.13 Plan view of sample holder for PLE experiments

One other series of measurements was performed at UMIST, these were spatially resolved PL experiments. Again this used the FFT spectrometer in its normal (i.e. detecting) mode. A diagram of the apparatus is shown in figure 5.14 (taken from Pritchard, 1992). The laser excitation source is focused to a spot 2μm in diameter by a microscope objective lens. A special cryostat is used which enables the sample to be brought very close to the lens,

which is necessary because of the short focal length (15mm) of the lens. The cryostat was cooled by liquid nitrogen (down to 77K) and the laser beam was moved across the sample surface by a two-axis stepper motor system (x-y stage) which is geared and compensated for backlash (Pritchard et al, 1992). This allows movement of the laser beam in 2μm steps. Sample navigation is eased by the use of a CCD camera viewing system with a removable de-focusing lens. The PL signal is directed to the FFT spectrometer (which is configured for PL experiments, as shown in figure 5.12) by a series of mirrors and the spectrum is recorded using a North Coast germanium detector (as described in section 5.3).

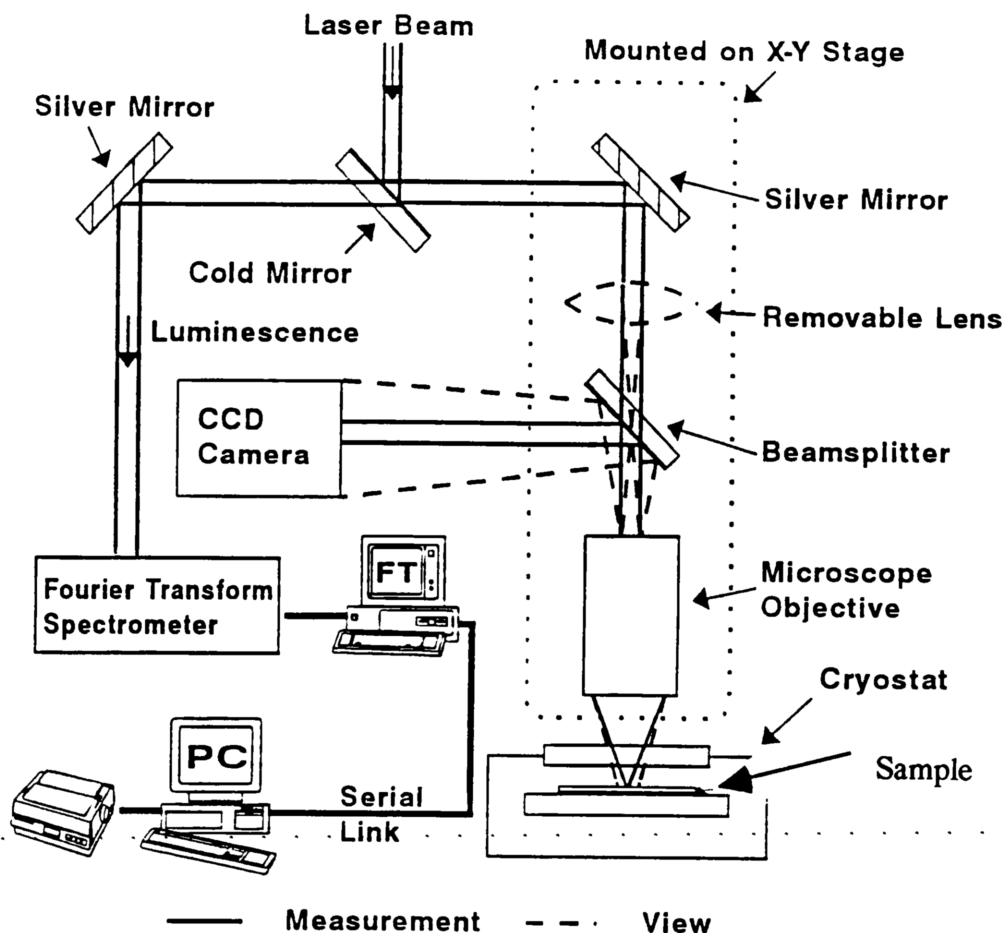

Figure 5.14 Spatially resolved PL experimental apparatus

5.5 Summary of nanostructure characterisation techniques

Having fabricated structures with dimensions of the order of 10nm it is vital to be able to characterise them accurately. Several techniques have been mentioned in this chapter, these include conventional PL, PLE and absorption experiments, the FFT spectrometer equivalents of these three, spatially resolved PL and CL.

Ideally, it would be good to obtain luminescence (of whatever kind - photo or cathodo) from just a few of these nanostructures so that small arrays could be fabricated and the sizes of each of the dots or wires measured. This might reveal whether the broad luminescence observed (to a greater or lesser degree) by every research group originates from structures (dots or wires) of different physical sizes or whether this broad luminescence would emanate from even one dot.

However, all of the techniques mentioned above must do battle with the low signal levels which are emitted by nanostructures. This hampers the quest for information on the energy levels in the nanostructures, which is necessary in order to characterise the samples fully.

The spatial resolution of the standard PL and PLE measurements (for both the conventional and FFT based spectrometers) depends (to an extent) on the diameter of the beam which is used to excite the sample. As a consequence of the low signal levels emanating from the nanostructures high laser powers are required (~1mW) and so the beam diameter cannot be reduced substantially because the very high power density would induce local sample heating.

The spatial resolution of the CL apparatus at the DRA is ~1µm. If this could be reduced to approximately 0.2µm (Nilsson et al, 1991) then it might be a useful technique for imaging luminescence from nanostructures, which would be a useful addition to the characterisation process.

One of the most effective ways of counteracting the low signal levels emanating from nanostructures is to record a scan hundreds of times and add the results together. By far the most suitable apparatus for this is the FFT spectrometer based system. Its ability to record hundreds of spectra within a few minutes with a very high spectral resolution is extremely valuable.

Bearing in mind the lack of a suitable laser excitation source for performing PLE or absorption measurements on InGaAs/InP material, this apparatus stands out as being the best candidate available for obtaining absorption measurements.

The simplicity of the PL experiments, the very strong signal levels produced (compared with other techniques), and the information it furnishes on the lowest energy state are sufficient to ensure that it is a very important experiment which should not be overlooked in sample characterisation. However, the PLE experiment - or failing that an absorption experiment - yields the most information and so it is the most desirable experiment to perform so that a sample can be characterised as accurately as possible.

References

Arnot H E G, 1990 PhD Thesis, University of Glasgow

Bebb H B and Williams E W, 1973 Semiconductors and Semimetals Vol 8 Chapter 4

Collins A T and Jeffries T, 1982 J Phys E: Sci Instrum Vol 15 p712

Hamilton B, Clarke G, Rogers D, Wood D, Walling R H, Davies J I and Scott M D, 1988 Semic Sci Technol Vol 3 p1067-1072

Handbook of Physics and Chemistry, 1982 63rd Ed p F-109

Leitch W E, 1993 PhD Thesis, University of Glasgow

Nilsson S, Gustafsson A, Montelius L, Semu A, Georgsson K and Samuelson L, 1991 Proc 7th Int Conf on Microscopy of Semiconductors

Pritchard R, 1992 accepted for publication Semic Sci Technol

Rodden W S O, 1993 PhD Thesis, University of Glasgow

Rogers D C, Wood D R and Ambridge T, 1991 B T Technol J 9 (4) p36-42

Samuelson L, Georgsson K, Gustafsson A, Maximov I, Montelius L, Nilsson S, Seifert W and Semu A, 1992 Proc SPIE Symposium on Compound Semiconductor Physics and Devices vol 1676 154-160

Sotomayor Torres C M, Leitch W E, Lootens D, Wang P D, Williams G M, Thoms S, Wallace H , Van Daele P, Cullis A G, Stanley C R, Demeester P and Beaumont S P, 1992 Proc Int Symposium on Nanostructures and Mesoscopic Systems, Santa Fe, USA.

Williams G M, Cullis A G, Sotomayor Torres C M, Thoms S, Beaumont S P, Stanley C R, Lootens D and Van Daele P, 1991 Proc Microscopy of Semiconductor Materials Conf, Oxford. Inst Phys Conf Ser No 117 p695-698.

Chapter 6
Luminescence spectroscopy of quantum wires and dots

6.1 Sample fabrication considerations

Photoluminescence experiments were performed on samples which were fabricated by three different methods. Originally, the only available machines were one electron beam machine and one dry etching machine. However, during the period of this research another two, better electron beam machines became available, and another dry etch machine was purchased.

The first of these methods used the PSEM500 electron beam machine and the ET340 dry etch machine; the second used the Jeol 100CXII electron beam machine and the μP80 dry etch machine; and the third used the EBPG HR5 (the Beamwriter) electron beam machine and the μP80 dry etch machine. The results of these experiments will be presented in the following sections.

The data presented in this chapter will largely reflect the chronological order in which the data was recorded. The reason for this is not solely to produce a log of the research work performed but also to reflect the progress made towards smaller device dimensions with the availability of better equipment. One advantage of presenting the data in this form is that it highlights the role the fabrication equipment plays in introducing damage while patterning small structures. Another reason for presenting the data in this format is that some of the later (chronologically) samples (numbers 6 to 10 in table 6.1) had both wires and dots patterned on them, and so to dissociate the wire and dot sections would artificially separate data which should give complementary information which aids in interpreting the PL spectra.

The earliest samples which were produced during this research were fabricated using the PSEM500 electron beam microscope and the ET340 reactive ion etch machine. This

combination was used to fabricate dots down to 60nm in diameter. Although smaller dot sizes could have been written using the PSEM500 (perhaps down to 40nm) no signal could be obtained from the 60nm dots, presumably because of the ET340 introducing damage during etching, and so there was no point in pursuing structure sizes smaller than 60nm with this apparatus.

The second set of fabrication equipment used was the Jeol 100CXII and the μP80 RIE machine. This pair was more promising for fabricating small structures. The Jeol was capable of producing minute linewidths (down to 15nm) over small areas, but it was unsuitable for preparing samples with three or four arrays spaced approximately 1mm apart. The success in patterning samples using this machine (for four arrays of 30nm wide wires or dots) was very low - less than 10%. As a result of this inefficiency, fabrication efforts were switched to the third lithography machine.

The EBPG HR5 (Beamwriter) became available for use in the last few months of this research. The combination of high resolution (25nm wide wires could be written) and consistency of focus across the sample meant that when the Beamwriter was combined with the μP80 it was ideal for this research. Only 5 samples were patterned with the Beamwriter but every one of them worked - a yield of 100%.

6.1.1 Samples referenced in this thesis

Table 6.1 gives a list of the samples used in this thesis with a description of the quantum well type and thickness, the typical 5K PL FWHM of the quantum well, the origin of the samples, the method used to grow the samples, the lithography and dry etch machines which were used to pattern the samples and any additional fabrication steps such as annealing or wet etching of the quantum structures.

Sample No.	Quantum well type, thickness, and 5K PL FWHM	Origin, name and material growth process	Fabrication details	Additional fabrication steps
1	SQW 8nm 16meV	Thomson-CSF B556 LP-MOVPE	PSEM500 & ET340	-
2	SQW 8nm 16meV	Thomson-CSF B556 LP-MOVPE	JEOL & μP80	-
3	SQW 5nm 25meV	Thomson-CSF B555 LP-MOVPE	JEOL & μP80	-
4	SQW 8nm 16meV	Thomson-CSF B556 LP-MOVPE	JEOL & μP80	-
5	SQW 5nm 14 meV	Sheffield University PMB297 Solid Source MBE	JEOL & μP80	-
6	SQW 7nm 9 meV	Aachen RWTH 2311 MOVPE	EBPG HR5 & μP80	-
7	SQW 7nm 9 meV	Aachen RWTH 2311 MOVPE	EBPG HR5 & μP80	Annealing
8	SQW 7nm 9 meV	Aachen RWTH 2311 MOVPE	EBPG HR5 & μP80	Annealing and Wet etching
9	SQW 7nm 9 meV	Aachen RWTH 2311 MOVPE	EBPG HR5 & μP80	Wet etching only
10	SQW 7nm 9 meV	Aachen RWTH 2311 MOVPE	EBPG HR5 & μP80	-

Table 6.1 Samples used in this research work. The FWHM was measured from the 5K PL spectra of the as-grown samples

6.1.2 Guide to nomenclature of wires and dots

In order to give titles to the sections and the subsections in this chapter which convey information to the reader, the identification of samples by a description of structure type and size will be used rather than just using the sample number.

6.2 Dots from 600 to 60nm fabricated using the PSEM500 and ET340

A single quantum well sample (sample no.1) was patterned with a variety of dot sizes, the largest being 600nm and the smallest 60nm in diameter; in addition to these dots several mesas (areas which were masked during etching) were included for comparison. Figure 6.1 shows a diagram of the structure of the material which was used (sample B556) showing the individual layer thicknesses. The sample was grown at the Thomson-CSF laboratory by the LP-MOVPE growth technique.

20nm InP
8nm InGaAs
200nm InP
Fe doped InP

Figure 6.1 B556 sample structure

The sample used had to be a single quantum well sample for several reasons. When multiple quantum well samples are used then the etch depth must be greater than for shallow, single quantum wells in order to etch through all of the quantum wells. If any wells are left which are not etched through then they will give a huge luminescence signal which will swamp the weak signal from the higher lying quantum wells. As the etch time increases the length of time that the topmost quantum well (usually the most important quantum well for observing confinement) is exposed to the rf discharge increases, and hence it sustains a greater amount of damage due to the incidence of the accelerated ions in the plasma. In order to minimise the damage induced by dry etching short etch times are used, which in turn requires the use of single quantum wells which are near the top of the sample surface.

6.2.1 PL spectra from 600 to 60nm sized dots

The PL spectra recorded from the different arrays patterned on sample no. 1 are shown in figures 6.2 to 6.4. The three different PL spectra labelled figures 6.2, 6.3, and 6.4 correspond to the spectra obtained from a mesa, the 300nm diameter dot array, and the mesa and 100nm diameter dot spectra superimposed on the same diagram, respectively. The spectrum recorded from the 600nm diameter dot array is not shown because it is virtually identical to the mesa spectrum of figure 6.2. Although 60nm diameter dots were successfully patterned onto this sample, no PL signal could be detected from these dots.

The arrays of dots and mesas were excited with the 488nm line of an Argon ion laser. The spectra of figures 6.2 to 6.4 were all recorded under the same conditions. The laser power was kept at a constant value of 2mW and the spectrometer entrance and exit slits were set at a constant width of 1mm. Although this value of slit width seems quite large it was necessary in order to obtain a signal from the smallest dots. The major disadvantage associated with wide slits is a loss of resolution: but since the quantum well peak is comparatively broad (see table 6.1) for the InGaAs samples which were used in this research, resolution is not of the utmost importance.

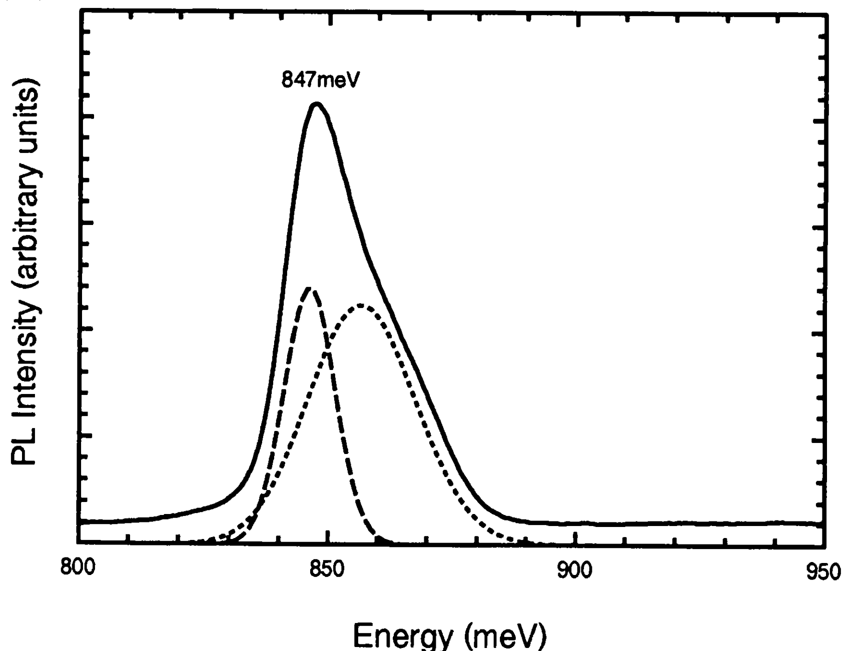

Figure 6.2 PL spectrum obtained from the mesa on sample no.1, which was an 8nm thick SQW. Excitation was by 2mW of the 488nm line of an Ar^+ laser. The sample was maintained at 5K during the PL measurements.

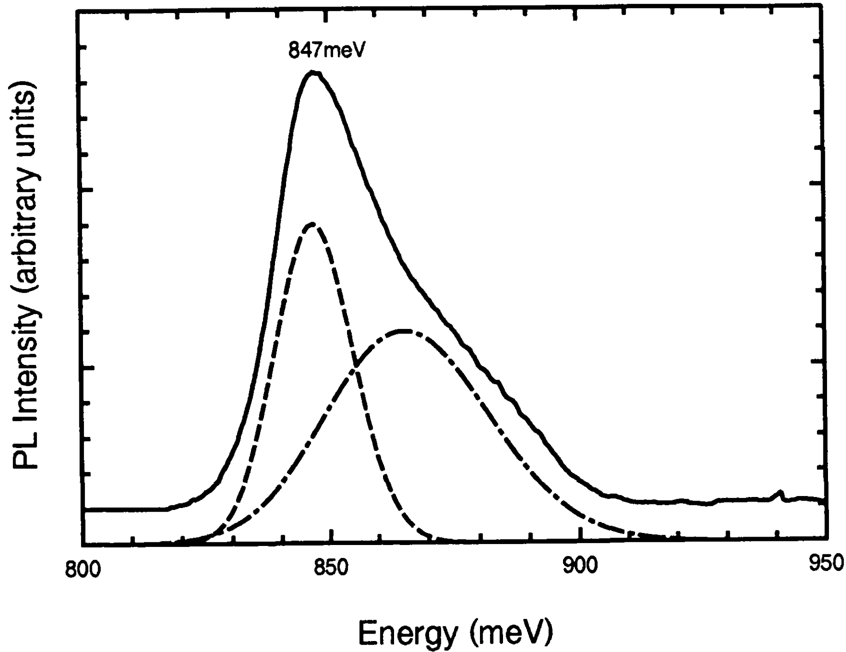

Figure 6.3 PL spectrum obtained from a 300nm wide dot array on sample no.1, which was an 8nm thick SQW. Excitation was by 2mW of the 488nm line of an Ar^+ laser. The sample was maintained at 5K during the PL measurements.

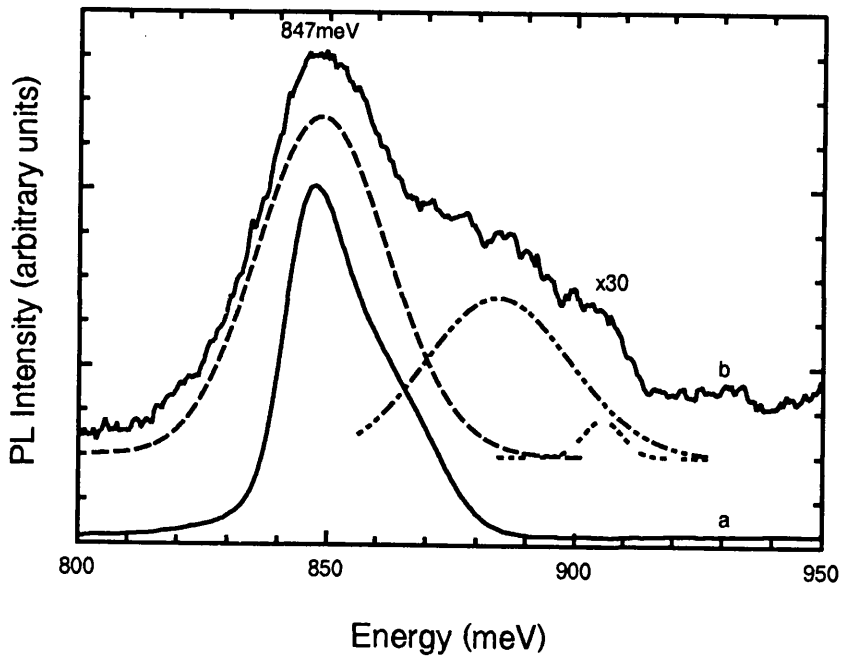

Figure 6.4 PL spectrum obtained from both the mesa (a) and 100nm wide dot array (b) on sample no.1, which was an 8nm thick SQW. Excitation was by 2mW of the 488nm line of an Ar^+ laser. The sample was maintained at 5K during the PL measurements.

On comparing the three spectra shown in figures 6.2 to 6.4, the following details are worthy of consideration. The spectrum obtained from the mesa area (figure 6.2) shows a peak at 847meV and a high energy tail. Figure 6.3 is the spectrum obtained from an array of dots each one 300nm wide. The peak position is not shifted with respect to the mesa but the high energy tail is more pronounced and it extends to higher values of energy than the tail on the mesa. The spectrum of an array of 100nm wide dots (shown in figure 6.4b) reveals a broadened peak/knee at higher energies. This high energy knee is even more pronounced than in either the mesa or 300nm dot spectrum (figures 6.2 & 6.3 respectively) and it extends to even higher energies. Indeed, the high energy hump has assumed the appearance of additional peaks in the transition from mesa to 100nm wide dot structures. In addition to the high energy hump/peaks there is also some broadening of the main peak to lower energies, although this is not nearly as pronounced as the high energy broadening.

The spectra shown in figures 6.2 to 6.4 were deconvoluted using a least-squares approximation (see Appendix B). Two gaussian peaks were used to approximate each of the curves, the optimum values of which are given in table 6.2. The relative peak intensity relates the intensity of the gaussian peak to the intensity of the main peak on the original figure.

Figure no.	Gaussian no.	Peak position (meV)	FWHM (meV)	Relative peak intensity (a.u.)
6.2	1 (e, A°)	846	12	0.6
	2 BE	856	26	0.6
6.3	1 (e, A°)	847	19	0.8
	2 BE	865	39	0.5
6.4	1 (e, A°)	847	21	0.3
	2 BE	866	63	0.3

Table 6.2 Two-Gaussian approximation parameters for figures 6.2 to 6.4 with possible interpretations of emission origin

The two-gaussian approximation seems to work reasonably well for the comparatively simple spectra of figures 6.2 and 6.3. However, the spectra of figure 6.4 is too complicated to be treated by a two-gaussian approximation. There appears to be a small peak at 810meV in addition to the main peak at 849meV and any number of peaks between 860 and 910meV. Even with the these limitations in view, however, the two-gaussian approximation does shed some light on the shape of the spectra and origin of the emission processes.

Figure 6.5 shows the graph of the exciting laser power against the integrated emission intensity for material type B556 (as used in sample number 1). The graph of figure 6.5 was fitted with the curve $y = 0.49\ x^{0.96}$, which indicates that the recombination is intrinsic in nature.

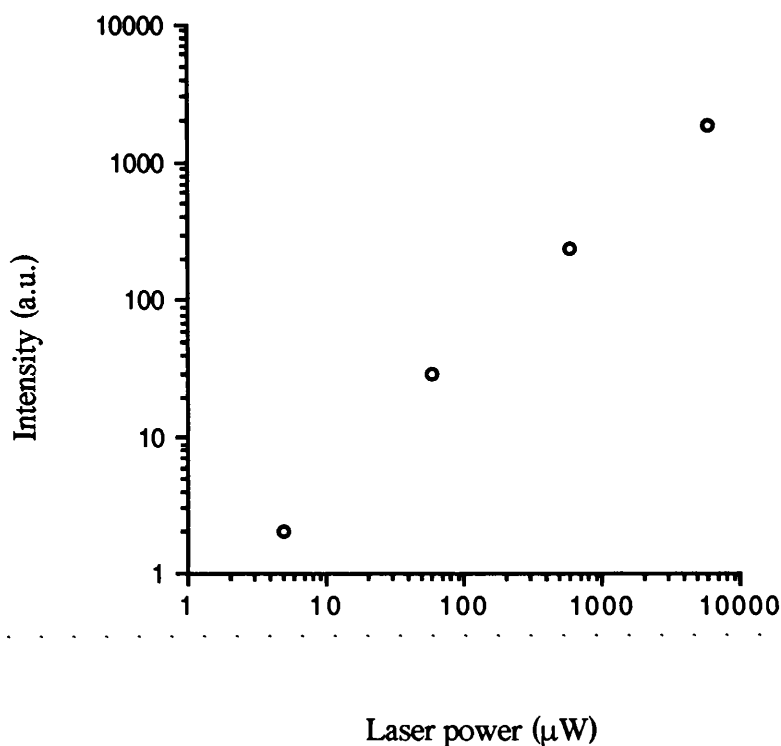

Laser power (μW)

Figure 6.5 Laser power versus integrated emission intensity for sample no.1

Figure 6.6 shows the PL spectra of B556 material recorded at three different sample temperatures.

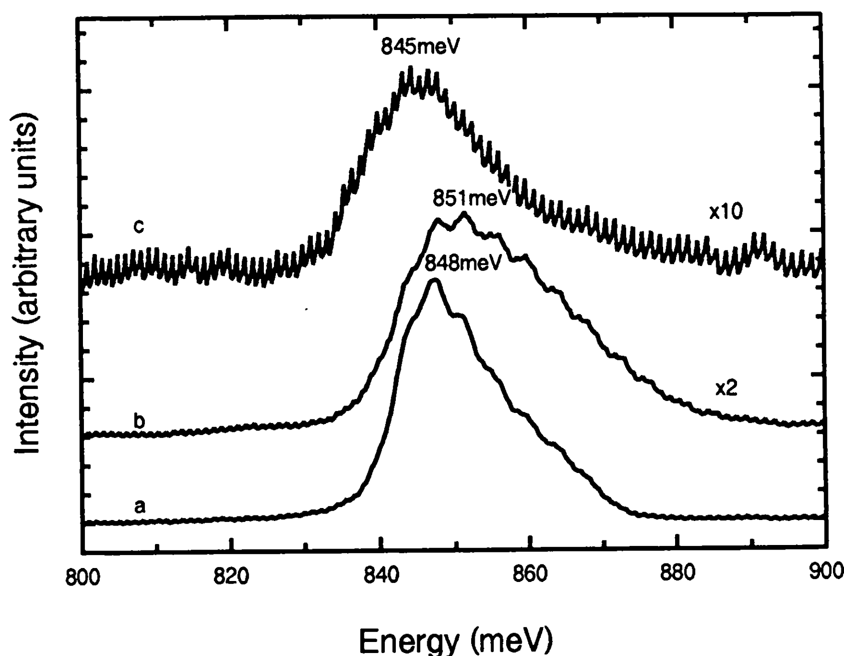

Figure 6.6 PL spectra of B556 material recorded at three different sample temperatures. Curve c corresponds to 120K, curve b to 50K and curve a to 10K. The 488nm line of an Ar^+ laser was used to excite the sample, an 8nm thick SQW. Cuves a and b were excited using 50μW and curve c was excited by 350μW

Deconvolution of the mesa spectrum produces one narrow peak at 846meV and a further peak of similar intensity but a factor of two broader at 856meV. The peak at 846meV is attributed to a free-to-bound transition and the peak at 856meV to a bound exciton. The exciton is probably bound to a donor and/or an alloy fluctuation potential.

The 300nm wide dots spectrum, when deconvoluted, shows that both peaks have broadened by ~50% and the peak at 856meV has moved to higher energies by ~10meV compared with the mesa.

The 100nm wide dots spectrum shows broadening to both high and low energies. Perhaps the low energy broadening is best accounted for by the effect of impurities introduced during processing (Patillon et al, 1990). RIE is carried out using carbon and hydrogen (CH_4/H_2) which are easily incorporated into semiconductors. The two-gaussian deconvolution shows one peak at 847meV with a FWHM only slightly larger than that of the 300nm wide dots. The other peak is at 866meV, which is almost the same position as for the 300nm wide dots, but with a FWHM approximately 50% larger than the 300nm dots. It is interesting to note that the peak intensities are approximately equal. This means that the integrated luminescence signal emanating from the high energy peak (although in this approximation it is one peak, in reality it is probably the result of two or three peaks) is much greater than that

emanating from the main recombination energy (because of the differences in FWHM of the high and low energy peaks).

Initially the high energy peaks on the spectrum of figure 6.4 were thought to arise from some form of "bottlenecking" (Benisty et al, 1992). This theory states that with increasing confinement (decreasing size) the 2D allowed energy levels split into a series of 1 and 0-D levels which are separated by only a few meV in energy. The regime for the onset of this effect is the exciton centre-of-mass confinement regime (100-250nm lateral sizes for the case of InGaAs based quantum well structures).

In this regime, scattering with optical phonons is seriously inhibited, leaving acoustic phonons to participate in the relaxation process. Acoustic phonon scattering times increase by orders of magnitude in going from 2 to 0-D (Bockelmann and Bastard, 1990) so the net result is that there will be a large number of carriers "waiting" at higher energy levels and causing a "bottleneck" at these higher energy levels. If this "bottleneck" is severe enough (if the upper energy levels begin to fill up with electrons) then there will be recombination from higher energy levels which would be manifest even in PL measurements by emission at energies higher than the main exciton recombination energy.

However, two objections could be raised regarding the validity of this theory for interpreting the data of figure 6.4. The first is that the mesa and 300nm wide wire array both show a high energy tail. It could be argued that the high energy peaks of figure 6.4 are present in both the mesa and 300nm dots spectra but they are obscured by the strong signal from the recombination at 847meV, whereas this signal from the 100nm dots (847meV) is so weak (comparatively) that the high energy tail has a greater effect.

The second objection is that this model seems inapplicable for this data because the spectrum of figure 6.4 shows no blue-shift (which is the characteristic of quantum confinement effects) of the main exciton peak. This model is only valid for structures which are subjected to some form of quantum confinement (without quantum confinement the energy levels would not separate into a series of levels and so no "bottle-necking" would occur).

The second objection is the weaker of the two. Although the bottleneck model does require some form of quantum confinement, this does not mean that the confinement must be observable in the PL spectra. The separation of energy levels required for this effect occurs in the centre-of-mass confinement regime (lateral sizes of 100-250nm) and for structures of this size no blue shift of the main recombination peak is expected in this material type. It is possible that the 100nm dots patterned on sample no.1 do indeed confine electrons but due to

competing factors - such as an increased exciton binding energy - there is no clear blue-shift of the main peak in the PL spectrum.

It is interesting to note the appearance of a slight shoulder on the 300nm dots spectrum (figure 6.3) because these dots should be just above the limit of centre-of-mass confinement (~250nm). As this size (250nm) is only approximate it is possible that a slight bottleneck occurs in these dots. The proximity of the second emission peak (obtained by Gaussian deconvolution) in this spectrum (865meV) to that of figure 6.4b (866meV) would support this view.

The first objection is not satisfactory either. This is because the spectrum of figure 6.2, even when magnified, shows no evidence of any peaks in the region of 900meV.

It could be said that these peaks are impurity related. This would explain why the tail gets more pronounced with the move from mesa to 300nm dots to 100nm dots. As the dot size decreases the surface area to volume ratio increases and so surface effects (such as impurity incorporation) become more pronounced.

This explanation, though plausible, is very unlikely. Incorporation of impurities into the quantum well material should give rise to peaks at lower - not higher - energies. It might be said that the high energy peaks could be due to deep level traps in the barrier material (InP); but it seems unlikely that the luminescence from these traps should coincide with that of the well material.

Another possibility is that there is some form of mild impurity induced disorder which would give rise to broader luminescence emission by producing areas of GaInAs with P, i.e. GaInAsP, at the interfaces of the GaInAs and InP. Thus, emission from the GaInAs quantum well would be detected but so would the emission from the higher energy GaInAsP at the interface.

6.2.2 Integrated PL intensities of 600 to 60nm sized dots

Notwithstanding the care which must be exercised in interpreting data obtained from PL intensities of wires and dots, it is still a useful exercise and one that can yield important information regarding fabrication considerations. The normalised values of integrated luminescence intensities (i.e. corrected for fill-factor) which were recorded from the patterned arrays on sample no.1 are shown in table 6.3. Data from 600nm wide dots is included although the spectrum was not shown because it was similar to the mesa spectrum.

Structure Type	Integrated Intensity (arbitrary units)	Fill-factor (%)	Corrected Integrated Intensity (a.u.)
Mesa	40	100	1
600nm dots	22	7	8
300nm dots	17	4	11
100nm dots	2.8	2.8	2.5

Table 6.3 Integrated PL intensities for sample no.1

The integrated intensity value of 11 for the 300nm dots is unlikely to be indicative of enhanced luminescence. It is far more likely to be the result of the well capturing carriers generated in the InP barrier layer surrounding the quantum well layer. To be sure of an enhancement in the luminescence intensity it is essential to do experiments using a laser of energy sufficient to excite only the well, which was not available during this project.

What the statistics presented in table 6.3 do show (when comparing the 300nm dots with the 100nm dots) is that there is a sizeable decrease in integrated PL intensity accompanying the move to smaller dot sizes. The cause of this will be considered in greater detail in sections 6.3.1.1 and 6.3.4.

6.2.3 Discussion of data obtained from 600 to 60nm dots

The study of damage introduced by the ET340 compared with that introduced by the μP80 RIE machine detailed in chapter 4 of this thesis revealed that the ET340 seemed to introduce more damage than the μP80.

In addition to this, the unsuitability of the ET340 based process for producing small structures (less than 60nm) required the use of a more innocuous fabrication process.

The dramatic reduction in PL intensity exhibited by the medium sized dots (100nm diameter) introduced a further complication, namely, the possibility that quantum dots could be fabricated which confine the carriers but which produce a PL signal too low to detect.

Since the poor emission could arise from RIE damage (which would have a greater effect in smaller dots) and/or the bottleneck phenomenon, new avenues of investigation were required in order to clarify the situation. Consequently, the focus of this work shifted to quantum wires because they usually have larger fill-factors and so, hopefully, stronger luminescence signals.

6.3 Wires down to 30nm fabricated using the Jeol and μP80 system

Initially, experiments were performed in order to shed light on the relationship between the emission intensity of wires compared with dots. This would show whether stronger signals came from wires or dots and hence either justify or disparage the shift of attention from dots to wires.

6.3.1 170 and 100nm wires - sample nos. 2 & 3

It was decided to use medium sized wires as a reference for these experiments to ensure that the signals obtained would be large enough to allow accurate comparisons to be made.

6.3.1.1 Determination of PL intensity variation with wire length

Photoluminescence experiments based on the GaAs/AlGaAs system suggested that with changes in the length of quantum wires there were also changes in the luminescence efficiency (Leitch et al, 1992). In particular, it was reported that dots luminesced more efficiently than wires and it was suggested that this was because there is a high probability of an exciton encountering a trap as it diffuses along a wire. Such exciton diffusion processes would not apply to very small dots.

In order to test whether or not this model applied to the InGaAs/InP system the following experiment was performed. Two samples were patterned with wires, the first of these samples (sample no. 2, L_z=8nm) was B556 which was described earlier (see section 6.2) and the structure of this sample is given in figure 6.1. The second sample (sample no. 3, L_z=5nm) was also a single quantum well sample (B555) grown by LP-MOVPE at Thomson-CSF, details of this sample structure are given in figure 6.7.

20nm InP
5nm InGaAs
200nm InP
Fe doped InP

Figure 6.7 Structure of sample No.3 (B555)

Each sample was patterned with six different wire arrays. For sample no. 3 each array was composed of 100nm wide wires and for sample no. 2 each array was composed of 170nm wide wires. Thus, each sample had six arrays of equal wire width. This experiment differed from the usual PL experiments in that the difference between each array was in the length of the wires, not in the wire width. Each array covered an area of approximately 75μm by 200μm. The longest wires on each sample stretched the full width of the array, which was 75μm. The next array had wires of approximately 37μm long, the next array had wires approximately 15μm long, the next 5μm long, the next 1μm long and the final array of wires (although by this stage they were more like dots) was 200nm wide for sample no. 2 and 100nm wide for sample no. 3. Thus, in each sample there were arrays which covered the transition from long wires to dots. The fill-factors of these arrays were calculated from micrographs taken from an Hitachi S-900 electron microscope and the integrated intensities of the PL spectra were calculated and then normalised by the appropriate fill-factor. The results of the PL experiments are shown in figures 6.8 and 6.9.

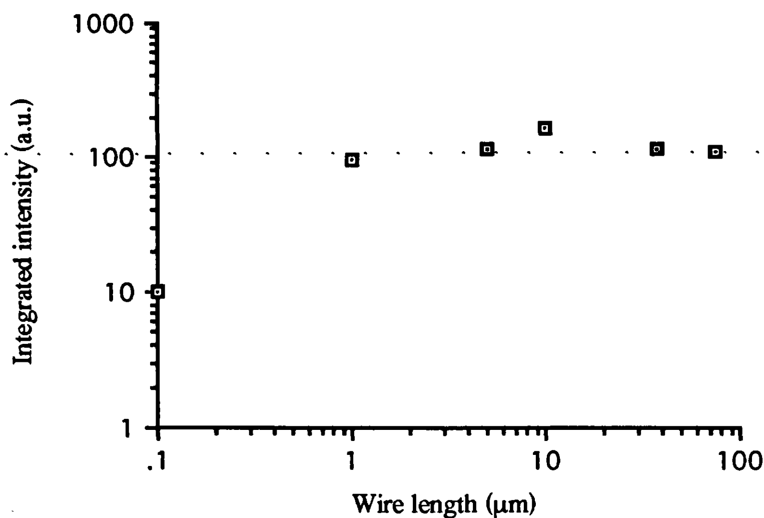

Figure 6.8 PL integrated intensity versus wire length for the 100nm wide wire arrays on sample no. 3.

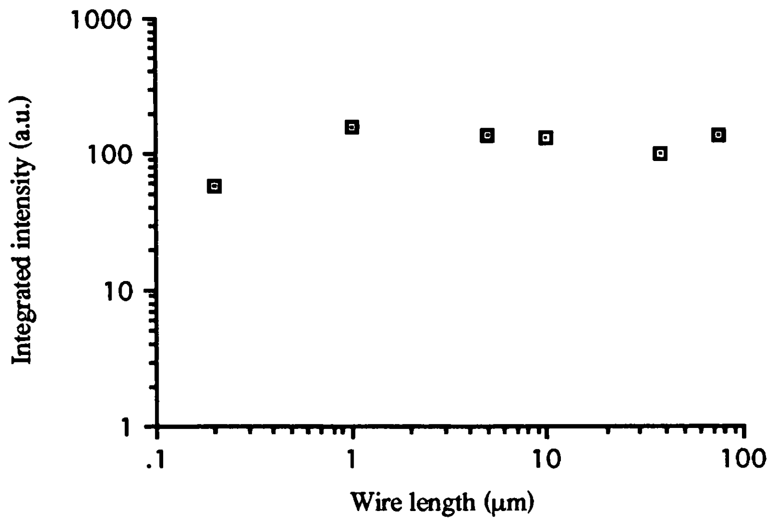

Figure 6.9 PL integrated intensity versus wire length for the 170nm wide wire arrays on sample no. 2.

Figures 6.8 and 6.9 show that for wires between 1μm and 75μm in length the luminescence intensity is virtually constant. Figure 6.9 shows that for wires (in reality they are dots) down to 200nm long the intensity is still quite high, almost 60% of that of the long wires. Figure 6.8 also shows that the smallest wires (dots) have a PL intensity an order of magnitude smaller than that of the long wires.

6.3.1.2 Discussion of PL intensity variation with wire length

From these results it seems reasonable to suggest that the length of a wire (as long as it is greater than 1μm) makes no appreciable difference to the PL intensity. In both of the above cases the luminescence from the "dot-like" structures is noticeably lower than that from the wires.

The present set of data differs substantially from that of GaAs/AlGaAs wires (Leitch et al, 1992).

The main explanation given by Leitch et al (1992) for the increase in luminescence with decreasing wire length was the increased probability of having traps in a long wire. As a result of the interface smoothness (the MBE grown GaAs/AlGaAs was of very high quality) the excitons could diffuse along the wire and become trapped, this would result in non-radiative recombination and hence lower luminescence efficiency.

However, the InGaAs/InP material which was used in this research was not of comparable quality with the GaAs/AlGaAs material. It is very unlikely that the interfaces are

smooth and so the possibility of exciton diffusion is much lower, it is more likely that the excitons will be localised in the plane of the well by a combination of alloy fluctuation potentials and quantum well interface terraces.

6.3.2 50 to 30nm wires - sample no. 4

A single quantum well sample - for reasons detailed in section 6.2 - was patterned with wires and mesas, and is called sample no. 4 for identification purposes. Again the sample used was B556, detailed in section 6.2.

Seven arrays were patterned onto the sample, three mesa areas and four wire arrays. The pattern layout was similar to that given in figure 3.12, the difference being the absence in this sample of the large dots/wires in figure 3.12. Of the four wire arrays, two arrays had lateral dimensions of approximately 50nm and two had lateral dimensions of approximately 30nm. Ascertaining the size of the wires was not a trivial matter despite having access to a very high resolution electron beam microscope (an Hitachi S-900). This was because there was polymer build-up on the mask during dry etching which gives the impression that the wires are thicker than they actually are. Another problem is that small structures - and particularly the polymer - swell on exposure to a high energy electron beam, such as the one present in a scanning electron microscope (SEM). Presumably this is due to the influence of the electron beams.

Figure 6.10 shows a micrograph of one of the arrays of wires which has a nominal width of 30nm, but which is perhaps as narrow as 15nm (careful examination of the micrograph reveals a narrow line within the "main" wire which could be the true semiconductor wire width, the rest being polymer from the etching stage).

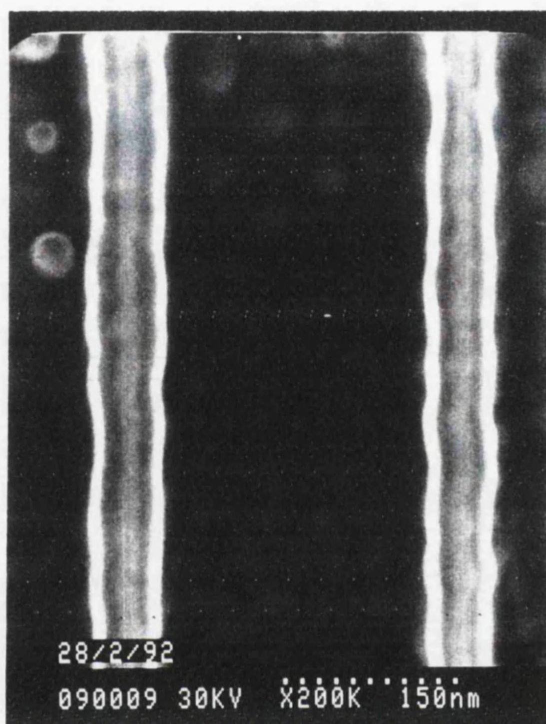

Figure 6.10 Micrograph of 30nm (possibly 15nm) wires

The arrays of wires and mesas were approximately 400μm square and were separated by 500μm. The large array size was chosen to aid in locating the patterned arrays when doing PL experiments; however, using such a large array size (large compared with the typical laser spot diameter of ~70μm) had several ramifications. The large array sizes meant that the electron beam lithography machine took over half an hour to write each array and this long time annexed to the comparatively large distance between the starting and finishing sites on the one array (~300μm) gave rise to the possibility of a focus shift over the array (the depth of focus on the Jeol is of the order of 1μm). This means that one end of the array could have wires which were slightly narrower than the other end.

The effect of these variations on PL spectra from such an array would be a signal which is dependent on laser spot position, i.e. different spectra could be obtained from the one array. This effect can be seen by comparing figures 6.11 and 6.12, which are spectra recorded from different positions on the same wire array.

Figures 6.11 to 6.15 show some of the PL spectra obtained from these wire arrays. The spectrometer entrance and exit slits were set at a constant value of 1mm for these experiments and the excitation source was the 488nm line of an Argon ion laser.

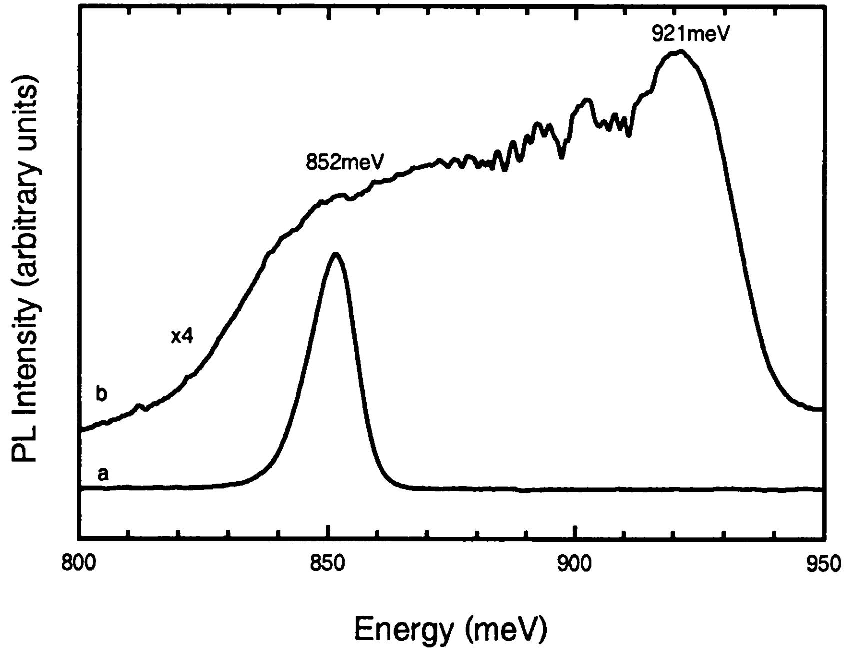

Figure 6.11 PL spectra of a 50nm wide wire array (curve b) and a mesa array (curve a) on sample no. 4, which is an 8nm thick SQW sample. Both spectra were recorded with the sample cooled to 5K. The 488nm line of an Ar^+ laser was used with a power of 180μW for the wire array and 20μW for the mesa array. The region from 880meV to 910meV is disrupted by water absorption

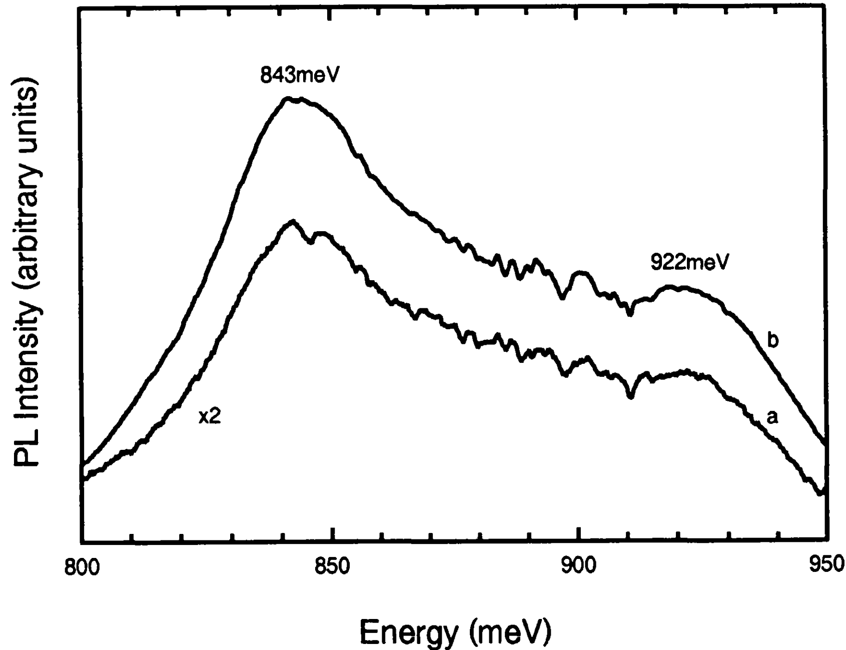

Figure 6.12 PL spectra of the same 50nm wide wire array on sample no. 4, an 8nm thick SQW sample, as was probed in figure 6.11. The 488nm line of an Ar^+ laser was used to excite the sample, but this time a different location on the array was probed to that excited in figure 6.11. The sample was cooled to 5K. Curve (b) resulted from 2.6mW of laser power, curve (a) from 0.6mW of laser power.

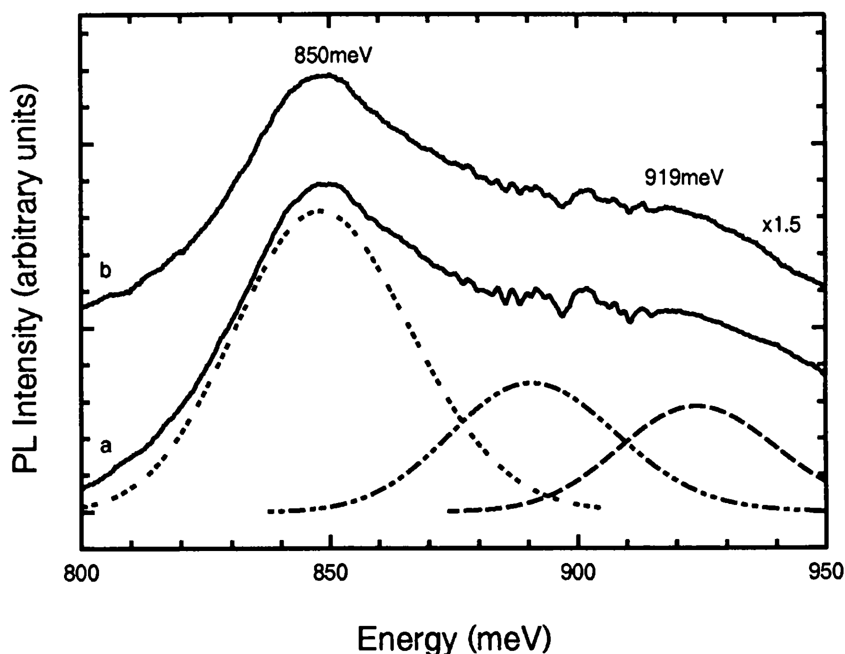

Figure 6.13 PL spectra of a 30nm wide wire array on sample no. 4, an 8nm thick SQW sample. The 488nm line of an Ar^+ laser was used to excite the sample which was cooled to 5K. Two PL spectra were obtained from the wire array (the laser spot was in the same position each time). Curve (a) corresponds to 8mW laser excitation, curve (b) to 2mW excitation.

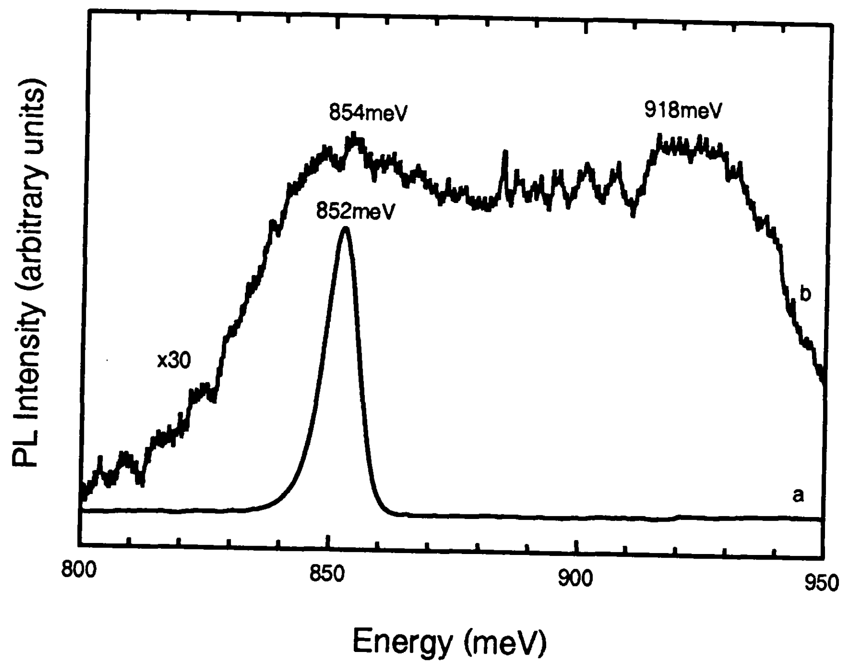

Figure 6.14 PL spectra from the second 50nm wide wire array (different to figures 6.11 and 6.12) and a mesa array on sample no.4, an 8nm thick SQW sample. The 488nm line of an Ar^{+} laser was used to excite the sample which was cooled to 5K. Curve (b) resulted from 2.4mW of laser power exciting the 50nm wide wires, curve (a) resulted from 10μW of laser excitation of a neighbouring mesa array.

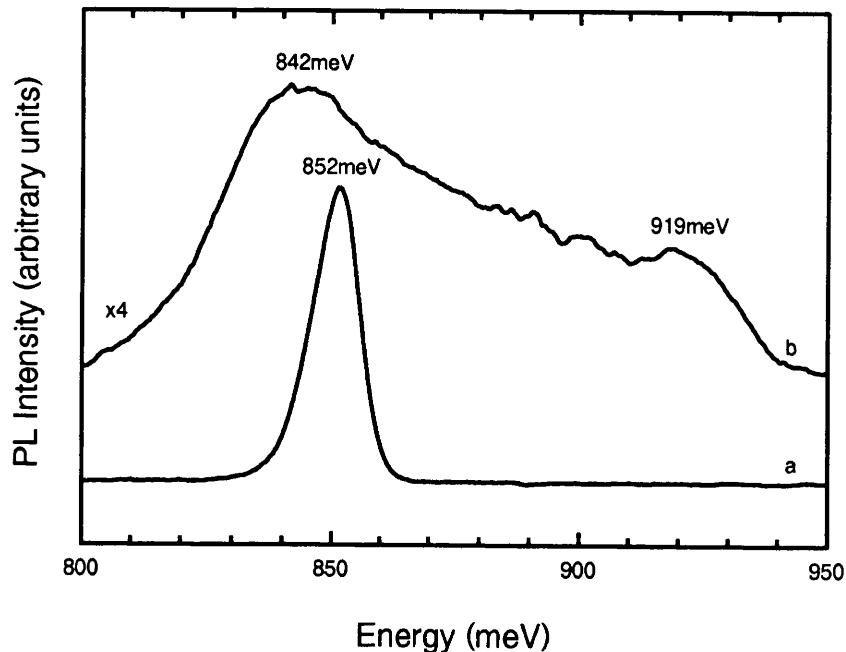

Figure 6.15 PL spectra of the second 50nm wide wire array and a mesa array on sample no. 4, an 8nm thick SQW sample. The 488nm line of an Ar^+ laser was used to excite a different part of the wire array to that excited in figure 6.14. The temperature of the sample was maintained at 5K while the measurements were being recorded. Curve (b) corresponds to 100μW of laser power, curve (a) to 20μW of laser power exciting a neighbouring mesa area.

6.3.3 Discussion of PL data obtained from sample no.4

Initially, an overview will be given of all the data obtained from this sample before addressing any particular issue raised by one of the figures.

Even a glance at figure 6.11 reveals that spectrum (b) is very unusual when compared with many quantum wire and dot spectra published by some other research groups (Izrael et al, 1991; Samuelson et al, 1992). However, similar spectra have been recorded from doped 2D-GaInAs/InP (Skolnick et al 1987) where the effect of free carriers has broadened the PL linewidth. In addition, some research groups have recorded similar spectra from wires and dots (see, for example, Adesida et al, 1992 and Patillon et al, 1990). The PL spectrum of quantum wires shown in figure 6.11 has a band of enormous width with multiple peaks to higher energies. Broadening of the PL emission after fabrication of such small structures is neither unusual nor unexpected. In this spectrum there are at least two - and probably more - peaks. There is also considerable broadening of the main peak to lower energies. This can be

accounted for by the presence of shallow impurities introduced during one of the fabrication stages - most likely the dry etch stage, as previously discussed in section 6.2.1.

The peak at 852meV is probably the E1-HH1 exciton peak. The most intense peak occurs 69meV higher in energy than the mesa peak. The nominal well width is 8nm. Using this width as a guide, theoretical calculations predict that the E1-HH1 peak should occur at ~869meV, which is higher than the recorded peak which occurs at 852meV. However, the 8nm well width is only a nominal figure, and in other growth techniques there has been a tendency to underestimate the layer thickness (see section 6.3.5). If the well width was closer to 10nm there would be very little discrepancy. If it is assumed that the well is ~10nm thick then the energy levels would be as shown in table 6.4. These values were obtained by solving the square well potential Schrödinger equation. The calculations assumed band offsets of 230meV and 380meV for the conduction and valence bands, respectively. The effective masses in the well were assumed to be 0.05 for the electron, 0.5 for the heavy-hole and 0.05 for the light-hole; and in the barrier these were assumed to be 0.08 for the electron, 0.6 for the heavy-hole and 0.12 for the light-hole.

Transition	Energy (meV)
E1-HH1	854
E1-HH2	872
E1-HH3	904
E1-LH1	884

Table 6.4 Theoretical energy level emissions for a 10nm thick well

The broad emission of figures 6.11 to 6.15 makes it very difficult to ascertain which transitions are involved in the emission process. All of the transitions listed in table 6.4 occur within the emission band of the spectra.

Once again, the bottleneck model seems to provide the only realistic interpretation of the large broad emission at high energies.

It is interesting to note the similarity between the spectra of figure 6.12 and figure 6.4b, even though a different dry etch machine was used in each case and one of the figures refers to the emission from dots (figure 6.4) the other to emission from wires (figure 6.12).

Comparing curve (b) of figure 6.11 with those in figure 6.12 yields the following information. The two curves of figure 6.12 have their main peak at 843meV with a smaller peak at 922meV, whereas figure 6.11 has its main peak at 921meV with smaller peaks at ~850meV. It is apparent from figure 6.12 that the increase in laser power had almost no effect on the shape of the spectrum, although the integrated intensity of the wires does change with power. There is a three-fold increase in integrated intensity corresponding to the

four-fold increase in laser power. Table 6.5 gives the values of peak intensity for the peaks of figures 6.11 and 6.12.

Figure no.	Peak position (meV)	Intensity (a.u.)	Power (mW)
Mesa 6.11a	920	0	0.02
50nm wires 6.11b	920	90	0.18
50nm wires 6.12a	920	20	0.60
50nm wires 6.12b	920	50	2.6
Mesa 6.11a	843 (e, A°)	220	0.02
50nm wires 6.11b	843 (e, A°)	50	0.18
50nm wires 6.12a	843 (e, A°)	45	0.60
50nm wires 6.12b	843 (e, A°)	125	2.6

Table 6.5 PL peak intensities of spectra from figures 6.11 and 6.12 and tentative assignments of emission origin.

It should be remembered that the spectrum recorded by excitation with 0.18mW was recorded at a different spot (although on the same array) to the spectra recorded by excitation with 0.6 and 2.6mW. It is interesting to note from table 6.5 that raising the excitation power from 0.6mW to 2.6mW causes a uniform increase in the intensity of both peaks, i.e. neither peak saturates at these excitation powers.

Figure 6.13 shows spectra which are almost identical to the spectra of figure 6.12. Table 6.6 shows the individual peak intensities from these spectra.

Figure no.	Peak position (meV)	Intensity (a.u.)	Power (mW)
6.13a	~920	20	2
6.13b	~920	50	8
6.13a	~850	45	2
6.13b	~850	85	8

Table 6.6 PL peak intensities of spectra from figure 6.13

Table 6.6 shows that there is a slightly smaller increase in the PL peak intensity of the 850meV peak than for the 920meV peak. This suggests that there might be saturation of the 850meV peak under even higher excitation powers.

Figure 6.15 is similar to the spectra of figures 6.12 and 6.13. It shows that the main emission from these wires occurs at energies lower than the main emission for the mesa area.

This phenomena is probably due to the presence of impurities introduced during etching. These spectra seem to indicate that the width of the wire (whether 30nm or 50nm) does not greatly influence the shape of the spectrum. An alternative suggestion is that the excitons are sensing only a very small region (probably due to alloy fluctuations) and so are relatively unaffected by the size of the wells.

All of the spectra shown in figures 6.11 to 6.15 were deconvoluted using a 3-Gaussian approximation. The results for the wire arrays were very similar, especially figures 6.12, 6.13 and 6.15. The data obtained from figure 6.13a is given in table 6.7 as an example.

Gaussian no.	Peak position (meV)	FWHM (meV)	Relative peak intensity (a.u.)
1	849	42	0.5
2	891	40	0.2
3	924	37	0.2

Table 6.7 Deconvolution of spectrum (a) on figure 6.13 using a 3 gaussian approximation

In table 6.7, the three gaussian peaks are very broad and are probably the result of several transitions. In particular, the first gaussian peak probably covers at least three transitions, one at approximately 846meV, another at 856meV (compare with table 6.2) and a third at approximately 817meV. This explains why the value of FWHM is so high (42meV).

The one spectrum which does appear to be different is that of figure 6.14. This spectrum shows what appears to be a plateau which has peaks at either end. The signal produced by these wires is only ~2% of that obtained from the wires whose spectra is given by figure 6.13b, which was excited by a similar laser power. Perhaps the reduced intensity could be accounted for by assuming that this array of wires was patterned on a slightly better part of the sample. This higher quality area would have fewer areas or interfaces of the quantum well to trap excitons, in addition to fewer potential fluctuations due to alloy disorder. This would allow electron-hole pairs to reach the surface more efficiently than in poorer quality areas and the PL intensity would be reduced.

In support of this hypothesis (that some areas of the quantum well are better than others) attention could be drawn to the fact that one of the mesas has a PL FWHM of 9meV (e.g. figure 6.14) whilst another mesa has a PL FWHM of 11meV (e.g. figure 6.15).

To summarise the data obtained from sample no.4, the following notes are worthy of consideration. All of these spectra are very similar. In fact they all conform to the one broad shape with a peak at the start (~850meV) and a peak at the end (~920meV). The peak positions are remarkably constant for the four arrays, and yet the wire widths are not all the same, they vary from 30 to 50nm between arrays; this fact poses an interesting question as to

the mechanisms which cause the PL emission. It seems likely that the emission is due to recombination between E1-HH2, E1-HH3 and E1-LH1 energy levels, i.e. some form of bottlenecking.

6.3.4 Very small wires - sample no.5

The next sample of interest was one in which the electron beam lithography process was incomplete. The intention was to produce a sample similar in design to sample no. 4, with four wire arrays and three mesa areas. As usual the mesa areas worked perfectly but only one of the wire arrays was patterned successfully. Inconsistency of wire width across a sample and uncertainty in an array being correctly exposed were risks associated with using the Jeol. However, the one wire array which worked was composed of wires which were between 15 and 20nm in width.

Unlike sample no.4, sample no.5 was an MBE grown single quantum well sample grown at Sheffield University. The structure of sample no. 5 is shown in figure 6.16.

26nm	InP
5nm	InGaAs
500nm	InP
Semi-insulating InP	

Figure 6.16 Structure of sample no.5, PMB297

The PL integrated intensity versus laser power was recorded for this sample, the result (not shown) was fitted with the curve $y = 7.63\ x^{0.98}$. The value of 0.98 indicates that the recombination in this sample is intrinsic in nature.

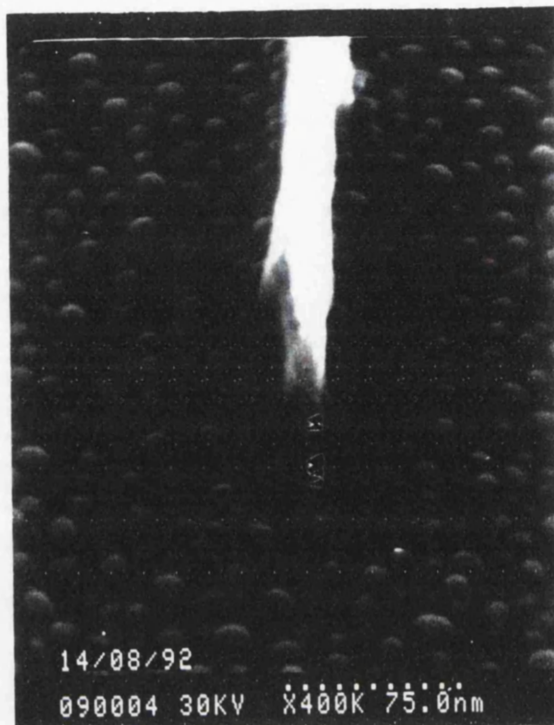

Figure 6.17 Micrograph of the 20nm wide wire array on sample no. 5

In figure 6.18 the upper curve corresponds to the signal emitted by the array of wires when excited by 6.2mW of laser power. The lower curve is the mesa emission produced by excitation with 14μW of laser power.

A number of PL spectra were taken at the same spot on the array of wires, varying the laser exciting power from 180μW to 6.2mW (see figure 6.19). In figure 6.20 three of these curves are plotted again to ease comparison between the spectra corresponding to the highest and lowest excitation powers.

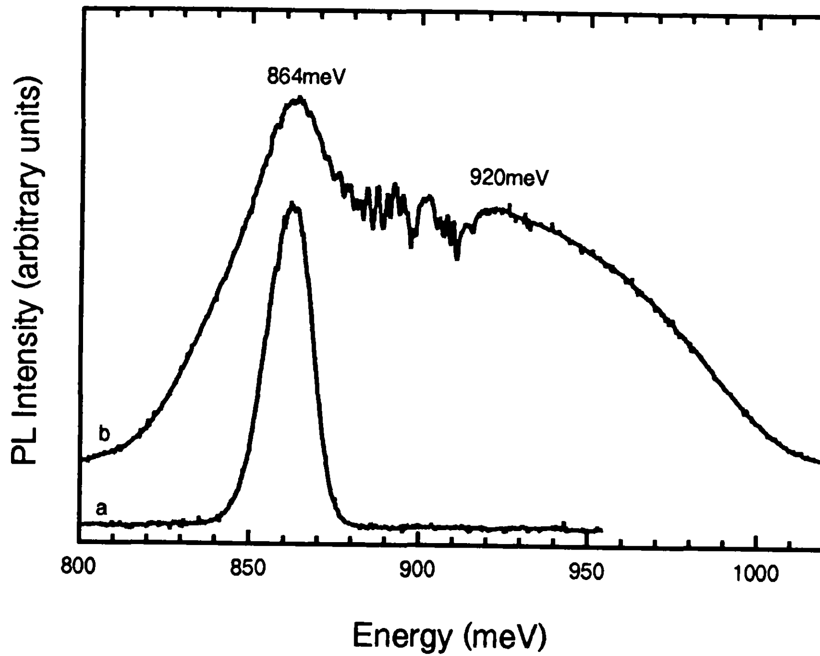

Figure 6.18 PL spectra of a 20nm wide wire array and a mesa area on sample no. 5, which is a 5nm thick SQW sample. The 488nm line of an Ar^+ laser was used to excite the sample which was cooled to 5K. The upper curve corresponds to excitation of the wires by 6.2mW of laser power, the lower curve to excitation of the mesa with 14μW.

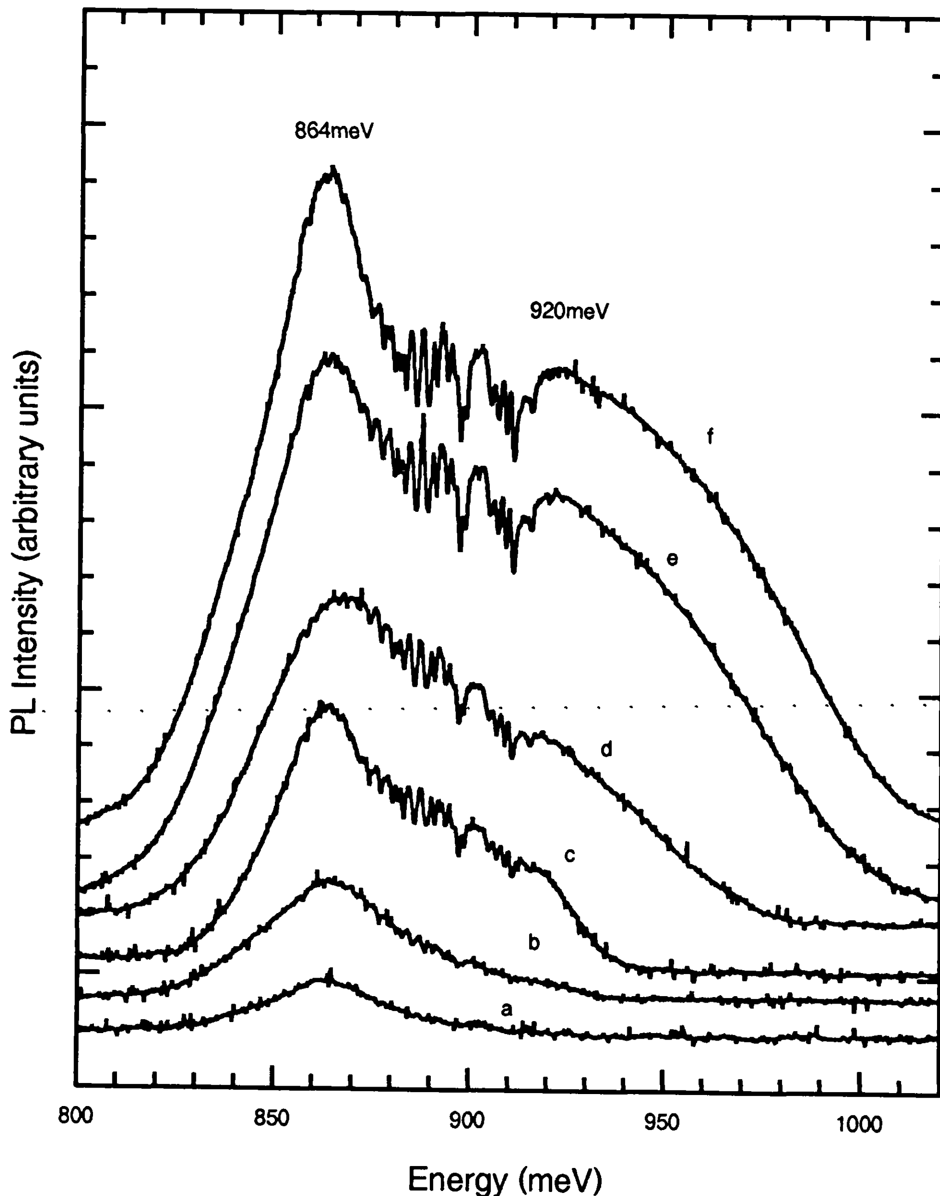

Figure 6.19 PL spectra of an array of 20nm wide wires on sample no. 5, a 5nm thick SQW sample, under different excitation intensities. The spectra were all recorded using the 488nm line of an Ar^+ laser, with the sample cooled to 5K. The spectra have been shifted in the vertical direction to clarify the figure and ease viewing; however, the relative intensities have not been adjusted. The laser excitation powers were (from the lowest curve to the highest curve) 180μW (a), 400μW (b), 700μW (c), 1.4mW (d), 3.3mW (e) and 6.2mW (f). The area from 880 to 920meV is disrupted by the effect of water absorption.

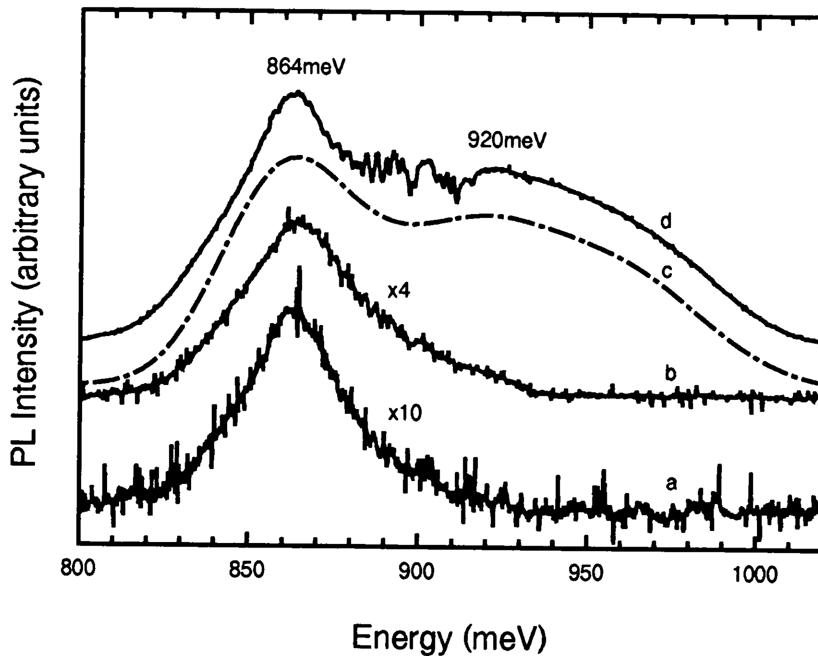

Figure 6.20 PL spectra obtained from the 20nm wide wires on sample no. 5, a 5nm thick SQW sample. The sample was cooled to 5K and probed with the 488nm line of an Ar^+ laser. The upper curve corresponds to 6.2mW of laser power (d), curve (c) is a theoretical gaussian lineshape fit to curve (d), curve (b) corresponds to 400μW excitation and the lowest curve (a) corresponds to 180μW.

6.3.5 Discussion of PL data obtained from sample no. 5

Quantum wires which have dimensions as small as 20nm - let alone 15nm - should produce sizeable energy up-shifts of the main peak on the PL spectra due to quantum confinement. For example, Izrael et al (1991) reported 30meV blue shifts for 15nm wide wires, and Notomi et al (1991) reported 10meV shifts for 20nm wide wires. The upper curve of figure 6.18 is remarkably similar to the curves shown in figures 6.12 and 6.13.

The effect of increasing the laser excitation power is shown in figure 6.19. The upper four curves clearly show two peaks, one at 864meV and another at ~920meV. Absorption experiments were performed at 4.2K on these samples (unpatterned samples not samples patterned with wire arrays) by J Camassel et al in Montpellier. The electron to heavy-hole transition (E1-HH1) at 860meV and the electron to light-hole transition (E1-LH1) at 895meV were resolved in an absorption experiment.

The electron to heavy-hole transition at 860meV seems to correspond quite well to the main peak of figures 6.18 to 6.20 which occurs at 864meV. This suggests that the recombination observed at 860meV in the PL spectrum of figure 6.19a is intrinsic. The

electron to light-hole transition at 895meV may well be present in the PL spectra of figure 6.19 but it would seem that there is another peak at ~920meV.

Camassel et al deduce from combined PL, PLE, absorption, reflectivity and x-ray scattering experiments that the actual well thickness is more likely to be nearer 9nm than the nominal value of 5nm. Using values for a well width of 9nm yields the theoretical energy level positions (using the same model as was used in section 6.3.3) given in table 6.8.

Transition	Position (meV)
E1-HH1	860
E1-HH2	883
E1-HH3	920
E1-HH4	972
E1-LH1	895

Table 6.8 Theoretical energy levels for a 9nm thick quantum well

The values of 860meV for E1-HH1 and 895meV for E1-LH1 correspond exactly to the values obtained from the absorption spectrum. In the light of these it would seem that the peak at 920meV is due to the E1-HH3 recombination.

Neither of the peaks shift much with increasing laser power, but it is interesting to note that there appears to be a threshold below which there is no emission corresponding to the E1-HH3 transition (compare spectra (b) and (c) on figure 6.19).

Spectrum (d) on figure 6.20 was deconvoluted using a three-Gaussian approximation program, the result is shown as spectrum (c) in that figure. The values obtained from this approximation are shown in table 6.9.

Gaussian no.	Peak position (meV)	FWHM (meV)	Relative peak intensity (a.u.)
1	860	46	0.85
2	919	68	0.65
3	967	53	0.28

Table 6.9 Deconvolution of spectrum (d) on figure 6.20 using a 3-Gaussian approximation

The three peaks produced by the deconvolution of spectrum (d) on figure 6.20 correspond very well to the calculated values for the E1-HH1, E1-HH3 and E1-HH4 energy level transitions. The presence of the spikes in the spectrum due to water absorption means

that the region of the light hole transition (895meV) can yield no information as to whether this transition is present in the spectra. The spectrum was fitted using only three gaussian peaks, it is highly probable that more than three transitions are responsible for the shape of the spectrum but these are masked by stronger signals. This would explain why the FWHM of the peaks given in figure 6.11 are so broad.

The ratio of the intensity of the main peak (at 864meV) to the second peak (at 920meV) is very high for the lowest excitation powers but gradually decreases with increasing laser power and seems to reach a near constant level of 1.5:1 for the two highest excitation spectra.

Figure 6.20 shows the spectra produced by the two lowest excitation powers expanded for comparison with the highest excitation power spectrum. Curve (b), corresponding to 400μW excitation, shows evidence of a shoulder which may be the beginnings of peaks at ~880meV (E1-HH2) and 895meV (E1-LH1). This behaviour matches the predictions of the bottleneck theory very well. As the laser power is increased more carriers are created and a bottleneck occurs resulting in emission from higher energy levels. The lowest curve (180μW excitation) is too noisy to allow any accurate statements to be made regarding a slight shoulder at approximately 920meV.

6.4 Wire and dot samples fabricated down to 20nm using the Beamwriter and μP80 system - sample nos. 6 to 10

The advent of the Beamwriter in Glasgow University brought consistency and reliability in patterning even the smallest lithographic features (down to 20nm), and also the ability to pattern mesas, large (500nm) and small (20nm) features on the same sample without having to re-focus the electron beam manually. The effect of this was to enable a wide variety of sizes of both dots and wires to be patterned onto the same sample.

In order to ease comparisons between wire and dot data from the same sample this section will be subsectioned according to sample number and not according to structure type (wires or dots).

Quantum structures were fabricated by the Beamwriter in material which was grown by MOVPE at the RWTH University in Aachen. A diagram of the sample structure is given in figure 6.21.

12nm InP
7nm InGaAs
200nm InP
Semi-insulating InP

Figure 6.21 Structure of sample 2311, sample no.6

All of the samples fabricated using the Beamwriter corresponded to the same general pattern. There were ten arrays on each sample. Three of these arrays were mesas, one had 25nm wide wires, two had 20nm wide dots, one had 40nm wide wires, one had 35nm wide dots, one had 300nm wide wires and the final array had 300nm wide dots. Figure 6.22 shows how the PL integrated intensity varies with exciting laser power. Figure 6.22 was fitted with the curve $y = 33.79\,x^{0.79}$.

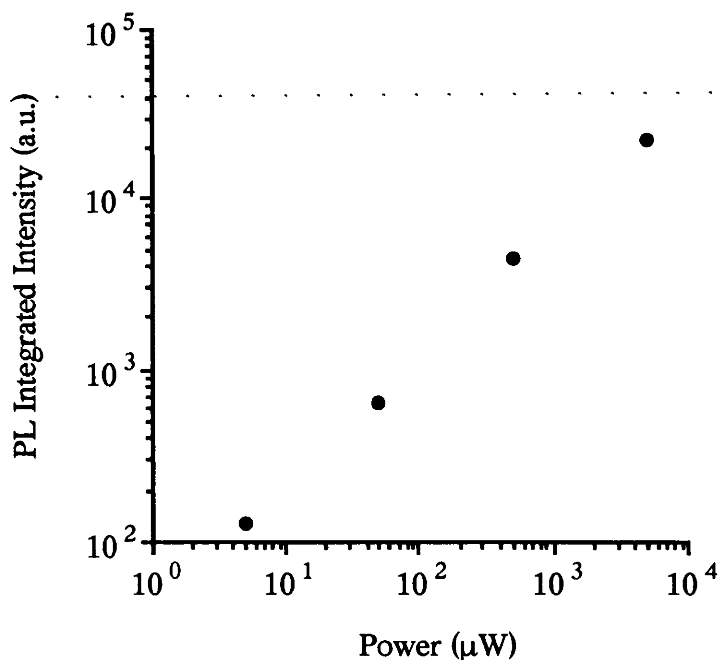

Figure 6.22 Laser power versus integrated emission intensity for material type 2311, the measurements were taken at 6K.

Figure 6.23 shows the temperature dependence of the PL peak positions for material type 2311. The solid line is a least squares fit of the experimental data (experimental data points are shown as small circles) using $E(T) = E(0) + \alpha T^2/(T + \beta)$. The least squares fit gives values of $E(0) = 862.5$meV, $\alpha = -2.71\times10^{-4}$ eV/K, and $\beta = 127.2$K.

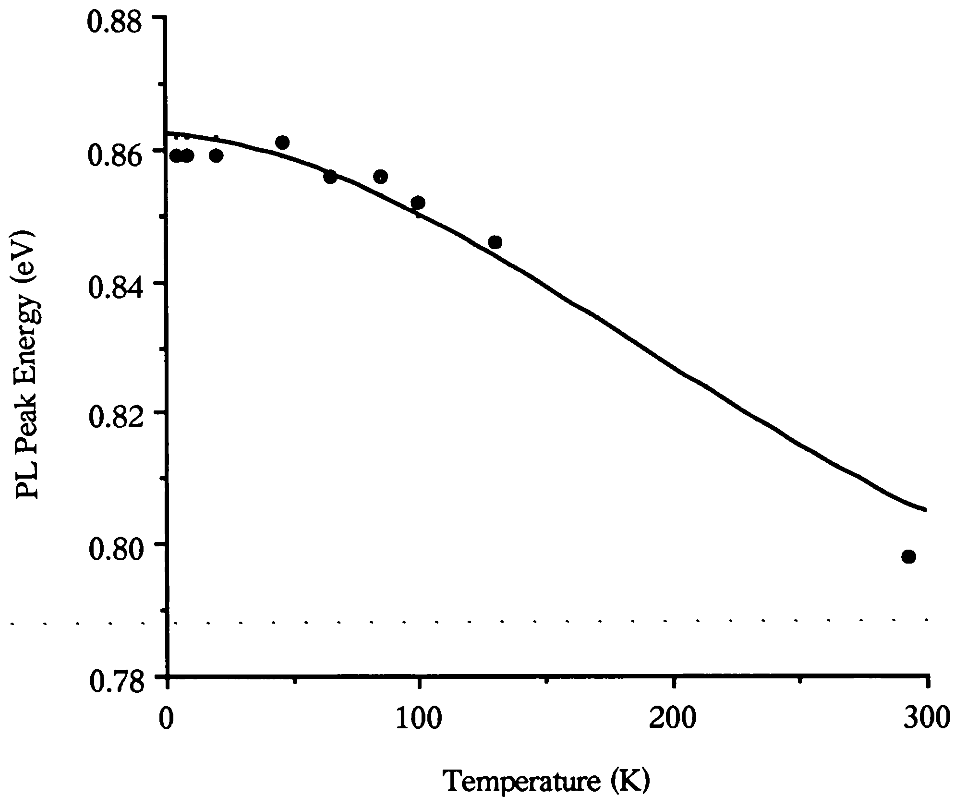

Figure 6.23 Temperature dependence of the PL peak position of material type 2311

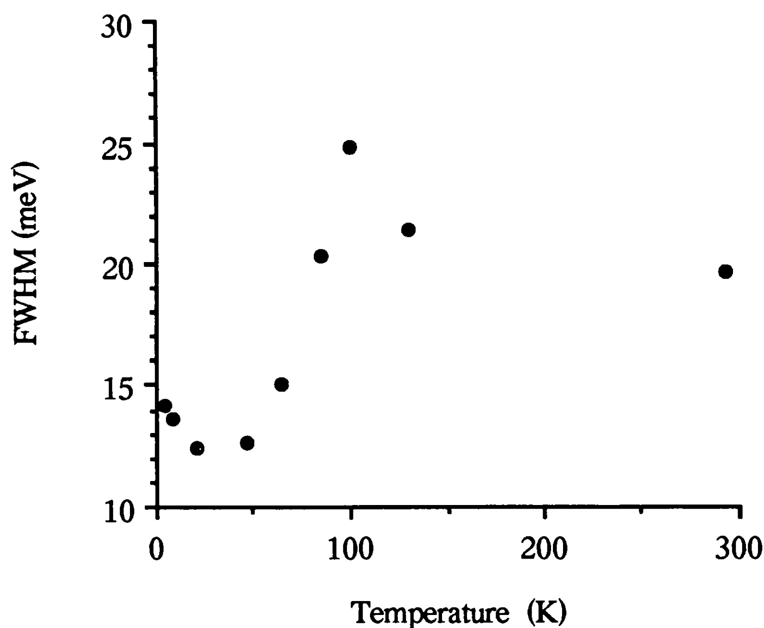

Figure 6.24 Relationship between measured PL peak width and temperature for material type 2311, as used in sample numbers 6 to 10

The slope of the line in figure 6.22 is less than unity (0.79), which suggests that the emission is extrinsic exciton recombination. Figure 6.24 shows a decrease in the FWHM in the temperature region between 20 and 50K, which is indicative of strong localization processes probably due to a combination of alloy fluctuation potentials and interface roughness. Figure 6.24 also indicates that the scattering and localization mechanisms responsible for the shape of the PL emission are very complex.

6.4.1 Wires and dots down to 20nm - sample no.6

Figure 6.25 shows the PL spectra of an array of 20nm wide dots under two different excitation intensities and a neighbouring mesa array.

The PL spectra recorded from an array of 30nm wide wires under 7mW and 3.6mW laser excitation are shown in curves (c) and (b) of figure 6.26, curve (a) is the PL emission from a mesa array.

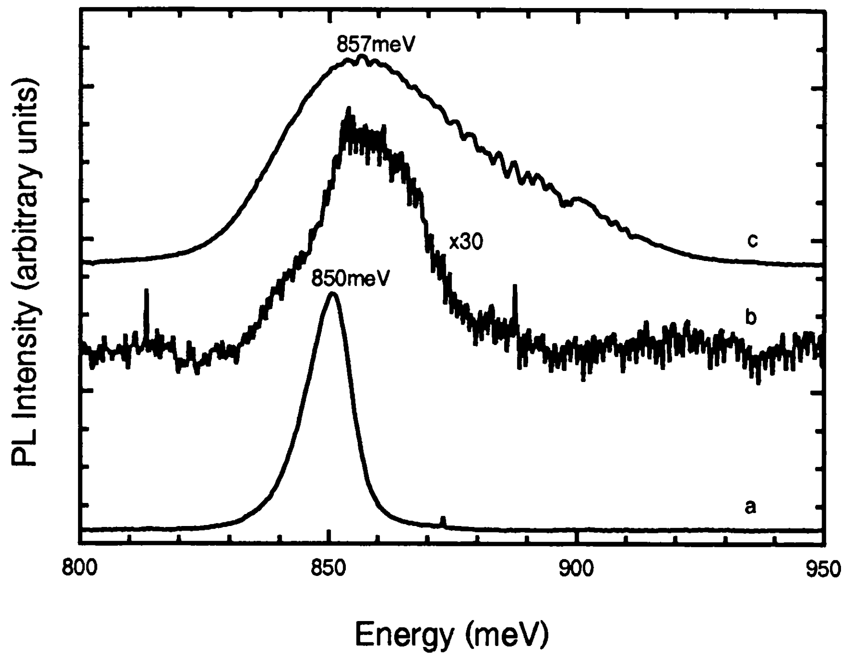

Figure 6.25 PL spectra of a 20nm wide dot array under two different excitation intensities and a mesa area on sample no. 6, a 7nm thick SQW sample. The arrays were excited with the 488nm line of an Ar^+ laser with the sample cooled to 5K. The 20nm wide dots were excited by 7mW (curve c) and 0.6mW (curve b) of laser power, and the mesa (curve a) with 30μW of laser power.

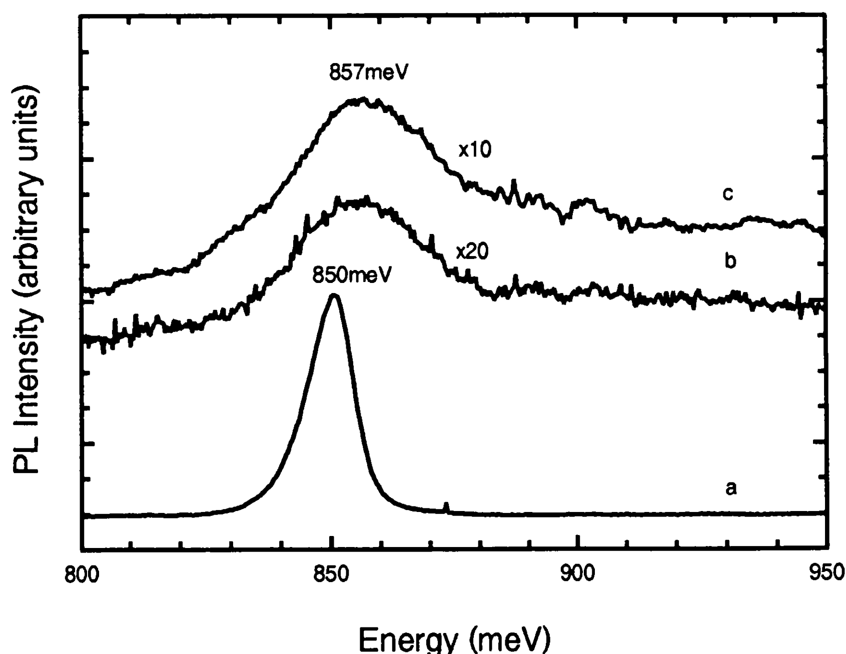

Figure 6.26 PL spectra of a 30nm wide wire array under two different excitation intensities and a mesa array on sample no. 6, a 7nm thick SQW sample. The arrays were excited with the 488nm line of an Ar^+ laser with the sample cooled to 5K. The 30nm wide wires were excited by 7mW (curve c) and 3.6mW (curve b) of laser power, and the mesa (curve a) was excited by 30μW.

6.4.2 Discussion of PL data obtained from sample no.6

The mesa spectrum of figures 6.25 and 6.26 was deconvoluted using a two gaussian approximation. The result is shown in table 6.10.

Gaussian No.	Peak position (meV)	FWHM (meV)	Relative peak intensity (a.u.)
1	848	15.4	0.47
2	851	7.7	0.56

Table 6.10 Deconvolution of mesa spectrum of figure 6.25 using 2-Gaussian approximation

The transition at 851meV is narrow and is probably due to the electron to heavy-hole 1 transition (E1-HH1).

The transition at 848meV is broader than that at 851meV and is probably an impurity related transition. The 3meV energy difference between these transitions is probably due to the binding energy of the exciton bound to an impurity.

The broader FWHM of the impurity related transition at 848meV is not surprising because the binding energy of excitons bound to shallow impurities depends on the location of the impurity, whether it is in the centre or at the edge of the quantum well.

The spectra of figure 6.25 refer to the PL emision from dots of 20nm diameter. When dots this small are fabricated then - according to theory - the regime of strong confinement (separate electron and hole confinement) is entered (see section 1.5.2). However, spectra (b) and (c) do not show large energy shifts of the main recombination peak with respect to the mesa.

The reduction in laser power of one order of magnitude (spectrum (b) compared with spectrum (c)) leads to a fifty-fold reduction in the integrated PL intensity, which suggests that strong non-radiative recombination channels are present. In addition, considerable narrowing of the spectrum occurred (from a FWHM of approximately 48meV to 26meV). It is interesting to note that the bulk of the narrowing occurred at the high energy side of the peak, while the low energy onset of PL emission remained almost unchanged. This is consistent with the low energy emission arising from impurity related effects and the high energy emission from a bottlenecking of the carriers at higher energy levels. With the reduced excitation power the bottleneck is reduced and consequently the emission from these higher energy levels is reduced. Spectrum (c) was deconvoluted using a 3-Gaussian approximation and the results are given in table 6.11.

Gaussian no.	Peak position (meV)	FWHM (meV)	Relative peak intensity (a.u.)
1	845	19	0.10
2	858	37	0.74
3	892	36	0.23

Table 6.11 Deconvolution of spectrum (c) on figure 6.25 using a 3-Gaussian approximation

The deconvoluted spectrum reveals a peak at 845meV which is probably due to impurity incorporation, a peak at 858meV, which would represent a blue-shift of the main peak of 8meV, and a small broad peak at 892meV which could represent emission from higher energy levels (a series of zero dimensional states).

The difference in the shape of spectra (b) and (c) of figure 6.25 graphically illustrates the acute effect that the laser power has on the shape of the spectrum. This is almost entirely because of the small number of states which remain in these nanostructures to participate in the luminescence process.

The PL spectrum of 50nm wide dots (not shown) exhibited broadening of the PL emission but no shift of the peak with respect to the mesa. This suggests that the separate confinement regime is not reached for this lateral size of InGaAs/InP structures.

The spectra of figure 6.26 represent the emission from 30nm wires. Again, two different excitation powers were used but there was no appreciable change in the shape of the spectrum. When the laser excitation power was reduced from 7mW to 3.6mW (curves (c) and (b) of figure 6.26, respectively) the integrated intensity diminished by 50%, which is consistent with a 50% reduction in excitation power. Notice that PL emission was detected even at high energies (up to 950meV), this is a signal, not just a background count.

Spectrum (c) on figure 6.26 was modelled using a 3-Gaussian approximation. The parameters produced by this approximation are given in table 6.12.

Gaussian no.	Peak position (meV)	FWHM (meV)	Relative peak intensity (a.u.)
1	831	10	0.07
2	855	28	0.63
3	876	81	0.30

Table 6.12 Results of 3-Gaussian deconvolution of spectrum (c) on figure 6.26

The peak at 831meV probably corresponds to shallow impurities, the emission of which is enhanced by the etching process. The peak at 855meV is the main peak shifted to higher energies, and the emission at higher energies is perhaps due to a contribution from higher energy levels, but it is so broad and flat that it is difficult to determine the position of specific energy levels.

After measuring the PL signal of these samples it was decided to anneal them to check whether or not this had any effect on the PL signal, especially regarding the shape or intensity of the signal. It was suspected that hydrogen might have some effect on the PL intensity. Another reason was that impurities at the interface may be thermally removed after the annealing process, and finally, annealing might also reduce any disorder effects. In order to avoid confusion the annealed pieces of sample no.6 will be referred to as pieces of sample no.7.

6.4.3 Annealing of wires and dots - sample no. 7

The pieces of sample no. 7 were placed on a copper/beryllium block which was then transferred to a copper surface which was maintained at a temperature of 400°C for 2

minutes under a continuous flow of argon/hydrogen gas (95% Ar, 5% H_2). These pieces were then remounted on the cryostat insert and PL experiments were performed.

6.4.3.1 PL spectra obtained from sample no.7

Figure 6.27 shows two spectra obtained from the array of 20nm wide dots before annealing and after annealing. As can be seen from the figure the signal intensity has been reduced by an order of magnitude.

Figure 6.28 shows another two spectra, this time these were taken from an array of 50nm wide dots (not shown previously) before and after the sample was annealed. There is a narrowing of the PL signal and, once again, the intensity of the PL of the annealed sample is lower than the PL of the sample prior to annealing.

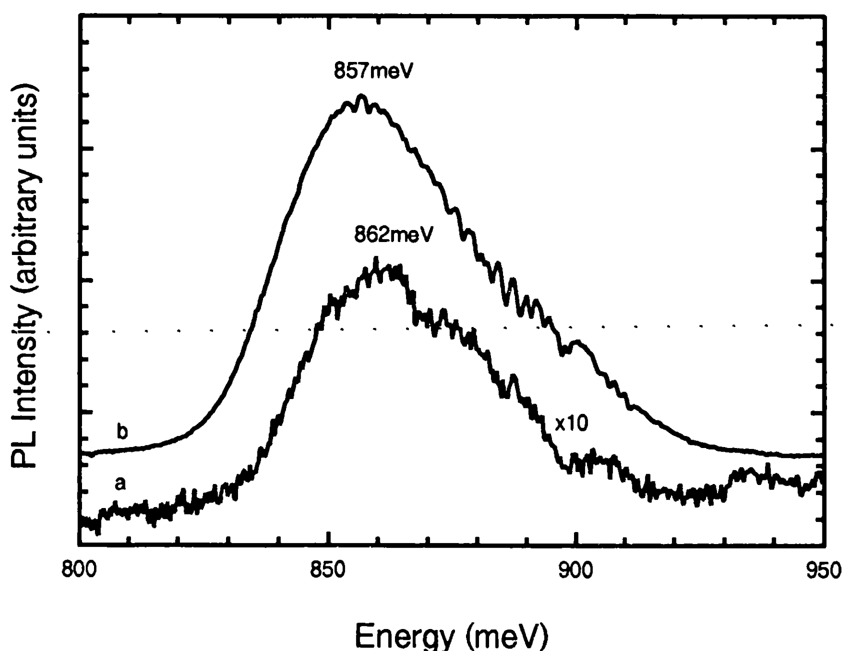

Figure 6.27 PL spectra of a 20nm wide dot array on sample no. 7 (a 7nm thick SQW sample) before (curve b) and after (curve a) annealing. The sample was maintained at 5K during the measurements while the 488nm line of an Ar^+ laser was used to excite the arrays. The laser power used was 7mW for the upper curve and 8mW for the lower curve.

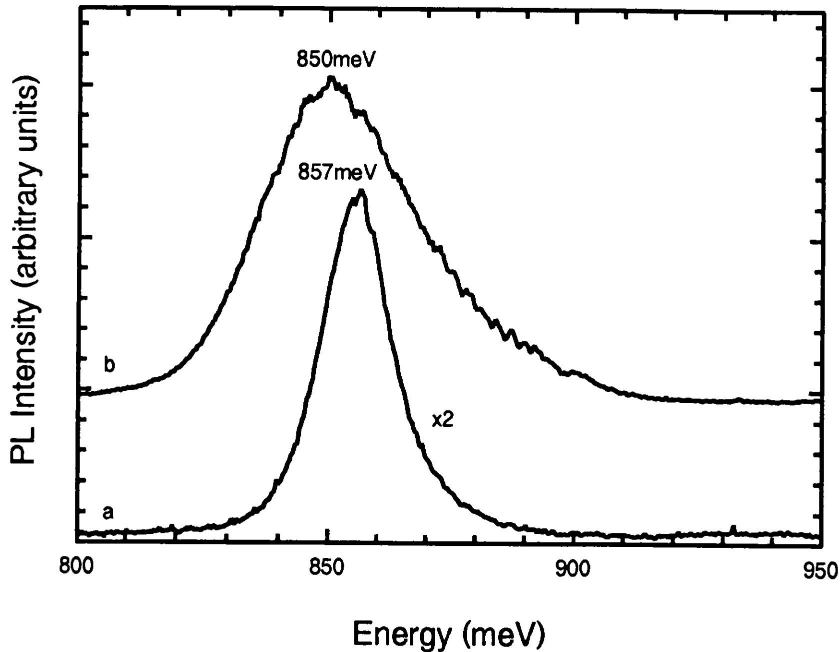

Figure 6.28 PL spectra of a 50nm wide dot array on sample no. 7 (a 7nm thick SQW sample) before (curve b) and after (curve a) annealing. The sample was maintained at 5K during the measurements while the 488nm line of an Ar^+ laser was used to excite the arrays. The laser power used was 2.6mW for curve (b) and 8mW for curve (a).

6.4.3.2 Effects of annealing on quantum dots

In figures 6.27 and 6.28 a comparison is made between the PL spectra before and after annealing for two different dot sizes. PL measurements on the mesa arrays before and after annealing (not shown) reveal a decrease in the integrated intensity after the annealing cycle but no change in the PL peak position, shape or linewidth. Typically, after the annealing stage a mesa had to be excited with an order of magnitude more laser power to produce a signal intensity comparable to what was emitted prior to annealing. Similarly, figures 6.27 and 6.28 clearly show a decrease in integrated PL intensity after annealing.

There seems to be reasonable consistency between the factor of 10 more power needed for the mesa, the factor of 10 less luminescence from the 20nm dots, and the factor of 3 more power required to produce half the luminescence from the 50nm wide dots. So the effect of annealing seems to be uniform and not greater for the smaller dots than for the larger dots.

Both figures 6.28a and b were deconvoluted using a 3-Gaussian approximation, whereas a 4-Gaussian approximation was used for figure 6.27a and a 2-Gaussian for figure 6.27b. The results are given in table 6.13.

Figure	Gaussian No.	Peak position (meV)	FWHM (meV)	Relative intensity (a.u.)
6.27a	1	856	29	0.9
	2	863	7	0.1
	3	879	22	0.4
	4	891	35	0.1
6.27b	1	854	33	0.9
	2	883	44	0.4
6.28a	1	848	19	0.2
	2	856	14	0.7
	3	864	24	0.2
6.28b	1	846	25	0.4
	2	855	42	0.7
	3	891	24	0.1

Table 6.13 Deconvolution of figures 6.27 and 6.28

In figure 6.27 the annealing stage has had the effect of slightly increasing the position of the main peak at ~854meV and narrowing it by 4meV. The narrowing is probably due to the impurities incorporated during etching, which are removed by the annealing stage.

Although the shape of the spectrum in figure 6.28a is very different to that of figure 6.27a there are some similarities.

In figure 6.28a (like 6.27a) the lowest (energy) peak (from table 6.13) occurs a few meV higher in energy and is a few meV (6meV) narrower than the corresponding peak of the spectrum prior to annealing. The main peak occurs at ~855meV and is largely unaffected by the annealing stage (i.e. it is not shifted much (1meV) and it is still the most intense of the three peaks).

Once again, annealing of impurities would seem to be the cause of the narrowing of the spectrum. It is interesting to note that the emission peak at lowest energies for figure 6.28a occurs at approximately the same energy as the mesa emission.

6.4.4 Wet etching of dry etched structures

A few research groups have reported that they performed a brief wet chemical etch after the dry etching stage in order to remove any surface contaminants and smooth the wire sidewalls (e.g. Izrael et al, 1991 and Samuelson et al, 1992).

For similar reasons, it was decided to perform a brief wet chemical etch on the pieces of sample no. 7 and then examine them by PL spectroscopy to see whether or not the etch had any effect on the PL. The etch which was chosen had to be non-selective (it had to etch both the InGaAs and InP) and so the following etch was used (which was detailed in section 3.3.1 of this thesis)

4ml HCl : 4ml H_2O_2 : 4ml CH_3COOH

The pieces of sample no. 7 were mounted together and dipped into the etch momentarily (approximately two seconds). To avoid confusion this sample (after the wet etching stage) will be referred to as sample no. 8.

6.4.4.1 PL of annealed and wet etched structures - sample no. 8

A small PL signal was obtained from the narrowest dots but it was so noisy that no accurate measurements could be obtained from it. The only pieces of the sample which produced any quantifiable signal were the mesa area and the portion which had dots which were originally 50nm wide but were reduced to approximately 30nm in diameter after the wet etch stage. Figure 6.29 shows two spectra. The upper curve is the PL obtained from the 30nm wide dots (30nm is the size of the dots after the wet etch stage) and the lower curve is the PL obtained from the mesa area.

A shift of 12meV between PL peaks can be clearly seen in figure 6.29. The effect of impurities at low energies seems to have disappeared entirely because figure 6.29b is almost symmetrical and can be approximated very well by a single gaussian peak centred at 865meV with a FWHM of 33meV.

By this stage the sample had been subjected to both annealing and wet etching. In order to ascertain the effect of wet etching on its own a sample was taken and a brief wet etch was performed after the RIE stage, with no annealing stage.

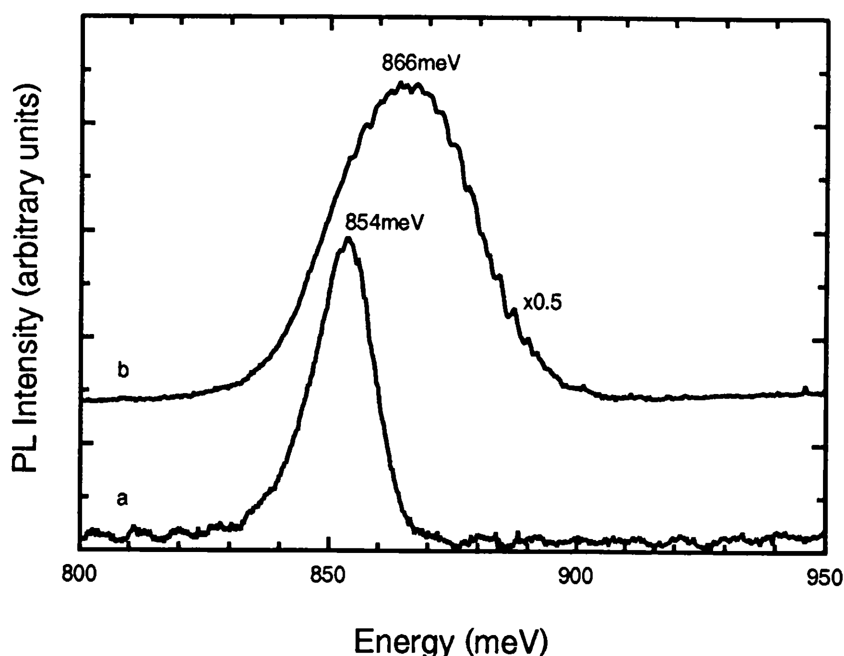

Figure 6.29 PL spectra of an annealed and wet etched 30nm wide dot array and a mesa area on sample no. 8, a 7nm thick SQW sample. The arrays were excited with the 488nm line of an Ar^+ laser with the sample cooled to 5K. The 30nm wide dots (curve b) were excited by 7mW of laser power and the mesa (curve a) was excited by 1.5mW of laser power.

6.4.4.2 Wires and dots - sample no.9

A fresh portion of sample no.6 (shown in figure 6.21) was taken and mesas, wires and dots were fabricated on this sample using the Beamwriter. Immediately after the dry etching stage a brief wet chemical etch was performed, i.e. unlike sample no.8 this sample was not annealed. This sample will be referred to as sample no. 9. The structure sizes which resulted after these two etching stages were measured in an electron microscope and then the sample was scribed into individual arrays and these arrays were then mounted ready for PL experiments.

In figure 6.30 the PL emission from an array of large (330nm diameter) dots (curve b) is compared with the mesa emission (curve a). The laser excitation was 30μW in each case. The PL emission of the large dots is surprisingly strong, the luminescence intensity of the dots is approximately half that of the mesa, and yet the dots have an active area which is only 5% of that of the mesa. There is a slight blue-shift of the dots with respect to the mesa (1meV) but this is unlikely to be due to any confinement effects, it is more likely to be due to a slight variation of the peak position over the wafer surface.

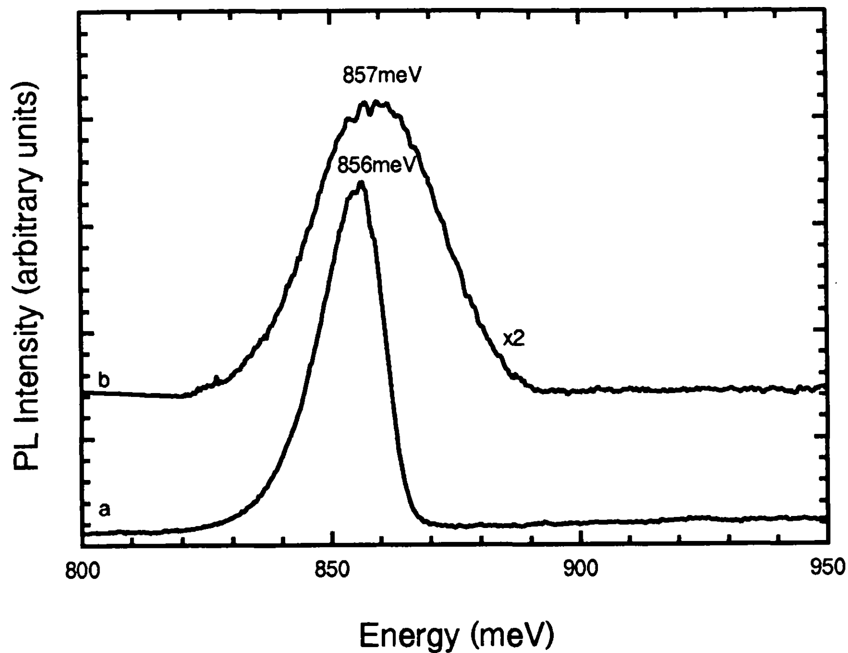

Figure 6.30 PL spectra of a 330nm wide dot array and a mesa area on sample no. 9, a 7nm thick SQW sample. The arrays were excited with the 488nm line of an Ar^+ laser with the sample cooled to 5K. The 330nm wide dots (curve b) were excited by 30μW and the mesa (curve a) was also excited by 30μW.

In figure 6.31 the PL emission from an array of small (20nm) dots (curve b) is compared with the mesa PL emission (curve a). The 20nm dots show a blue-shift of 4meV with respect to the mesa and 3meV with respect to the large dots. The 20nm dot spectrum has a FWHM of only 23meV, which is quite narrow compared with the FWHM of figures 6.11 to 6.15 (~100meV).

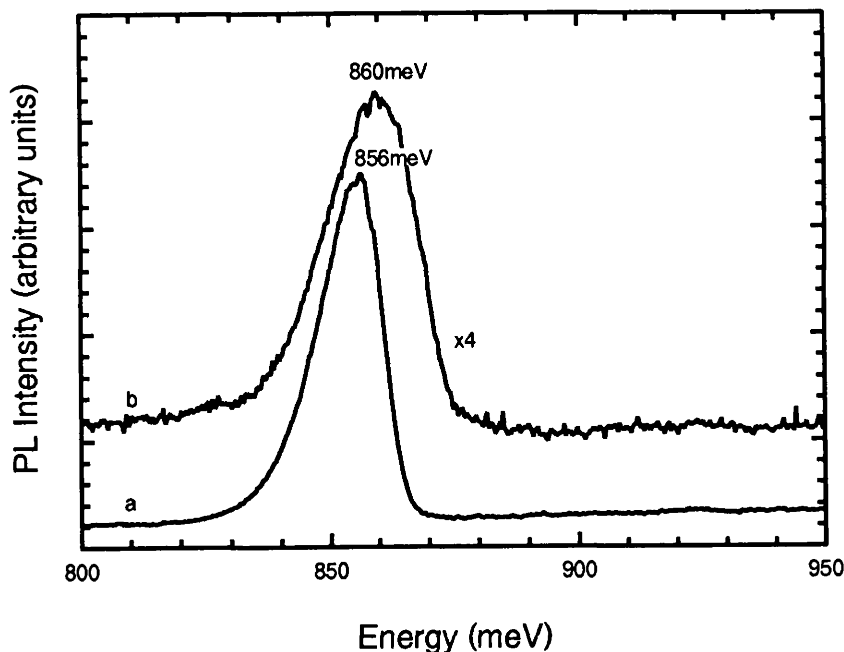

Figure 6.31 PL spectra of a 20nm wide dot array (b) and a mesa array (a) on sample no. 9, a 7nm thick SQW sample. The arrays were excited by the 488nm line of an Ar^+ laser with the sample cooled to 5K. The 20nm wide dots (curve b) were excited by 2.4mW and the mesa (curve a) was excited by 30μW.

In figure 6.32 the PL emission from an array of very small (10nm) dots (curve b) is compared with the PL emission of a mesa area (curve a). The PL of the 10nm dots shows a clear blue-shift of 6meV with respect to the mesa and 5meV with respect to the large dots. Again, the spectrum of the 10nm dots is reasonably narrow (26meV).

Finally, figure 6.33 shows the PL emission from an array of small (25nm) wires (curve b) compared with the PL emission from a mesa area (curve a). The PL spectrum of the wires shows a 4meV blue-shift with respect to the mesa, 3meV with respect to the large dots (figure 6.30). The wire PL emission has a FWHM of 21meV.

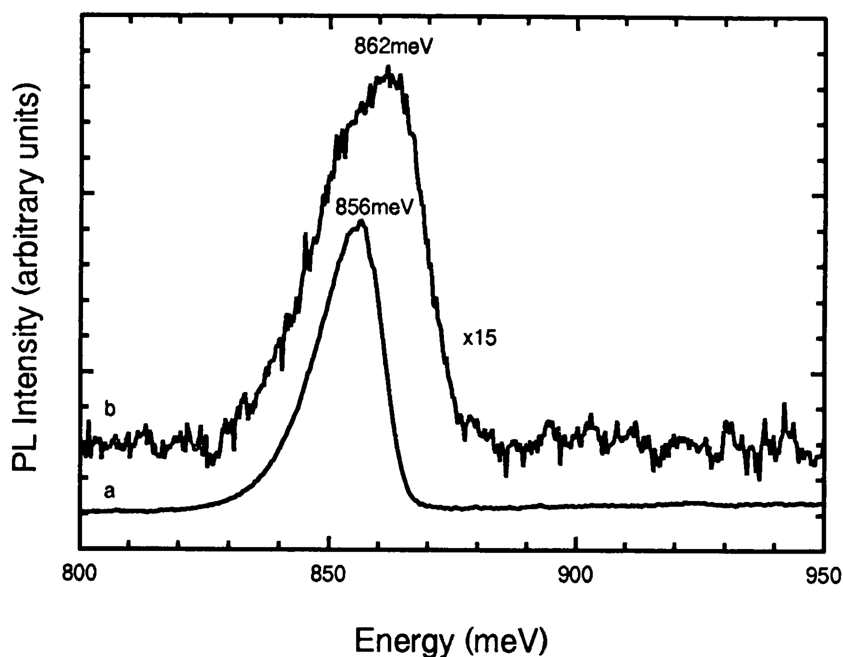

Figure 6.32 PL spectra of a 10nm dot array and a mesa array on sample no. 9, a 7nm thick SQW sample. The arrays were excited by the 488nm line of an Ar^+ laser with the sample cooled to 5K. The 10nm wide dots (curve a) were excited by 9mW and the mesa (curve b) was excited by 30μW of laser power.

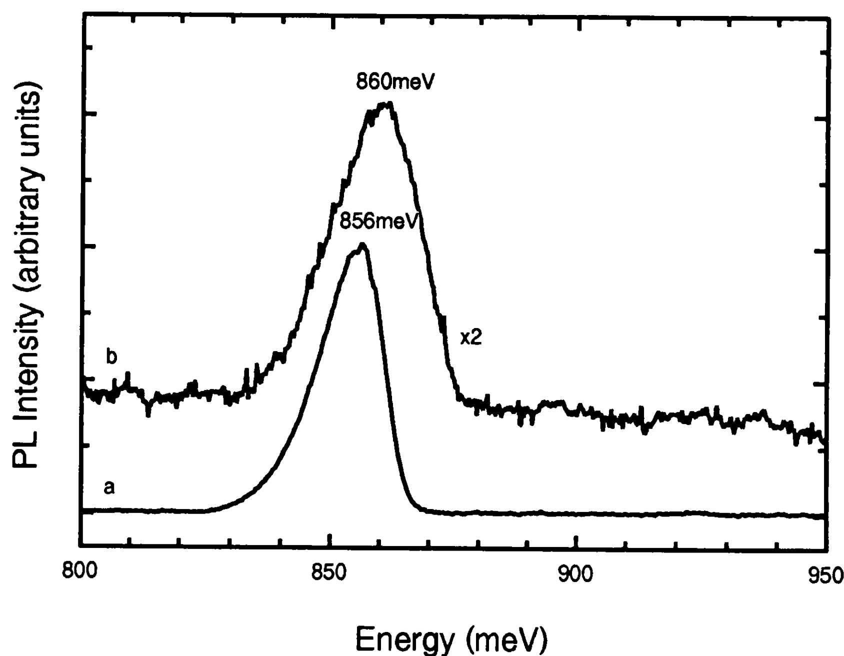

Figure 6.33 PL spectra of a 25nm wire array and a mesa area on sample no. 9, a 7nm thick SQW sample. The arrays were excited by the 488nm line of an Ar^+ laser with the sample cooled to 5K. The 25nm wide wires (curve b) were excited by 5mW and the mesa (curve a) was excited by 30μW of laser power.

6.4.4.3 The effect of wet etching on quantum structures

None of these spectra (figures 6.29 to 6.33) shows any high energy hump. Previously the PL of the wire and dot arrays always exhibited a hump/peak to higher energies (see figures 6.15, 6.18 etc.). However, when samples were dipped into a wet chemical etch after the dry etching stage then the high energy hump seemed to disappear.

The shape of the spectra in figures 6.29 to 6.33 is much closer to that which was expected prior to undertaking this research. Each spectrum is almost symmetrical, with only a slight shoulder at low energies due to impurity emission. These impurities were probably incorporated during reactive ion etching. The most symmetric spectrum of them all is figure 6.29b. This is the sample which was annealed and wet etched, the rest were only wet etched. This observation is consistent with the fact that annealing tends to remove or seriously inhibit the effect of impurities, and these impurities cause the shoulder at low energies on figures 6.30 to 6.33.

The absence of the peaks at higher energies is not so easy to account for, since the wet etch only removes a few nanometres from the sample surface. However, this has an enormous effect on the shape of the spectrum. Notice the sharp cut-off in luminescence in figures 6.31b, 6.32b and 6.33b, which contrasts starkly with the luminescence obtained from 50nm dots patterned on the same material (figure 6.28b). This shows that on the same material type (all of these figures relate to dots and wires patterned onto 2311 material from Aachen) a radically different PL spectrum is obtained depending on whether wet etching is used or not.

In addition to removing a few nanometres of the surface wet etching also removes the strontium fluoride based mask. It is possible that this mask causes strain in these small structures, which is released when it is removed. However, it seems unlikely that any strain effect would cause emission from higher energy levels to occur.

The FWHM of the Aachen grown samples (2311) is narrower than that of the Sheffield grown sample (PMB297), typical values of which are given in table 6.1. When figure 6.28b (50nm dots grown on 2311) is compared with figure 6.19d (20nm wires on PMB297) it is clear that the high energy emission from the PMB297 samples extends to higher energies than the 2311 sample. Since sample PMB297 has a larger FWHM than 2311 it is possible that the larger amount of alloy fluctuations (in PMB297) localise the exciton. It should be noted that the intensity versus wire length experiments of section 6.3.1 (which were done on samples B555 and B556 which had the largest FWHM of the four sample types used in this research) showed no evidence of exciton transport/diffusion.

6.4.5 Summary of PL experiments on samples fabricated with the Beamwriter

Table 6.14 shows the position of the PL peak (in meV) for different arrays of wires, dots and mesas after various fabrication stages. The dash (-) is included where no signal could be detected. The last entry in the last column has 30nm in brackets because this was the size of the array after the wet etching stage. Table 6.15 shows similar data for sample no. 9, which was wet etched immediately after the dry etching stage.

Structure Type	As-Etched	Annealed	Wet-Etched
MESA	850	854	856
20nm DOTS	857	862	-
30nm WIRES	857	-	-
50nm DOTS	850	857	866 (30nm)

Table 6.14 PL peak positions (in meV) for different structure types (fabricated on material 2311) after various fabrication processes

Structure Type	Wet-Etched
MESA	856
20nm DOTS	860
10nm DOTS	862
25nm WIRES	860

Table 6.15 PL peak positions for different arrays after wet and dry etching

Figure 6.34 shows a graph of the energy shift versus diameter for wet etched quantum dots of sample no 9. It clearly shows an increase in the energy of the main emission with decreasing diameter of quantum dots, starting at approximately 50nm. The blue-shift is significantly smaller than expected (by several tens of meV). The main explanation for this is probably based on the release of the tetragonal distortion of the GaInAs-InP (Ryan et al 1987) system when grown on InP (2.73×10^{-3} lattice mismatch). The smallest structures undergo strain relief which results in the GaInAs layer being subjected to a biaxial tensile strain on the plane of the well. This may push the energy levels to lower energies (red-shift) which counteracts the blue-shift, rather like the case of Si-SiGe quantum wires (Tang et al 1992). The calculation is rather involved and was beyond the scope of this work. It is clear

that for non-perfect lattice matched heterostructures, deep etching will alter (relieve) the strain compared with the as-grown samples.

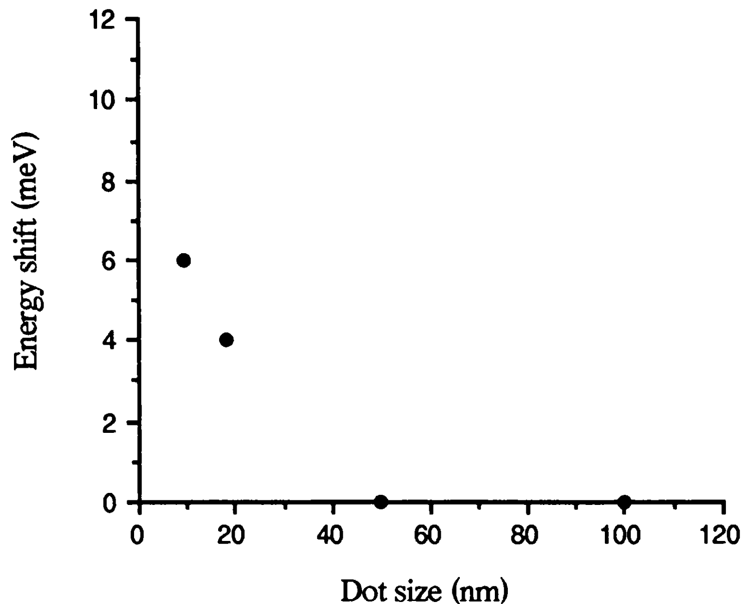

Figure 6.34 Graph of energy up-shift versus diameter for reactive ion and then wet etched quantum dots fabricated on material type 2311.

6.5 Experiments performed with an FFT spectrometer

This section deals with the work performed at UMIST in conjunction with Dr R Pritchard, who configured the Fast Fourier Transform (FFT) apparatus.

A number of samples were taken to Manchester. One of the samples - previously called sample no 4 - was patterned by the Jeol and details of the PL measurements are given in section 6.3.2. This sample was used because it emitted light very strongly, as demonstrated by the spectra shown in figures 6.11 to 6.15 which only required excitation with powers of approximately 200μW to produce measurable PL signals. The strong PL signals were probably due to the high fill-factor (20%) for this sample compared with the wire arrays patterned by the Beamwriter (which had a typical fill-factor value of 7%).

6.5.1 FFT PL and absorption measurements on sample no. 4

The reason for doing experiments with the FFT spectrometer-based system in UMIST was to obtain a PLE spectrum of the wires. However, as mentioned in section 5.4, PLE measurements could not be performed on any of the samples. The reason for this was not directly due to a lack of luminescence signal but because of a problem inherent in the sample design which was not suited to the way the experimental apparatus was configured. However, absorption experiments were performed on this sample.

Figure 6.35 shows the absorption spectrum which was obtained from an array of 30nm wide wires. The spectrum is the result of recording and averaging over 500 spectra. It is superimposed on the PL spectrum obtained from a neighbouring mesa area. This spectra shows that the absorption begins below the energy corresponding to the mesa emission and continues steadily. Several points are labelled on the absorption spectrum but it is difficult to attribute these to any particular emission. These bumps in the spectrum were taken from the derivative of the absorption curve. These experiments are to be regarded as a preliminary investigation of the suitability of FFT PL and absorption for nanostructure devices.

If a sample layout was specifically designed for use with FFT absorption apparatus then the signal obtained may be large enough to yield useful information. Part of the difficulty with this experiment was the low signal to noise ratio because the sample design was not suited to the particular FFT experimental set-up used.

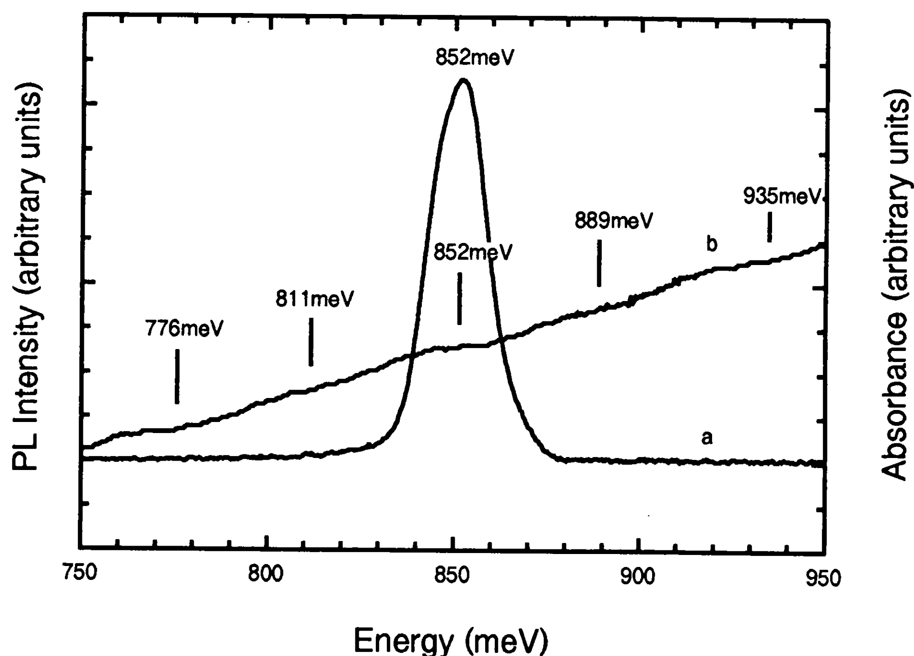

Figure 6.35 FFT absorption (curve b) and PL spectrum (curve a) obtained from a 30nm wide wire array and mesa area, respectively, on sample no. 4. Which was an 8nm thick SQW sample cooled to 5K. The mesa was excited with 5mW of power from the 633nm line of a He-Ne laser.

6.5.2 Spatially resolved PL experiments

The SRPL apparatus was used to provide information which could not be obtained from standard PL experiments. One piece of information provided by SRPL was the variation in the PL emission across a mesa. Owing to its ability to measure the luminescence emitted from a small region, SRPL enabled mapping of the PL peak position and intensity across a mesa to be performed. However, one disadvantage of the apparatus was that the signals obtained from the samples were very low. Initially, a cold finger cryostat was used which had a copper block cooled to liquid nitrogen temperatures (77K). The signals obtained were so weak (the signal was directed towards the FFT spectrometer by five or six mirrors) that only the PL emission from the mesa areas could be detected. Figure 6.36 shows two spectra obtained at different points of a mesa area on sample no. 4. This figure shows that there is no appreciable difference in either the peak position, intensity or linewidth across the mesa.

In an effort to detect a signal from a wire or dot array a specially modified Oxford Instruments cryostat was used. Sample no. 10, which was almost identical to sample no.6, was loaded into this cryostat and cooled to 10K. Only the mesa emission could be recorded

due to the weak signals associated with wires and dots. Three spectra were recorded from one mesa area and the results are shown in figure 6.37.

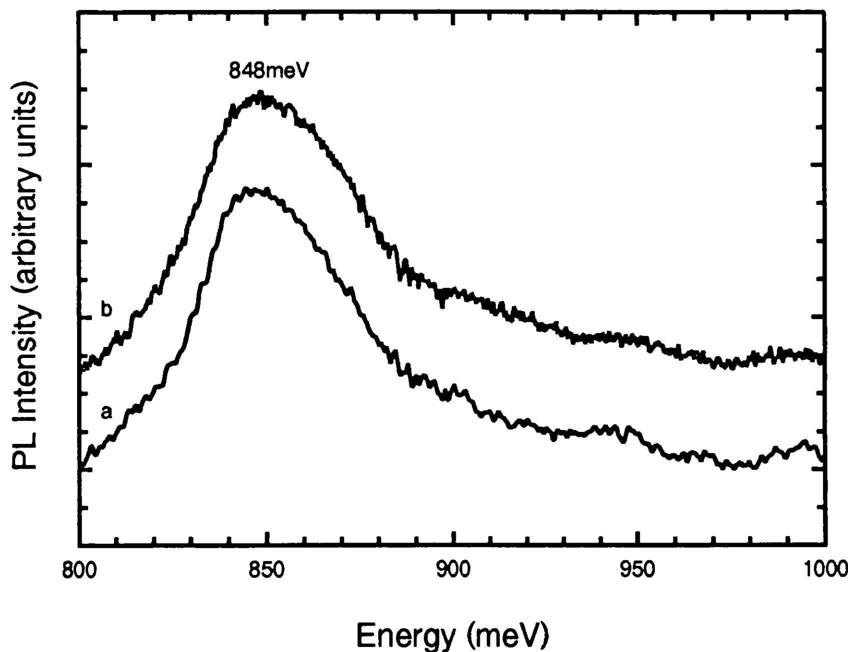

Figure 6.36 SRPL spectra of different sites of a mesa area on sample no. 4, an 8nm thick SQW sample, cooled to 77K. The 633nm line of a He-Ne laser was used to excite the sample with a laser power of 5mW.

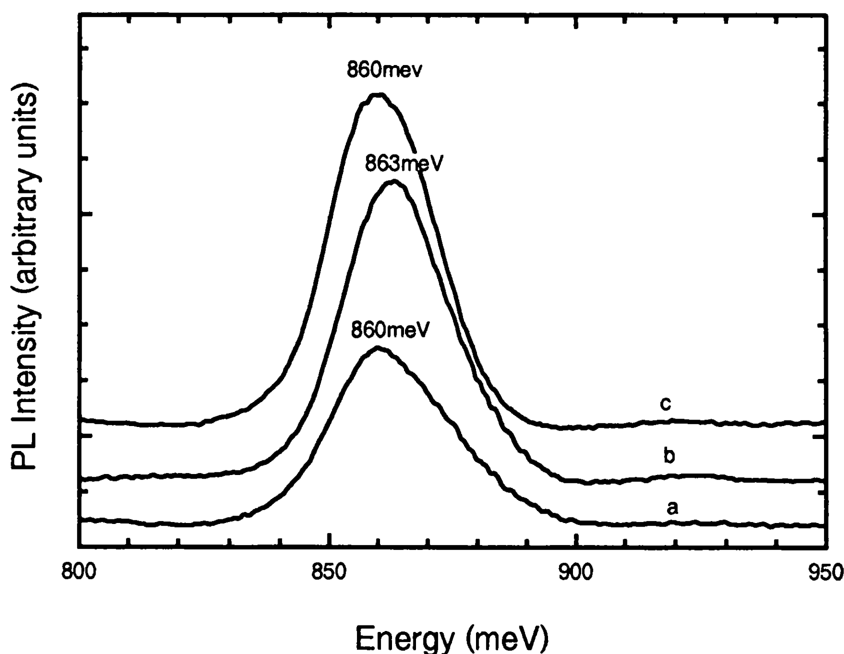

Figure 6.37 SRPL spectra of three different sites on a mesa area on sample no. 10, a 7nm thick SQW sample, cooled to 10K. The 633nm line of a He-Ne laser was used to excite the sample with a laser power of 5mW.

This time, there was a slight change in the PL intensity and a slight shift (3meV) in peak position over the mesa area. It is interesting to note that PL measurements from other mesa sites on the sample gave similar results as to peak position and luminescence intensity.

These results demonstrate the uniformity of PL emission from individual mesa areas and from areas across the sample surface, thus giving credence to the claims made previously (sections 6.3 to 6.5) that energy up-shifts of the PL spectra have been recorded and are not due to variations in the peak position across the wafer.

References

Benisty H, Sotomayor Torres C M and Weisbuch C, 1992 Phys Rev B 44 (19) p10945-10948

Camassel J, unpublished work

Izrael A, Marzin J Y, Sermage B, Birotheau L, Robein D, Azouley R, Benchimol J L, Henry L, Thierry-Mieg V, Ladan F R and Taylor L 1991 Japanese Journal of Applied Physics 30 (11B) p3256-3260

Leitch W E, Sotomayor Torres C M, Lootens D, Thoms S, van Daele P, Stanley C R, Demeester P and Beaumont S P 1992 Surface Science 263 p622 - 627

MacLeod R W, Sotomayor Torres C M, Tang Y S and Kohl A 1993 Journal de Physique IV, Colloque C5, Supplement au Journal de Physique II, Vol 3 p335 - 339

Notomi M, Naganuma M, Nishida T, Tamamura T, Iwamura H, Nojima S and Okamoto M 1991 Appl. Phys. Lett. 58 (7) p720 - 722

Patillon J N, Jay C, Iost M, Gamonal R, André J, Soucail B, Delalande C and Voos M 1990 Superlattices and Microstructures 8 (3) p335 - 339

Ryan T W, Hatton P D, Bates S, Watt M, Sotomayor Torres C M, Claxton P A and Roberts J S 1987, Semicon. Sci. Technol. 2 p241 - 243

Skolnick M S, Nash K J, Saker M K, Bass S J, Claxton P A and Roberts J S 1987 Appl. Phys. Lett. 50 (26) p1885 - 1887

Samuelson L, Georgsson K, Gustafsson A, Maximov I, Montelius L, Nilsson S, Seifert W and Semu A 1992 Proc SPIE Symposium on Compound Semiconductor Physics and Devices vol 1676 p154-160

Tang Y S, Sotomayor Torres C M, Wilkinson C D W, Smith D W, Whall T E, Parker E H C 1992 Superlattices and Microstructures 12 p535

Chapter 7 Conclusions and further work

7.1 Conclusions

A high resolution fabrication process has been developed which enables wire and dot structures with lateral dimensions down to 10nm to be fabricated. The quantum wire and dot structures are optically active even at these small dimensions, which indicates the absence of a large (19nm) "dead layer" at the sidewalls of the structures, as was reported in some fabrication processes (Maile et al 1989). The high resolution process involves electron beam lithography, RIE, and wet chemical etching and is compatible with device integration.

Quantum confinement has been clearly observed in the low temperature emission spectrum of quantum structures. However, the absolute confining energy could not be determined accurately because of the interplay between carrier lateral confinement and localization effects (due to impurities, alloy fluctuation, well width fluctuation). An in-depth study of systems, such as InGaAs/InP, containing defects and localization centres is required.

It was found that exciton transport plays a crucial role in the emission strength of wires. This is because of exciton localization effects resulting from variations in the layer thickness at the InGaAs/InP interface, and alloy potential fluctuations. When the exciton is localized it behaves as if it was in a quantum dot, and so it is not affected by the wire length. Exciton transport and the scattering that excitons undergo during it are important factors in the use of quantum wires for 1-D lasers as they may not permit a full reduction of the laser threshold current. These factors are should be investigated further.

A study of process-induced effects on the PL spectra of dots and wires has been presented. The processes studied included both wet etching and annealing after the RIE stage. It was found that annealing a sample after it had been etched in a reactive ion etch machine reduced the absolute PL intensity of the quantum structures and also caused a narrowing of the PL emission. When a sample was subjected to RIE, annealing and then wet chemical etching there was a clear shift of the PL peak position to higher energies for dots of 30nm diameter or less.

To separate the process-induced effects of annealing from those effects induced by wet etching, a test was conducted in which a sample was wet etched immediately after the RIE stage. The main finding was that spectra corresponding to the emission of small dots and wires were considerably narrower than the emission of wires and dots of comparable sizes which were only subjected to RIE. There was also a sharp cut-off in high energy emission in the samples which had both wet and reactive ion etches performed on them, compared with the broadening to high energies present in the samples which were subjected to RIE only. This indicates that the role of the surface of the dots and wires needs to be carefully considered, particularly with reference to strain and impurities, either of which could have been affected by the wet chemical etch.

The bottleneck model, when considered with respect to the samples used throughout this research, seemed to apply best to sample number 5 (PMB297). The bottleneck model is concerned with the energy levels within a semiconductor and is most applicable to intrinsic recombination processes. For this reason it is not surprising that the data obtained from sample number 5 fits the bottleneck theory reasonably well. The recombination from this sample was found to be mostly intrinsic in nature, whereas the recombination from the other samples had an extrinsic contribution.

The role of hydrogen in GaInAs and InP remains to be studied. It is clear that part of the changes in the intensity of the emission spectrum may be related to hydrogen incorporation during etching and perhaps also desorption during annealing. A detailed study of the effect of hydrogen in these semiconductors would yield the information necessary for the process design of doped nanostructures, as required for most applications. From previous work in GaAs it is known that hydrogen incorporation affects the electrical and optical activities of donor and/or acceptor related processes, and there is no reason to believe that it will be different in GaInAs/InP.

The fabrication process seems to be quite good since luminescence has been observed from structures down to 10nm in diameter. To test whether the fabrication process could be improved, different gases could be used in the RIE machine. Perhaps using a different gas

might reduce the damage inflicted. An ECR etching process might introduce less damage during etching than a conventional RIE machine, this is another avenue which could be pursued to try to optimize the fabrication process.

The alloy system of GaInAs/InP does not seem to be good enough at present for producing optical nanostructure devices because of poor quality interfaces and alloy fluctuations. Their inhomogeneities are exacerbated by processing steps making it difficult to predict and control the strength, energy and width of the emission. Possibilities for improvements on this front include:

(i) MBE growth of the alloy quantum wells by a digital technique depositing submonolayers of InAs and GaAs to build up the alloy;

(ii) exploration of GaInAs islands nucleation mechanisms which result in islands buried in a GaAs matrix; and

(iii) the development of low ion energy etching techniques such as ECR or variations of it.

Samples with excessive linewidths (greater than approximately 10meV) in the low temperature emission spectrum are not suitable for the study of dots and wires since the linewidth of the emission spectrum increases dramatically after patterning. Samples which have fewer inhomogeneities will provide spectra which are easier to interpret. A full characterization of the sample both prior to and after fabrication is essential in interpreting data from emission spectra.

Concerning techniques to study optical processes in nanostructures, the spatially resolved FFTPL work indicates that it is essential to map each sample, particularly if there are inhomogeneities in the sample. In addition, techniques which can study emission from a few nanostructures (ideally a single nanostructure) such as cathodoluminescence and scanning optical probes, would be very useful. At present the spectrum obtained from small dots is a composite of the emission of each dot or wire in a large (500μm^2) array and any property results in the average response of a large group of nanostructures.

The FFT spectrometer which was used at UMIST is suitable for recording signals from arrays of structures which emit only weakly. If this could be harnessed to record absorption measurements from arrays of wires or dots then it would be an invaluable tool for the study of nanostructures.

Structured studies such as X-ray dynamical theoretical approaches and modelling which have been applied so far to wires should be extended to dots. For wires, such X-ray analysis would yield the compositions, interface mixing, strain and periodicity. At the time of writing

this thesis the author learnt of a pre-print of a paper using triple X-ray analysis for the study of GaInAs/InP wires.

The study of GaInAs/InP nanostructures remains to be completed. For it to yield the required information on device-relevant optical properties there is a need for the following:

(i) uniform samples to avoid the localization - confinement interplay

(ii) minimum damage RIE processes

(iii) single nanostructure optical spectroscopy techniques

(iv) advanced structural studies

(v) more efficient optical techniques in terms of light collection, such as FFT, and in terms of probing higher energy levels

(vi) extension of the work to doped structures.

Appendix A

Data for $In_{0.53}Ga_{0.47}As/InP$ Material

The following values of effective masses for electrons, light holes and heavy holes were used throughout this thesis:

InGaAs:

$$\frac{m_e^*}{m_o} = 0.041$$

$$\frac{m_{lh}^*}{m_o} = 0.05$$

$$\frac{m_{hh}^*}{m_o} = 0.05$$

The value of permittivity of $In_{0.53}Ga_{0.47}As$ used in this thesis was:

$$\varepsilon_r = 13.7$$

The following values of energy gap were used throughout this thesis:

Material	Temperature (K)	Energy Gap (meV)
InGaAs	298	750
	4.2	813
InP	298	1351
	4.2	1423

The following values of band offsets were used for InGaAs/InP at 4.2K:

$$\Delta E_c = 230meV$$

$$\Delta E_v = 380meV$$

Appendix B

Gaussian Lineshape Fitting

The deconvolution of a PL spectrum was achieved assuming overlapping contributions in energy from two or more emission processes. In general, in a quantum well these can be lineshape fitted using a Gaussian function like:

$$I = A \exp\left\{-\left[\frac{(x-b)}{c}\right]^2\right\}$$

where I is the intensity of the peak, c is a factor which takes account of the breadth of the peak, and b is the position of the peak. The full width at half maximum (Γ) is related to the factor c by the following equation:

$$\Gamma = 2\sqrt{\ln 2}\, c$$

The function of Γ is to account for all of the broadening (scattering) mechanisms. InGaAs is an alloy which is lattice matched when the proportion of indium is approximately 50%, and so the material is in mid-composition where the alloy disorder is greatest. The values of Γ chosen reflect this fact with Γ in the range from 10 to 25meV.

GLASGOW
UNIVERSITY
LIBRARY